Effects of Molecular Adsorption on Properties of Nanocarbons

July 2013

Mingxia LU

Graduate School of Science

CHIBA UNIVERSITY

Contents

Chapter 1

General Introduction

Carbon materials are found in various forms such as graphite, diamond, carbon fibers, fullerenes, graphene, and carbon nanotubes. Apart from the well-known graphite, carbon can build closed and open caged with honeycomb atomic arrangement. First such structure to be discovered was the C_{60} molecule by Kroto et al [1]. Although various carbon cages were studied, it was only in 1991, when Iijima observed for the first time tubular carbon structures [2]. The carbon nanotubes (CNTs) are consisted of up to several tens of graphitic shells (so called multi-walled carbon nanotube (MWCNTs)) with adjacent shell separation of ~0.34 nm, diameters of ~1 nm and large length/diameter ratio. Two years later, synthesis of single-walled nanotubes was independently reported by Iijima and Toshinari Ichihashi of NEC, and Donald Bethune and colleagues of the IBM Almaden Research Center in California [3, 4]. Then in 1999, Iijima et al. developed a new type of single wall nanocarbon named single wall carbon nanohorn (SWCNH), which has a nanotubular and forms a unique assembly structure with a "Dahlia-flower-like" feature [5]. Furthermore, in 2004 physicists at the University of Manchester and the Institute for Microelectronics Technology, Chernogolovka, Russia, first isolated individual graphene planes by using adhesive tape. They also measured electronic properties of the obtained flakes and showed their unique properties [6]. Nowadays, there are a number of methods of making CNTs such as arc-discharge, laser-ablation, and catalytic growth [7-9]. The synthesized CNTs are also characterization by the measurement such as Raman spectroscopy, electronic and optical spectroscopies for the nano-science and nano-devices.

Carbon nanotubes, especially SWNTs, have been termed "materials of the 21st century" due to their functional mechanical, electrical and optoelectronic properties, since they already outperform classical materials such as organic polymers and

semiconductors [10]. Fuelled by potentially important applications for these materials, carbon nanotube research has sprung to an astonishing scale in only a few years, opening new challenges and opportunities for chemistry of these structures. Nanotube research is truly multi- and interdisciplinary: engineers are developing next-generation composites [11], electronic devices [10], and adsorbents [12] based on nanotubes; chemists are exploring nanotubes as containers for molecules [13] and ions [14] and as nanoscale reactors; biologists see nanotubes as potential shuttles for organ-selective drug delivery and other therapeutic and diagnostic purposes [15-17]. The physico-chemical nature of carbon nanotubes, which essentially can be viewed as fully conjugated polyaromatic macromolecules with a hollow, inert interior and reactive exterior and ends, drives applications in all these fields.

The application and research of nano-devices using CNTs have received great attention in the last decade. The CNTs have been attractive for various application fields due to their high mechanical strength, high chemical stability, high thermal and electrical conductivity, and large aspect ratio with naturally formed small diameters [18-20]. Particularly, their fascinating electrical and mechanical properties offer a new arena to the development of advanced engineering devices materials.

In order to enhance the electrical property of the SWCNTs, the study for the electronic structure of SWCNTs looks very important. Recently, the studies on the electrical properties of SWCNTs have been focused on the charge transfer interaction of modified SWCNTs with electron donor or acceptor molecules that allow the manipulation of electrical conductivity of SWCNTs [21-23]. Conventional modification of SWCNTs has been realized by intercalation with iodine or halogenides of Na, K, Rb, Cs, Ca, Cu, and Ag through gas phase doping or liquid phase adsorption methods [24-29]. These SWCNTs modified with metal halogenides always show a p-type behavior, which means that electrons always are withdrawn from the valence band of SWCNTs to the adsorbates and the main charge carrier in the SWCNTs are holes. In this study, hexaiodobenzene (HIB, C_6I_6) is chosen as a charge transfer molecule to modified the SWCNTs, because which exhibit a two-electron oxidation that generates a di-cation $(C_6I_6)^{2+}$ from HIB (C6I6) [30]. This

indicating HIB possibly act as electron donor. The detail of the effects of HIB for SWCNT is shown in Chapter 4.

More recently, researchers attempt to employ SWCNTs as the electrode materials of electrochemical sensors and dye-sensitized solar cells (DSCs) [31-33]. The subtle electronic properties confirmed that SWCNTs have the ability to promote charge transfer reactions when used as an electrode in electrochemical reactions. The aim of this work is to explore the effect of tri-iodide ions (I_3^-) on the Single-Walled Carbon Nanotube (SWCNTs) coated Polyethylene Terephthalate (PET) thin-films using electrochemical method. The detail is shown in chapter 5.

And also, this thesis is constructed as follows:

In ***Chapter 2***, characterization method to catalysts and carbon nanomaterials are introduced. Nitrogen adsorption at 77 K, thermogravimetry, X-ray photoelectron spectroscopy, scanning electron microscope, transmission electron microscope, UV-Vis-NIR spectroscopy, Raman spectroscopy, pulsed-field gradient nuclear magnetic resonance spectroscopy and electrochemical measurements including cyclic voltammetry and alternating current impedance are discussed in basic theory and application. ***Chapter 3*** introduces the nanocarbon materials are excellent device materials used in various fields, nanocarbons like carbon nanotube, and activated carbon fibers are discussed in their history background, structure, synthesis method, properties and application. ***Chapter 4*** presents the physical modification of SWCNTs with HIB molecules through liquid-phase adsorption. The electronic structure changes of SWCNTs were investigated by spectroscopic methods. UV-Vis-NIR absorption spectra analysis shows the interaction of HIB could induce a change of the electron density of state in SWCNTs. Both Raman and C1s XPS analyses revealed a slight reduction of carbon in SWCNTs upon HIB adsorption. From these results, we conclude that HIB can act as an electron donor for SWCNTs. ***Chapter 5*** mainly discussed the surface changes of the SWCNT-PET film electrodes after electrochemical redox reaction. And the redox peaks difference and the charge transfer impedance changes by increasing SWCNTs loading on the film electrodes.

Chapter 6 describes the diffusion behavior of ionic liquids confined in ACF, and the changes of the chemical shift in ACF compare with the bulk ionic liquids.

References

[1] H. W. Kroto, J. R. Heath, S. C. O'Brien, R. F. Curl, R. E. Smalley, *Nature* **1985** *318*, 162.

[2] S. Iijima, *Nature* **1991**, *354*, 56.

[3] S. Iijima, T. Ichihashi, *Nature* **1999**, *363*, 603.

[4] D. S. Bethunem, C. H. Kiang, M. S. de Vries, G. Gorman, R. Savoy, R. Beyer, *Nature* **1993**, *363*, 605.

[5] S. Iijima, M. Yudasaka, R. Yamada, S. Bandow, K. Suenaga, F. Kokai, *Chem. Phys. Lett.* **1999**, *309*,165.

[6] K. S. Novoselov, A. K. Geim, S. V. Morozov, D. Jiang, Y. Zhang, S. V. Dubonos, I. V. Grigorieva, A. A. Firsov, *Science* **2004**, *306*, 666.

[7] S. Iijiama, T. Ichihashi, Y. Ando, *Nature* **1992**, *356*, 776.

[8] A. Thess, R. Lee, P. Nikolaev, H. Dai, P. Petit, J. Tobert, C. Xu, Y. H. Lee, S. G. Kim, A. G. Rinzler, D. T. Colbert, G. E. Scuseria, D. Tomanek, J. E. Fischr, T. E. Smalley, *Science* **1996***, 273*, 483.

[9] W. Z. Li, S. S. Xie, L. X. Qian, B. H. Chang, B. S. Zou, W. Y. Zhou, R. A. Zhao, G. Wang, *Science* **1997***, 274*, 1701.

[10] P. Avouris, *Acc. Chem. Res.* **2002***, 35*, 1026.

[11] E. T. Thostenson, Z. F. Ren, T. W. Chou, *Compos. Sci. Technol.* **2001***, 61*, 1899.

[12] M. S. Dresselhaus, K. A. Williams, P. C. Eklund, *MRS Bull.* **1999***, 24,* 45.

[13] M. Monthioux, *Carbon* **2002***, 40*, 1809.

[14] J. Sloan, D. E. Luzzi, A. I. Kirkland, J. L. Hutchison, M. L. H. Green, *MRS Bull.* **2004***, 29*, 265.

[15] N. W. S. Kam, M. O'Connell, J. A. Wisdom, H. J. Dai, *Proc. Natl. Acad. Sci. U. S. A.* **2005***, 102*, 11600.

[16] S. J. Son, J. Reichel, B. He, M. Schuchman, S. B. Lee, *J. Am. Chem. Soc.* **2005***, 127*, 7316.

[17] C. R. Martin, P. Kohli, *Nat. Rev. Drug Discovery* **2003***, 2*, 29.

[18] W. A. D. Heer, A. Chatelain, D. Ugarte, *Science* **1995***, 270*, 1179.

[19] M. S. Dresselhaus, G. Dresselhaus, P. Eklund, *In Science of Fullerenes and Carbon Nanotubes; Academic Press: New York*, **1996**.

[20] A. N. Popov, *Material Science and Engineering R **2004**, 43*. 61.

[21] M. Shiraishi, S. Swaraj, T. Takenobu, T. Y. Iwasa, M. Ata, W. E. S. Unger. *Phys. Rev. B* **2005**, *71*, 12549.

[22] R. Voggu, C. S. Rout, A. D. Franklin, T. S. Fisher, C. N. R. Rao, *J. Phys. Chem. C* **2008**, *112*, 13053.

[23] C. N. R. Rao, R. Voggu. *Mater. Today* **2010**, *13*, 34.

[24] C. Hayakawa, K. Urita, T. Ohba, H. Kanoh, K. Kaneko, *Langmuir* **2009**, *25*, 1795.

[25] A. M. Rao, P. C. Eklund, S. Bandow, A. Thess, R. E. Smalley, *Nature* **1997**, *388*,

257.

[26] N. Minami, S. Kazaoui, R. Jacquemin, H. Yamawaki, K. Aoki, H. Kataura, Y. Achiba, *Synth. Metal*. **2001**, *116*, 405.

[27] F. Khoerunnisa, T. Fujimori, T. Itoh, H. Kanoh, T. Ohba, M. Yudasaka, S. Iijima, K. Kaneko, *Chem. Phys. Lett.* **2001**, *501*, 485.

[28] A. A. Eliseev, L. V. Yashina, M. M. Brzhezinskaya, M. V. Chernysheva, M. V. Kharlamova, N. I. Verbitsky, A. V. Lukashin, N. A. Kiselev, A. S. Kumskov, R. M. Zakalyuhin, J. L. Hutchison, B. Freitag, A. S. Vinogradov, *Carbon* **2010**, *48*, 2708.

[29] S. Ghosh, S. R. K. C. Sharma Yamijala, S. K. Pati, C. N. R. Rao, *RSC Advances* **2012**, *2*, 1181.

[30] D. J. Sagl, J. C. Martin, *J. Am. Chem. Soc.* **1988**, *110,* 5827-5833.

[31] T. N. Murakami, M. Gratzel, *Inorganica Chimica Acta* **2008***, 361*, 572.

[32] S. Kim, J. Yim, X. Wang, D. C. Bradley, *Adv. Funct. Mater.* **2010***, 20*, 2310.

[33] C. Y. Su, A. Y. Lu, Y. L. Chen, C. Y. Wei, P. C. Wang, C. H. Tsai, *J. Mater. Chem.* **2010***, 20*, 7034.

Chapter 2

Basic Theories

2.1. Adsorption

Adsorption is a process of adhere the atoms, ions, or molecules from a dissolved solid, liquid, or gas to a surface. Adsorption is present in many natural physical, biological, and chemical systems, and is widely used in industrial applications such as gas separations, increase storage capacity of carbide-derived carbons for tunable nanoporous carbon, and water purification. According to the international union of pure and applied chemistry (IUPAC) term, adsorption can be classified as physical adsorption (physisorption) and chemical adsorption (chemisorption). The physical adsorption is caused by van der Waals force with very weak interaction energy. The chemical adsorption is a chemical reaction between the adsorbate and adsorbent with stronger interaction energy than physical adsorption.

2.1.1. Porosity

Pore size is important to the function of a porous material. In the past the terms micropore and macropore have been applied in different ways by physical chemists and some other scientists. Porous materials are classified by pore size according to the International Union of Pure and Applied Chemistry (IUPAC) [1, 2]. As indicated, the pore size is generally specified as the pore width, i.e. the available distance between the two opposite pore walls. Three groups of pore size classification are shown in table 2-1.

Micropore, the pore width is less than 2 nm, be filled in the region of low relative pressure, and corresponds to the strong adsorption field. The more precise classification would distinguish two types of micropore: ultramicropore (pore size up

to 0.7 nm) and supermicropore (from 0.7 nm to 2 nm). As a consequence of the overlapping of the opposite pores walls adsorption potential, the micropore filling corresponds to the enhancement of adsorption at low relative pressure region (where initial steep portion appears in adsorption isotherm).

Table 2-1 The classification of pores

Term		Pore size (nm)
Micropore	Ultramicropore	$w < 0.7$
	Supermicopore	$0.7 < w < 2$
Mesopore		$2 < w < 50$
Macropore		$w > 50$

Mesopore, which pore width from 2 nm to 50 nm, corresponds to the middle part of isotherms. In mesopore the adsorbate condenses in a liquid-like state by capillary condensation and a meniscus is formed, the phenomenon in mesopores is characterized by a hysteresis loop typically appearing in the relative pressure higher than 0.4 P / P_0, which adsorption and desorption branches separate each other.

Macropore is the pore width greater than 50 nm. Adsorption in macropores is similar to adsorption behavior on open surfaces; the limit of 50 nm is artificial and it corresponds to the practical limit of the method for the size determination based on the analysis of the hysteresis loop.

2.1.2. Adsorption Isotherm

As it has been introduced in the top of this chapter, adsorption is a surface phenomenon which occurs when a solid surface is exposed to a gas or liquid, it is defined as the enrichment of material or increase in the density of the fluid in the vicinity of an interface. Porosity of powders and other porous solids can be characterized by gas adsorption studies [3, 4]. For the evaluation of the porosity of

most solid porous materials, nitrogen adsorption at 77 K is the most useful method.

An adsorption process can be reflected by adsorption isotherm, which shows the relationship between the amount of gas adsorbed and the pressure or relative pressure at a constant temperature. The amount of the adsorbed materials (n) on the solid surface depends on the measuring pressure (P), temperature (T), and interaction potential between the gases and solid surface (E). Thus, the adsorption amount can be expressed as:

$$n = f(P, T, E) \tag{2-1}$$

In general, for a given gas adsorbed on a particular solid maintained at a constant temperature *T*, the equation can simply to:

$$n = f(P)_{T,E} \tag{2-2}$$

At a critical temperature of gas, the equation becomes:

$$n = f(P/P_0)_{T,E} \tag{2-3}$$

where P/P_0 is the relative pressure.

Figure 2-1 shows diagrammatic representation of adsorption isotherms classified by the IUPAC. The majority of physical adsorption isotherms can be grouped into six types [5]. The brief description of the six isotherms is as follows:

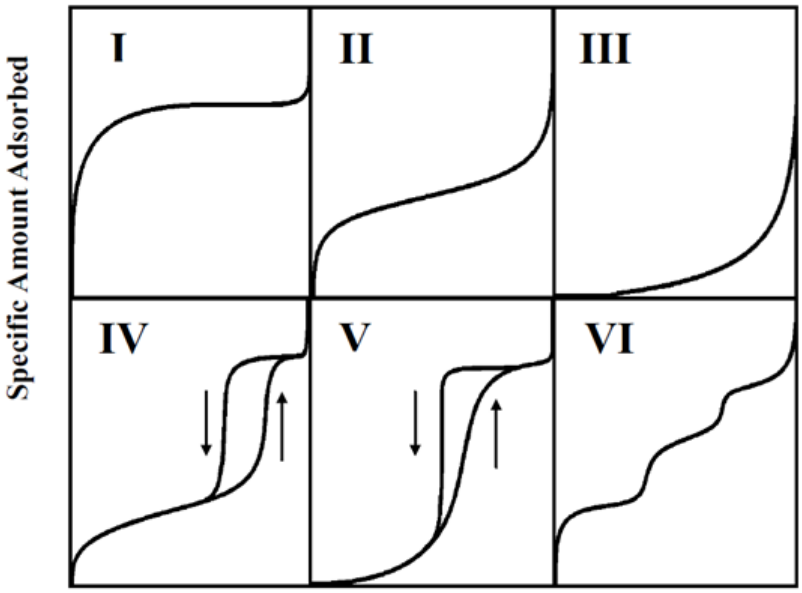

Figure 2-1 The IUPAC classification for adsorption isotherms [5]

Type Ⅰ isotherms

Type Ⅰ isotherm are also called Langmuir isotherm due to the adsorption on a microporous solid. The potential fields from neighboring walls overlap and interaction energy of a solid with a gas molecule is correspondingly enhanced [6]. The interaction may be strong enough to bring about a complete filling of the pores at a quite low relative pressure. The long plateau shape of isotherm indicates monolayer coverage. This type of behavior implies to be typical of chemical adsorption.

Type Ⅱ isotherms

Type Ⅱ isotherms well known as BET-type isotherms with the s-shape are typically obtained in case of monolayer-multilayer adsorption on a non-porous or macroporous adsorbent. Point B, the beginning of the almost linear middle section of the isotherm, is usually considered as the turning point of completion of monolayer formation and beginning of the multilayer adsorption.

Type Ⅲ isotherms

Type Ⅲ isotherms are given by non-porous or macroporous solids, are obtained

when the interaction between the adsorbates and adsorbents are smaller than those of adsorbates. This weak interaction causes the uptake at low relative pressures are small; but once the molecules has been adsorbed, the interaction between adsorbates will promote the adsorption of further molecules. Thus, the isotherm is convex to the P/P_0 axis over its entire range isotherms.

Type IV isotherms

Type Ⅳ isotherms are typical for mesoporous solids. This type of isotherms has a similar surface interaction with the Type Ⅱ isotherms since it follows the same path at the low pressure region. The most characteristic feature is the hysteresis loop, which is associated with capillary condensation taking place in mesopores, and the limiting uptake over a range of high P/P_0.

Type Ⅴ isotherms

Type Ⅴ isotherms are given by mesoporous or microporous solids and are very much similar to Type Ⅲ. Type Ⅴ isotherms also exhibits a hysteresis loop, which is associated with the mechanism of pore filling and emptying. Comparing with Type Ⅳ isotherms, Type Ⅴ isotherms a initially convex to the P/P 0 axis, which is indicative of weak adsorbent-adsorbate interactions.

Type Ⅵ isotherms

Type Ⅵ isotherms are called the stepwise isotherms. In which, the sharpness of the steps depends on the system and the temperature, represents stepwise multilayer adsorption on a uniform non-porous surface. The step-height now represents the monolayer capacity for each adsorbed layer and, in the simplest case, remains nearly constant for two or three adsorbed layers. This kind of isotherms is obtained from stepwise multilayer adsorption on a uniform, non-porous surface, particularly by spherically symmetrical, non-polar adsorptives [7]. Kr adsorption on the perfect graphite shows such kind of stepwise isotherm.

2.1.3. Theories of Adsorption

We can obtain many information from adsorption isotherms, so how to analysis the isotherms is essential important, and the analyze methods are also the key position of adsorption science. In this section, several analysis methods of adsorption isotherms have been provided, such as BET, αs-plot, D-R and t-plot, etc. These methods are quite different each other, especially micropore analysis, the different will be greater.

2.1.3.1. The Langmuir Equation

The Langmuir equation initially derived from kinetic studies was based on the assumption that: 1) fixed number of vacant or adsorption sites are available on the surface of solid, 2) all the vacant sites are of equal size and shape on the surface of adsorbent, 3) each site can hold maximum of one gaseous molecule and a constant amount of heat energy is released during this process, 4) dynamic equilibrium exists between adsorbed gaseous molecules and the free gaseous molecules, 5) adsorption is monolayer.

The adsorption process between gas phase molecules (A), vacant surface sites (S), and occupied surface sites (SA), can be represented by the equation,

$$S + A \rightleftharpoons SA \tag{2-4}$$

assuming that there are a fixed number of surface sites present on the surface.

An equilibrium constant, K, can be written:

$$K = \frac{[SA]}{[S][A]} \tag{2-5}$$

θ = Fraction of surface sites occupied (surface coverage) ($0 < \theta < 1$)

Note that: [SA] is proportional to the surface coverage of adsorbed molecules, or proportional to θ; [S] is proportional to the number of vacant sites, (1 -θ); [A] is proportional to the pressure of gas, P

Thus it is possible to define the equilibrium constant, b:

$$b = \frac{\theta}{(1-\theta)P} \tag{2-6}$$

Rearranging gives the expression for surface coverage:

$$\theta = \frac{\mathrm{bP}}{1+\mathrm{bP}} \tag{2-7}$$

That is the note as the Langmuir equation.

2.1.3.2. The Brunauer, Emmett, and Teller (BET) Adsorption Theory [2]

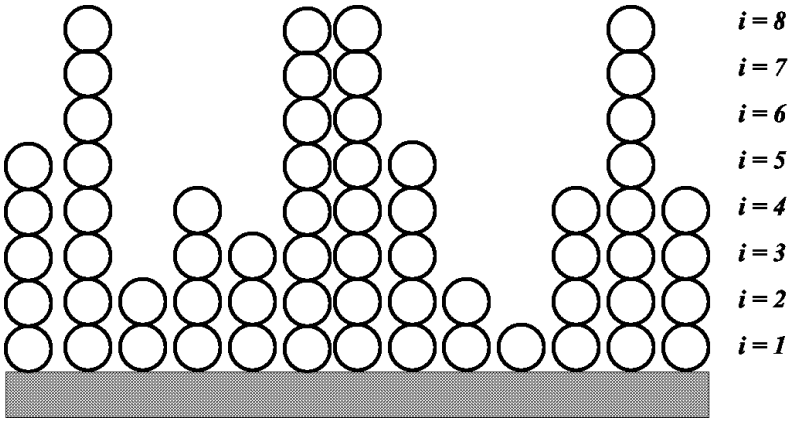

Figure 2-2. The model of BET multilayer adsorption

The abbreviation of Brunauer-Emmett-Teller adsorption analysis method, which named by the three scientists developed this method, and BET adsorption detection was based on the BET theory [54]. The BET theory is the most widely used procedure for the determination of the surface area of solid materials. It is an extended Langmuir model which based on that the multilayer adsorption is occurred on the solid surface. Figure 2-2 shows the BET multilayer model, where i and S_i are the number of layers adsorbates and sites formed i-numbers molecular layers.

For the first layer adsorption, when the adsorption system is equilibrium at a pressure (P), the velocity of adsorption and desorption is equivalent. The relationship is given by

$$a_1 P s_0 = b_1 s_1 exp(-E_1/RT) \tag{2-8}$$

where a_1 and b_1 are the constant, E_1 is a molecular adsorption energy of first layer. These values not depend on the number of adsorbed molecules on the surface of solid and then the BET model assumes that the adsorption sites on the surface are energetically equivalent. In a similar way, *i*-layers at equilibrium pressure (P) becomes

$$a_i P s_{i-1} = b_i s_i exp(-E_i/RT) \tag{2-9}$$

So, the number of all adsorbed molecules (v) is given by

$$v = \sum_{i=0}^{\infty} S_i \tag{2-10}$$

And then, the number of all sites, which is the monolayer capacity (v_m), becomes

$$v_m = \sum_{i=0}^{\infty} S_i \tag{2-11}$$

Here, it is assumed that the adsorption energy of molecules adsorbed above second layers is equivalent to liquid cohesive energy (E_L). It means

$$E_2 = E_3 = \cdots = E_i = E_L \tag{2-12}$$

The interaction between molecules adsorbed above second layers and the surface of solid is sufficiently small. Because the adsorptive molecules are adsorbed by only the interaction between adsorbed molecules, a_1 and b_1 ratios are constant which is denoted by

$$b_2/a_2 = b_3/a_3 = \cdots = b_i/a_i = g \tag{2-13}$$

Additionally, *x* and *c* are denoted by

$$(P/g)exp(E_L/RT) = x \tag{2-14}$$

$$(a_1 g/b_1)exp[(E_1 - E_L)/RT] = c \tag{2-15}$$

For all of these equations,

$$\frac{v}{v_m} = \frac{cx}{(1-x)(1-x+cx)} \tag{2-16}$$

Where *x* indicates a relative pressure defined as

$$x = P/P_0 \tag{2-17}$$

By (2-16), (2-17) can be rewritten as

$$v = \frac{v_m cP}{(P_0 - P)\left(1 + (c-1)(P/P_0)\right)} \tag{2-18}$$

This equation is called Langmuir equation.

(a) BET Plot

The BET equation can also be written as

$$\frac{P}{v(P_0 - P)} = \frac{1}{v_m c} + \frac{c-1}{v_m c}(P/P_0) \tag{2-19}$$

When P/P_0 and $v(P_0 - P)$ are plotted along the abscissa and the ordinate (shown as figure 2-3), the monolayer capacity (v_m) and the constant (c), which is related to heat of adsorption, are found. Generally, the BET equation is formed at the rage of P/P_0 from 0.05 to 0.35, where the coverage ($\theta = v/v_m$) is from 0.5 to 1.5. In the case of micropore systems such as activated carbon fiber, the monolayer is formed at lower relative pressure than that of flattened surface. Therefore, the range of P/P_0 is used from 0.01 to 0.05.

(b) Determination of the Specific Surface Area

When we analysed an adsorption isotherm by Brunauer, Emmett and Teller (BET) method which is representative method of multilayer adsorption, the specific surface area (A_s) is given by

$$A_s = (v_m N a_m / M) \times 10^{-18} \quad [\mathrm{m^2/g}] \tag{2-20}$$

where v_m, N, a_m and M are monolayer capacity (g/g), Avogadro constant (6.022×10^{-23}), molecular cross-section area and molecular weight of adsorbed molecule.

2.1.3.3 α_s-Plot Method

α_s-plot method is a very effective way to determining nanoporosity which is

similar to the t-plot method. This method was recommended by K. S. W. Sing in 1989 [8]. This method can be achieved by comparing a given isotherm to a standard curve, thus the invoking the concept of a statistical thickness *t* is not required.

Sing defined the α_s value as the relative adsorption amount of a standard reference sample,

$$\alpha_s = \frac{A}{A_{0.4}} \tag{2-21}$$

where A is the adsorption amount of the sample, while $A_{0.4}$ is the adsorption amount at relative pressure P/P_0=0.4.

The standard α_s-curve is obtained by plotted the normalized adsorption amount α_s against P/P_0. The α_s-curve can be then used to construct a α_s-plot from the isotherm of a sample. To estimate the specific surface area (A_s) of a sample, we calculate from using the slope (S) of the α_s-plot as follows

$$A_s = [S_\alpha(sample)/S_\alpha(standard)] \times A(standard) \tag{2-22}$$

where the A (standard) is the specific surface area estimated by other methods such as BET, S_α is the slop of the straight line from origin to the linearity region near α_s =0.5, as shown in Fig 2-3. Based on the slop of this line, total surface area can be obtained. When $\alpha_s \geq 1.0$, adsorption in micropore finished, the higher region of α_s can be considered as external surface adsorption. External surface area, micropore surface area and micrpore volume can be calculated from the slop and intercept of the straight line which α_s value greater than 1. Furthermore, due to the slit-pore hypothesis, micropore width can be calculated according to next formula:

$$w = \left(\frac{2W_0}{A_{total} - A_{ext}}\right) \times 1000 \tag{2-23}$$

where W_0 is the micropore volume, A_{total} is the total surface area, and A_{ext} is the external surface area.

For solid material without pores, α_s plot is a straight line pass through the origin, the slope of s. For the samples with micropore or mesopore, α_s plot deviate from the straight line. From Figure 2-3, shows a typical α_s plot with two auxiliary line and two swings: filling sing and

condensation swing. Filling swing is in the lower α_s region (< 0.4) originate from the enhance adsorption by the micropore. Because adsorption of molecule in a miltilayer limited by the pore width, can be enhanced by a kind of capillary condensation before saturated filling in micropore solid having relatively large micropore, condensation swing ascribe to such a capillary condensation effect just below the gradually increase [9].

The advantage of α_s method is it can be utilized no matter we know the statistic thickness or not, and it is available for other adsorbate besides N_2. In our lab, the reference solid used is non-porous carbon black for construction of the high resolution α_s plot.

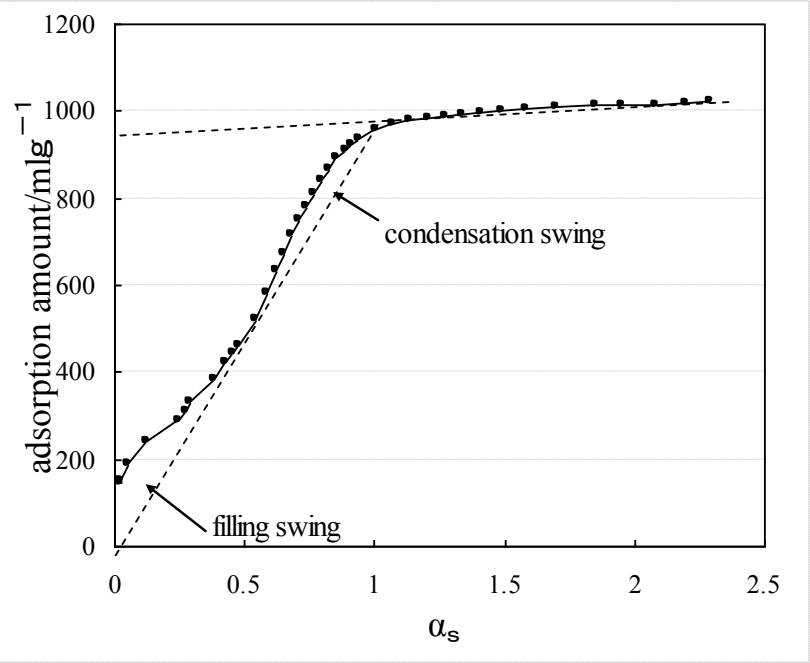

Figure 2-3. α_s plot

2.1.3.4 Dubinin and Radushkevich (DR) Theory [10]

The adsorption in micropore is caused at low pressure. Dubinin and Radushkevich propounded an equation to clarify the micropore volume from low pressure. The equation is based on Polanyi's adsorption potential theory.

The adsorption potential (ε) is rewritten by a differential free energy (ΔG),

$$\varepsilon = -\Delta G = RTln(P_0/P) \tag{2-24}$$

If we assumed that the adsorption of molecules in micropore is pore filling but not stake on the pore walls, the filling ratio (θ) is given by

$$\theta = W/W_0 \tag{2-25}$$

where W is the filled volume of the micropore at relative pressure (P/P_0), while W_0 is the total volume of the micropore system. Since the filling ratio (θ) is a function of P/P_0 as well as ε, θ can be rewritten as

$$\theta = f(\varepsilon/\beta) \tag{2-26}$$

where β is an affinity coefficient and defined as the ratio of the adsorption potentials of adsorbate (ε) and a standard adsorbate (ε_0),

$$\beta = \varepsilon/\varepsilon_0 \tag{2-27}$$

Under the assumption that the pore size distribution is Gaussian, Dubinin-Radushkevich, then formulated the ratio of micropore filling as

$$\theta = exp[-k(\varepsilon/\beta)^2] \tag{2-28}$$

Where k is a constant determined by pore structure. By combining the equations (2-26)-(2-28) then

$$W = W_0 exp[(-k/\beta^2) \times (RTln\, P_0/P)^2] \tag{2-29}$$

or

$$W/W_0 = exp\{-k(RT/\beta)^2[2.303log(P_0/P)]^2\} \tag{2-30}$$

where $2.303k(RT/\beta)^2 = D$, then

$$logW = logW_0 - Dlog^2(P_0/P) \tag{2-31}$$

The equation (2-31) is well-known as Dubinin-Radushkevich (DR) equation. The linear curve can be obtained by plotting the $log\ W$ against $[log(P/P_0)]^2$ so called

DR-plot. The micropore volume (W_0) then is determined from the intercept ($log\ W_0$).

2.2. Characterization of Nanocarbon Materials

2.2.1. Absorption Spectroscopy

Absorption spectroscopy refers to spectroscopic techniques that measure the absorption of radiation, as a function of frequency or wavelength, due to its interaction with a sample. The sample absorbs energy, i.e., photons, from the radiating field. The intensity of the absorption varies as a function of frequency, and this variation is the absorption spectrum. Absorption spectroscopy is performed across the electromagnetic spectrum.

Absorption spectroscopy is employed as an analytical chemistry tool to determine the presence of a particular substance in a sample and, in many cases, to quantify the amount of the substance present. Infrared and ultraviolet-visible spectroscopy is particularly common in analytical applications. Absorption spectroscopy is also employed in studies of molecular and atomic physics, astronomical spectroscopy and remote sensing.

Many molecules absorb ultraviolet (UV) or visible light. The absorbance of a solution increases as attenuation of the beam increases. Absorbance is directly proportional to the path length, *b*, and the concentration, *c*, of the absorbing species. *Beer's Law* states that

$$log_{10}\, I_0/I = A = \varepsilon bc \tag{2-32}$$

where I_0 is the intensity of incident radiation, I is the intensity of radiation transmitted through the sample, and ε is a constant of proportionality, called absorptivity.

The absorption of UV or visible radiation corresponds to the excitation of outer electrons. There are three types of electronic transition which can be considered; 1) transitions involving p, s, and *n* electrons; 2) transitions involving charge-transfer electrons; 3) transitions involving *d* and *f* electrons (not covered in this Unit). When an atom or molecule absorbs energy, electrons are promoted from their ground state to

an excited state. In a molecule, the atoms can rotate and vibrate with respect to each other. These vibrations and rotations also have discrete energy levels, which can be considered as being packed on top of each electronic level.

Possible electronic transitions of p, s, and n electrons are shown in figure 2-4. The σ → σ* transition: an electron in a bonding σ orbital is excited to the corresponding anti-bonding orbital. The energy required is large. For example, methane (which has only C-H bonds, and can only undergo σ → σ* transition) shows an absorbance maximum at 125 nm. Absorption maxima due to σ → σ* transition cannot be seen in typical UV-Vis. spectra (200-800 nm). The *n* → σ* transition: saturated compounds containing atoms with lone pairs (non-bonding electrons) are capable of *n* → σ* transition. These transitions usually need less energy than σ → σ* transition. They can be initiated by light whose wavelength is in the range 150 - 250 nm. The number of organic functional groups with *n* → σ* peaks in the UV region is small. The *n* → π* transition and π→ π* transition: Most absorption spectroscopy of organic compounds is based on transitions of *n* or p electrons to the π* excited state. This is because the absorption peaks for these transitions fall in an experimentally convenient region of the spectrum (200-800 nm). These transitions need an unsaturated group in the molecule to provide the p electrons.

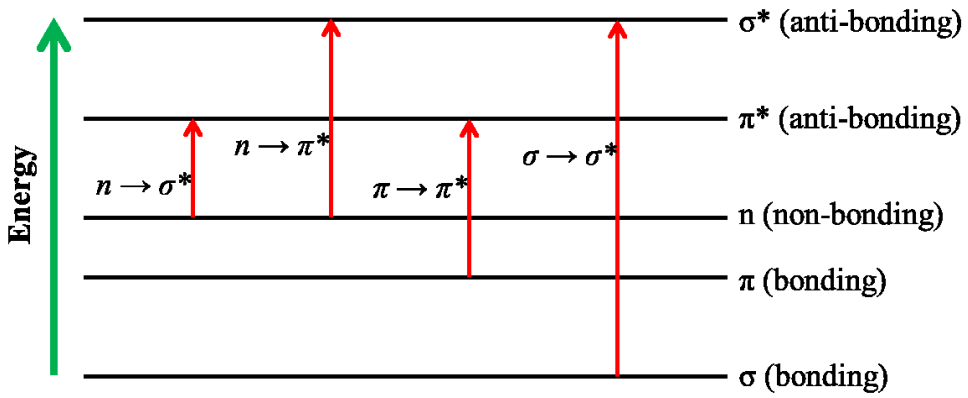

Figure 2-4.Tthe transition of electronic energy level

The optical properties are dominated by the electron transition between the pairs of van Hove singularities that are symmetrically located in the Fermi lever. Such intergap transitions denoted as S_{11}, S_{22}, for semiconducting nanotubes or M_{11} for metallic nanotubes are obviously important for absorption spectroscopy investigation. The electronic and optical properties of SWCNTs can be probes by the optical absorption spectroscopy. In particular, the visible-near infrared absorption spectra of SWCNTs show three regions; the first $C \rightarrow V$ transition for metallic SWCNTs, M_{11} (400-650 nm), and the first and second $C \rightarrow V$ transitions for semiconducting SWCNTs, S_{11} (900-1600 nm) and S_{22} (550-900 nm), respectively [11].

2.2.2. Raman Spectroscopy

Raman spectroscopy is a spectroscopic technique used to study vibrational, rotational, and other low-frequency modes in a system [12]. The Raman Effect was named after one of its discoverers, the Indian scientist Sir C. V. Raman. It is based on inelastic scattering, or Raman scattering, of monochromatic light, usually from a laser in the visible, near infrared, or near ultraviolet range. The laser light interacts with molecular vibrations, phonons or other excitations in the system, resulting in the energy of the laser photons being shifted up or down. The shift in energy gives information about the phonon modes in the system.

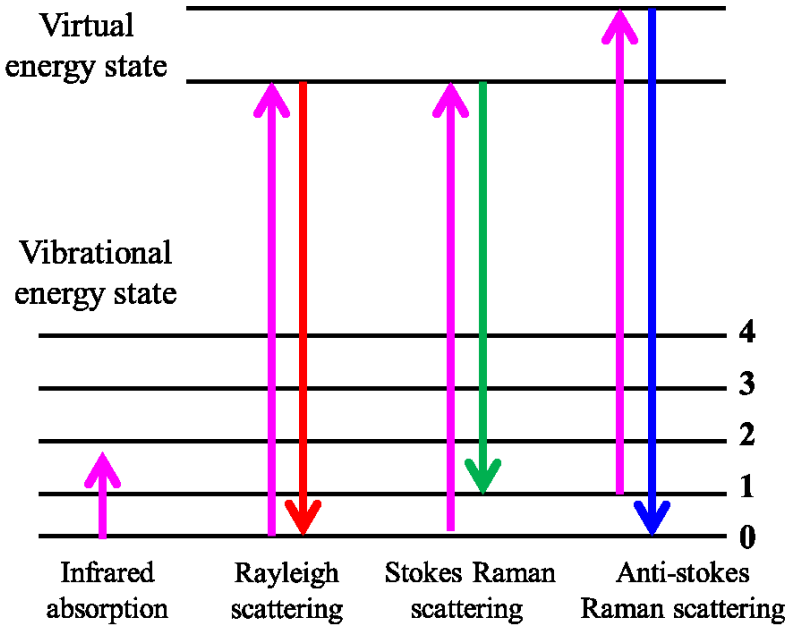

Figure 2-5. Energy level diagram for Raman scattering

The energy shift caused by energy transfer (E = *hv*) between the light and materials gives information about the phonon modes in the system, thus suggests the structure of the samples. Technically, the sauce has to provide the intense monochromatic radiation (usually laser). When light (frequency ν_0) is exposed on materials, light scattering is occurred by the collision of light and materials. The light scattering consists of the light with ν_0 (Rayleigh scattering) and a few shifted-light with $\nu_0 \pm \nu_i$ (Raman scattering) as shown in Figure 2–5. The Rayleigh scattering is elastic and there is no exchange in energy. However, Raman scattering leads to emission of another photon with a different frequency to the incident photon [13].

Raman spectroscopy is used to investigate the structure of sp^2-bonding carbon (e.g. graphite, carbon black), sp^3-bonding carbon (e.g. diamond), graphite intercalation compound, fullerene, carbon nanotube and sp-bonding carbon. Raman spectra of the materials based on graphitic structure lead two strong peaks. The Raman band at 1580 cm^{-1} (G-band) and 1380 cm^{-1} (D-band) are derived from graphite and defected structure, respectively. The intensity ratio of D-band to G-band called “R-value” indicates the graphitization grade of carbon materials. Another character was

observed at the low frequency region caused by the breathing vibration of the single-walled carbon nanotubulites, as well-known the radial breathing mode (RBM). The nanotube diameter can be calculated by the following equation,

$$\omega_{RBM} = \frac{A}{d} + B \tag{2-33}$$

where parameters A (248 nm cm^{-1}) and B (0 cm^{-1}) are determined experimentally [14]. In this study, the Raman spectroscopy is used to clarify the electronic structural changes of single-walled carbon nanotubes.

2.2.3. X-ray Photoelectron Spectroscopy

X-Ray Photoelectron Spectroscopy (XPS), also known as Electron Spectroscopy for Chemical Analysis (ESCA), is an analysis technique used to obtain chemical information about the surfaces of solid materials. Insulators and conductors can easily be analyzed in surface areas from a few microns to a few millimeters across.

XPS is based on the principle that X-rays hitting atoms generate photoelectrons. By measuring the number of these electrons as a function of kinetic (or binding) energy, an XPS spectrum is obtained. XPS is a typical example of a surface-sensitive technique, which can be used to measure the elemental composition, empirical formula, chemical state and electronic state of the elements that exist within a material.

Irradiating a material with a beam of X-rays gives rise to the emission of electrons. The energy of the emitted photoelectrons can be analyzed by the electron spectrometer and the data presented as a graph of intensity versus electron energy - the X-ray induced photoelectron spectrum can be obtained. The XPS process is schematically represented in Figure 2-6 for the emission of an electron from the 1s shell of an atom.

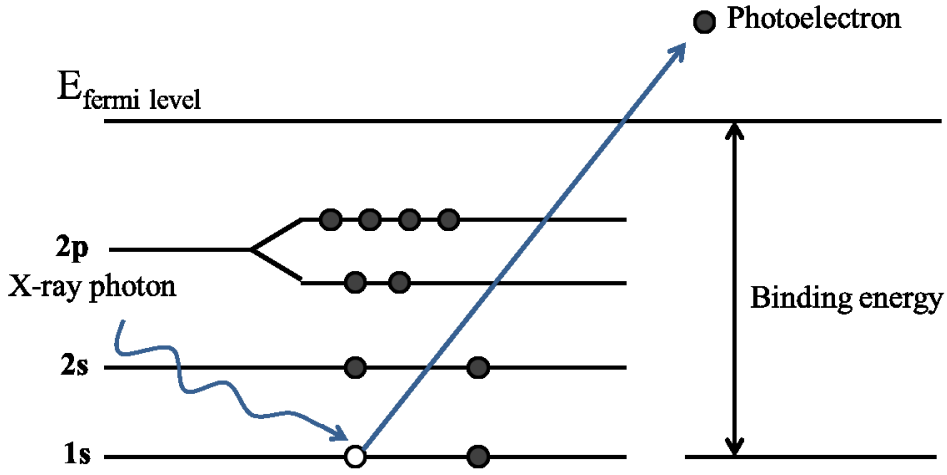

Figure 2-6. Schematic representation of the XPS process

The kinetic energy (EK) of the electron is the experimental quantity measured by the spectrometer, which depends on the energy *hv* of the primary X-ray source. The characteristic parameter for the electron is its binding energy. The electron binding energy of each of the emitted electrons can be determined by using an equation:

$$E_{binding} = hv - E_{kinetic} - W \tag{2-34}$$

where $E_{binding}$ is the binding energy of the electron, *hv* is the photon energy, and W is the spectrometer work function. As all three quantities on the right-hand side of the equation are known or measurable, it is a simple matter to calculate the binding energy of the electron. In addition, binding energy of the identical element with the identical orbital slightly changes with the condition around the observed atom. According to a measurement of this amount of change called chemical shift, the state analysis of the element is possible. In this study, we focused on the C1s peak and investigate the bond transformation of sp^2, sp^3 as well as the oxygen related functional groups of single-walled carbon nanotubes. Due to the adsorption treatment of hexaiodobenzene (HIB) on SWCNTs, the O1s and I3d peaks will be evaluated.

2.2.4. Scanning Electron Microscopy

The scanning electron microscope (SEM) is scientific instrument uses a beam of energetic electrons to generate a variety of signals at the surface of solid specimens. The signals that derive from electron-sample interactions reveal information about the sample including external morphology (texture), chemical composition, and crystalline structure and orientation of materials making up the sample. In most applications, data are collected over a selected area of the surface of the sample, and a 2-dimensional image is generated that displays spatial variations in these properties. In detail, a beam of electrons is produced at the top of the microscope by an electron gun. The electron beam follows a vertical path through the microscope, which is held within a vacuum. The beam travels through electromagnetic fields and lenses, which focus the beam down toward the sample. Once the beam hits the sample, electrons and X-rays are ejected from the sample. Detectors collect these X-rays, backscattered electrons, and secondary electrons and convert them into a signal that is sent to a screen similar to a television screen. This produces the final image.

Due to their low energy (< 50 eV) and very near to the surface (< 10 nm), these electrons can be collected and detected. Any changes in topography in the sample that are larger than this sampling depth will change the yield of secondary electrons due to collection efficiencies. Electronic amplifiers are used to amplify the signals, which are displayed as variations in brightness on a computer monitor, and the resulting image is therefore a distribution map of the intensity of the signal being emitted from the scanned area of the specimen. The magnification of a SEM can reach to about 500,000 times. The high spatial resolution of an SEM makes it a powerful tool to characterize a wide range of specimens at the nanometer to micrometer length scales.

2.2.5. Transmission Electron Microscopy

Different from scanning electron microscope (SEM), which doesn't use a concentrated electron beam to penetrate the object, Transmission Electron Microscopy (TEM) uses a high-powered beam to essentially shoot electrons through the object. The electron beam first passes through a condenser lens in order to

concentrate the beam on the object. Then the beam goes through the object. Some of the electrons pass all the way through; others hit molecules in the object and scatter. The modified beam then passes through an objective lens, a projector lens and onto a fluorescent screen where the final image is observed. Because the electron beam passes entirely through the object, the pattern of scatter gives the observed a comprehensive view of the interior of the object. TEM has the advantage over SEM that cellular structures of the specimen can be viewed at very high magnifications.

TEM can examine the fine detail of a sample, even as small as a single column of atoms. It forms a major analysis method in a range of scientific fields, in both physical and biological science.

2.2.6. Pulsed-Field Gradient-Nuclear Magnetic Resonance (PFG-NMR) Spectroscopy

Nuclear Magnetic Resonance (NMR) is a versatile technique in many disciplines of scientific research and industries (e.g., Magnetic Resonance Imaging (MRI) for clinical use to visualize internal structure of the body [15-18] and NMR spectrum for chemical identification and analysis [19-21]. Such applications allow us to obtain a variety of valuable information from the analyzed samples and help us to get insight into the microcosmic structure of interest. Among these, one can study the dynamic of molecules with the pulsed-field gradient (PFG) spin echo NMR technique.

The spin echo phenomenon in NMR was first found by Hahn in 1950 [22]. In his experiment, two $\pi/2$ radio frequency (rf) pulses were applied with an interval of τ. At the time of 2τ from the start of first $\pi/2$ rf pulse, echo signals were detected. Free induction decay (FID) was observed in the echo signals and the amplitudes of each signal were recorded. By plotting the logarithm of the maximum amplitude versus the value of 2τ, transverse relaxation time (T_2) was measured. In 1954, Carr and Purcell found that the T_2 values measured by Hahn's method would be severely affected by molecular diffusion [23]. They developed a new pulse sequence which replaced the second $\pi/2$ rf pulse with a π rf pulse, by which the sign of the phase angle of spins were reversed. By inserting numbers of (n) π rf pulses in certain time period, the

effect of molecular diffusion to the mean square phase dispersion $\langle\phi^2\rangle$ (which reflects the coherence of spin magnetizations in transverse plane and corresponding echo signal amplitude) was reduced by a factor determined by $1/n^2$. However, although their method provided relatively reliable way to measure T_2 value, the measurement of self-diffusion coefficient *D* was still not accurate. Several errors occurred in their calculation for *D* value. Also the magnetic field gradient was applied constantly in their experiments, which would bring lots of experimental limitations [24]. (E.g. decrease the duration of FID, require a large rf field amplitude, and difficult to define the precise diffusion time Δ.)

A remarkable improvement to the spin echo method was made by Stejskal and Tanner in 1965 [25]. Since the presence of magnetic field gradient during the rf pulses would require a large rf field amplitude; also at the time of echo, magnetic field gradient would decrease the duration of FID. To circumvent such experimental limitations, magnetic field gradient during both the rf pulses and the time of echo need reduced. Thus they applied a time-dependent magnetic field gradient instead of steady one on the spin echo experiment. Specifically, pulsed field gradient with the duration of Δ was applied during each of the τ period before and after π rf pulse. The period between the leading edges of gradient pulses was defined as diffusion time Δ, in which the diffusion of molecules was measured.

The role of gradient pulses in the diffusion experiment is to label the position of spins. In the isotropic diffusion, for simplicity, diffusion of molecules is measured only in one direction. Consider in a three-dimensional right angle coordinate system, in which static magnetic field B_0 is oriented in the z-axis. During the gradient pulse, spatial-dependent magnetic field with gradient g along z-direction is superimposed, which would impose different angular frequency to spins along the gradient. Thus the cumulative phase shifts of spins in xy-plane vary, which reflect the transient positions of spins in the gradient field.

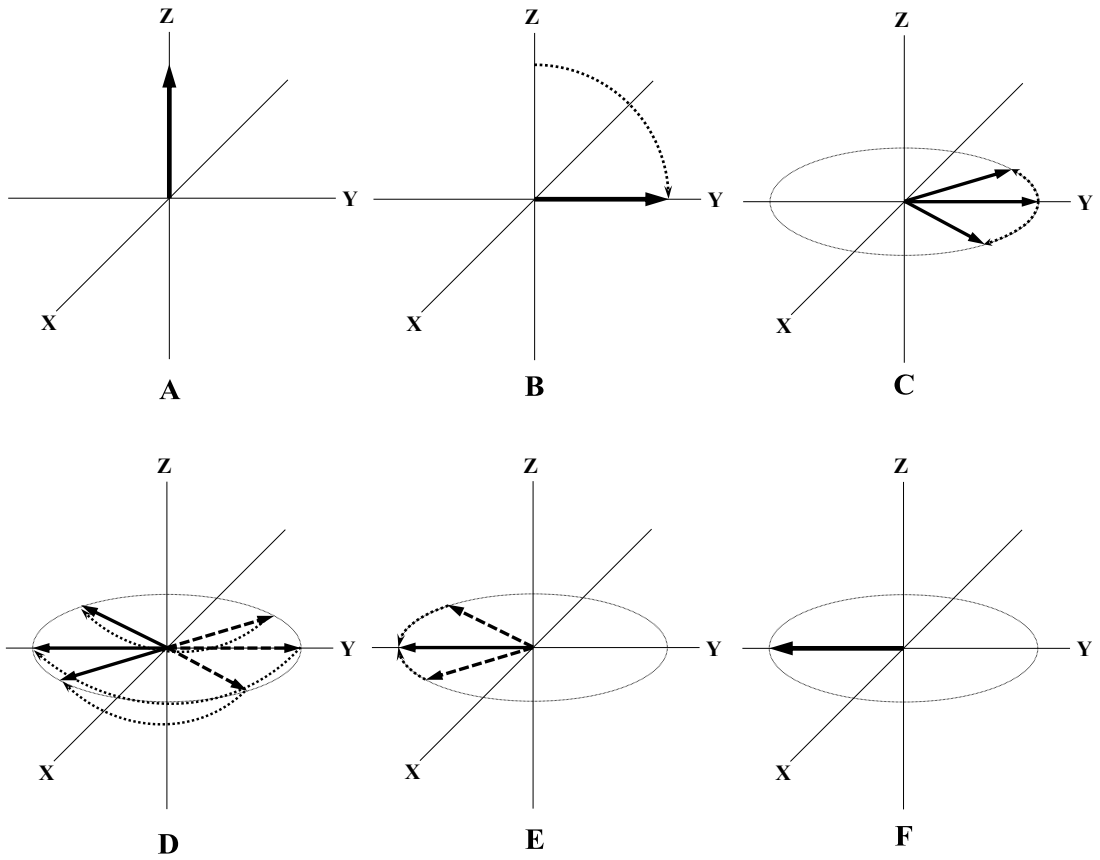

Figure 2-7. The precession of spins in the Stejskal and Tanner pulse sequence

Figure 2-7 illustrates the precession of spins during the Stejskal and Tanner pulse sequence. The arrows in the coordinate system represent an ensemble of spin magnetic moments. (A) Initially, spins are in their equilibrium status spinning on z-axis in the static magnetic field B_0. Given that the coordinate system is rotating about z-axis with an angular frequency of ω_0 ($\omega_0 = -\gamma B_0$, where γ is the gyromagnetic ratio of particles) compared to the laboratory frame of reference. Hence, the phase shifts of spins caused by static magnetic field B_0 in such a rotating reference frame are compensated. (B) Assuming that the $\pi/2$ rf pulse is imposed in x-direction, spin magnetic moments are flipped about x-axis into the equatorial plane (xy-plane) and stopped in y-axis. (C) The spin magnetic moments are considered stationary in the rotating reference frame until the presence of first magnetic gradient pulse, which would cause dephasing (fan out of spin magnetic moments in xy-plane) of the spins. We assume that the magnetic field in the center of the sample is kept constant (B_0) throughout the pulse sequence, thus net phase shifts of spins are symmetrical in both

sides of the sample, with reverse direction. (D) The following π rf pulse again flips spin magnetic moments about x-axis, reversing the sign of the phase angle of spins. (E) If the spins did not change their positions in z-direction during the period between two gradient pulses, the second magnetic gradient pulse would reverse the effect of the first one, (F) thus spin magnetic moments would refocus in the negative y-direction at the time of 2τ and give the maximum echo signal. However, in the presence of diffusion, spins which have displacement in z-axis between two gradient pulses would not be in phase (refocusing in the negative y-direction is incomplete) at t = 2τ. This would result in a phase distribution of spin magnetic moments in xy-plane at t = 2τ. The amplitude of echo signal is hence reduced.

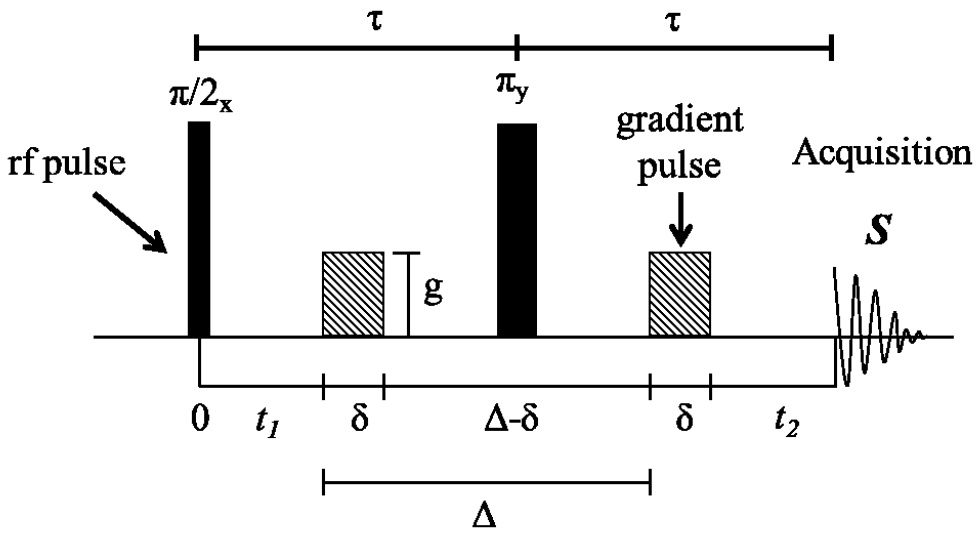

Figure 2-8. The Stejskal and Tanner pulsed-field gradient NMR sequence

In PFG NMR diffusion measurements, the diffusion coefficient (*D*) is measured using the simple Hahn spin-echo-based PFG pulse sequence (i.e. the Stejskal and Tanner sequence) shown in figure 2-8. Since this simple sequence is based on a Hahn spin-echo, the echo signal (*S*) is attenuated by both the effects of the spin-spin relaxation and of diffusion. Thus, the signal intensity is given by

$$S(2\tau) = S(0)exp\left(\frac{-2\tau}{T_2}\right) \times exp\left(-\gamma^2 g^2 D\delta^2(\Delta - \delta/3)\right)$$

$$= S(2\tau)_{g=0} \times exp\left(-\gamma^2 g^2 D\delta^2(\Delta - \delta/3)\right) \quad (2\text{-}35)$$

where the first section, $exp\left(\frac{-2\tau}{T_2}\right)$, is the attenuation due to relaxation; and the second section, $exp\left(-\gamma^2 g^2 D\delta^2(\Delta - \delta/3)\right)$, is the attenuation due to diffusion. *S(0)* is the signal immediately after the π/2 pulse, 2τ is the total echo time, T_2 is the spin-spin relaxation time of the species, γ is the gyromagnetic ratio of the observed unclears, g is the strength of the applied gradient, and δ and Δ are the duration of the gradient pulse and the separation between them, respectively. To remove the effects of the signal attenuation due to the spin-spin relaxation, we normalized the signal with respect to the signal obtained in the absence of the applied gradient and thereby defined the echo attenuation to be

$$E(2\tau) = \frac{S(2\tau)_{g=0} exp\left(-\gamma^2 g^2 D\delta^2(\Delta - \delta/3)\right)}{S(2\tau)_{g=0}}$$

$$= exp\left(-\gamma^2 g^2 D\delta^2(\Delta - \delta/3)\right) \quad (2\text{-}36)$$

By inspection of equation (2-36) with reference to figure 2-8, it can be seen that to measure diffusion, a series of experiments are performed in which either g, δ or Δ is varied while keep τ constant. Then, equation (2-36) is regressed onto the experiment data and D is straightforwardly determined.

References

[1] J. Rouqerol, D. Avnir, C. W. Fairbridge, D. H. Everett, J. H. Haynes, N. Pernicone, J. D. Ramsay, K. S. W. Sing, K. K. Unger, *Pure Appl. Chem.* **1994**, *66*, 1739.

[2] K. S. W. Sing, D. H. Everett, R. A. W. Haul, L. Moscou, R. A. Pierotti, J. Rouquérol, and T. Siemieniewska, *Pure Appl. Chem.* **1985**, *57*, 603.

[3] K. Kaneko, K. Kakei, J. *Colloid Interface Sci.* **1989**, *129*, 583.

[4] S. J. Gregg and K. S. W. Sing, *Adsorption, Surface Area and porosity*, Academic press, **1979**.

[5] K. S. W. Sing, D. H. Everett, R. A. W. Haul, L. Moscou, R. A. Pierotti, J. Roquerol, T. Siemieniewska, *Pure Appl. Chem.* **1985**, *57*, 603.

[6] S. G. Gregg, K. S. W. Sing, in "*Adsorption, Surface Area and porosity*" 2nd edition, Academic press, **1982**.

[7] T. L. Hill, *J. Phys. Chem.* **1955**, *59*, 1065.

[8] S. W. Sing, *Carbon* **1989**, *27*, 5.

[9] K. Kaneko, C. Ishii, *Colloids Surfaces* **1992**, *67*, 203-212.

[10] M. M. Dubinin, *Chem. Rev.* **1960**, *60*, 235.

[11] H. Kataura, Y. Kamazawa, Y. Maniwa, I. Umezu, S. Suzuki, Y. Ohtsuka, Y. Achiba, *Synth. Met.* **1999**, *103,* 2555.

[12] D. J. Gardiner, Practical Raman spectroscopy, *Springer-Verlag,* **1989**.

[13] J. R. Ferraro, K. Nakamoto, C. W. Brown, *Introductory Raman Spectroscopy*, Academic Press, **1998**.

[14] A. Jorio, M. Pimenta, A. Souza-Filho, R. Saito, G. Dresselhaus, M. Dresselhaus,

New J. Phys. **2003**, *5*, 139-1.

[15] L. M. Bidaut, *6th Mediterranean Electrotechnical Conference* **1991**, Proceedings Vols *1* and *2*, 1233-1237.

[16] E. Cuchet, F. Lambert, C. Derosier, *Journal of Neuroradiology* **1994**, *21*, 170-175.

[17] R. L. Delapaz, E. Herskovits, V. Digesu, W. A. Hanson, R. Bernstein, Extracting Meaning from Complex Data : Processing, Display, Interaction **1990**, *1259,* 176-181.

[18] C. L. Su, Machine Vision and Three-Dimensional Imaging Systems for Inspection and Metrology **2001**, *4189*, 63-71.

[19] A. Gossi, U. Scherer, G. Schlotterbeck, *Chimia* **2012**, *66*, 347-349.

[20] G. F. Pauli, T. Godecke, B. U. Jaki, and D. C. Lankin, *Journal of Natural Products* **2012**, *75*, 834-851.

[21] D. Jeannerat and J. Furrer, *Combinatorial Chemistry & High Throughput Screening* **2012**, *15*, 15-35.

[22] E. L. Hahn, *Physical Review* **1950**, *80*, 580-594.

[23] H. Y. Carr, E. M. Purcell, *Physical Review* **1954**, *94***,** 630-638.

[24] W. S. Price, *Concepts in Magnetic Resonance* **1997**, *9*, 299-336.

[25] E. O. Stejskal, J. E. Tanner, J*ournal of Chemical Physics* **1965**, *42*, 288-292.

Chapter 3

Nanocarbon Materials

3.1. Background

Previous discovery of nanocarbon in solid phase were known to be only exist in three allotropic forms: graphite, diamond and charcoal for a long time. In 1985, Kroto, Smalley, Curl and coworkers were successfully synthesized a new nanocarbon material which consists sixty carbon atoms called as fullerene (C_{60}) [1]. This material has received great attention in many years until the emergence of carbon nanotube. In 1991, Iijima of the NEC Laboratory elucidated the atomic structure and helical character of multi-wall carbon nanotubes, since then the interest in the carbon nanostructures was unprecedented generated [2]. Two years later, synthesis of single-walled nanotubes was independently reported by Iijima and Toshinari Ichihashi of NEC, and Donald Bethune and colleagues of the IBM Almaden Research Center in California [3, 4]. Then in 1999, Iijima et al. developed a new type of single wall nanocarbon named single wall carbon nanohorns (SWCNHs), which has a nanotubular and forms a unique assembly structure with a "Dahlia-flower-like" feature [5]. Though this is just the beginning of the study of SWCNHs, it is quite intriguing to reveal a large possibility for novel applications such as adsorbents [6–8], gas sensor [9], catalyst supports [10] and carriers of drag delivery [11]. These discovery of nanocarbon materials newly attracted great deal of interest in nano-science and the materials are expected not only to find out a nano-scale phenomena but solve the energy problem. Furthermore, in 2004 physicists at the University of Manchester and the Institute for Microelectronics Technology, Chernogolovka, Russia, first isolated individual graphene planes by using adhesive tape. They also

measured electronic properties of the obtained flakes and showed their unique properties [12]. The endeavor in carbon nanomaterials has not only broadened the field of scientific research, but also provided promising techniques for various applications. In this section a variety of nanocarbon materials will be introduced in history background, structure, synthesis method, properties and application.

3.2. Single-Walled Carbon Nanotubes

3.2.1. Structure and Chirality

Carbon nanotubes are allotropes of carbon with a cylindrical nanostructure. The structure of single-walled carbon nanotubes (SWCNTs) can be seen as a seamless rolled graphene sheet with a cylindrical nanostructure and multiwall carbon nanotubes (MWCNTs) are a collection of concentric SWCNTs [13]. Most SWCNTs have a diameter of close to 1 nanometer, with a tube length that can be many millions of times longer. The cylindrical structure of SWCNTs is assigned by diameter, chiral angle and handedness (right-handed and left-handed) [14–16]. The diameter and chiral angle are among the most important and these factors are uniquely defined by chiral vector $\boldsymbol{C}_h$. The chiral vector connects two crystallographically equivalent sites (O, A, B and B') on a two-dimensional graphene sheet in Figure 3-1 and is given by:

$$\boldsymbol{C}_h = n\boldsymbol{a}_1 + m\boldsymbol{a}_2 \equiv (n,\ m) \tag{3-1}$$

where $\boldsymbol{a}_1$ and $\boldsymbol{a}_2$ are unit vectors of the hexagonal honeycomb lattice of the graphene sheet. In Figure 3-1, the chiral vector $\boldsymbol{C}_h$ corresponds to a vector $\boldsymbol{OA}$ of the nanotube perpendicular to the tube axis. The construction of a CNT is uniquely defined by the pair of integers (n, m).

The circumferential length (L) of the CNT is given by:

$$L \equiv |C_h| = a\sqrt{n^2 + m^2 + nm} \tag{3-2}$$

where $|C_h|$ is the length of $\boldsymbol{C}_h$, a is the lattice constant ($a=1.44\text{Å}\times\sqrt{3}=2.49\text{Å}$) of the honeycomb lattice; the C-C bond length of graphite is generally 1.42 Å, but, in the case of SWCNT, the length (1.44Å) is slightly larger than graphite due to the cylindrical structure. The nanotube diameter d_t and the chiral angle θ are given by:

$$d_t = \frac{L}{\pi} = \frac{a\sqrt{n^2 + nm + m^2}}{\pi} \tag{3-3}$$

$$\theta = \tan^{-1}\left(-\frac{\sqrt{3}m}{2n+m}\right) \quad \left(|\theta| \le \frac{\pi}{6}\right) \tag{3-4}$$

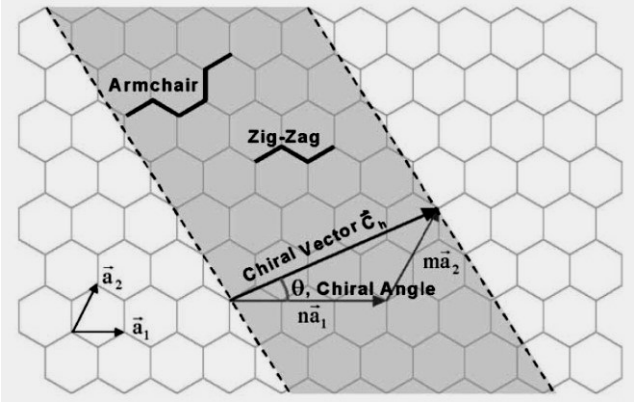

Figure 3-1. The unrolled honeycomb lattice of a nanotube [13]

From (3-4), it follows that the (n, 0) zigzag nanotube and the (n, n) armchair nanotube correspond to θ = 0° and θ = 30°, respectively. Thus the SWCNTs are classified to achiral or chiral types from the viewpoint of a symmetry. There are only two cases of achiral nanotubes; which are armchair nanotube, zigzag nanotube as shown in Figure 3-2 (a and b), respectively. In the (n, m) notation for chiral vectors, the vectors (n, n) denote armchair nanotubes and vectors (n, 0) denote zigzag nanotubes. Another nanotube exhibits a spiral symmetry. The nanotube with chirality is called chiral nanotube [(n, m)] as shown in Figure 3-2 (c). The notation of chiral nanotubes is generally considered only $0 < |m| < n$ due to the hexagonal symmetry of the honey comb lattice.

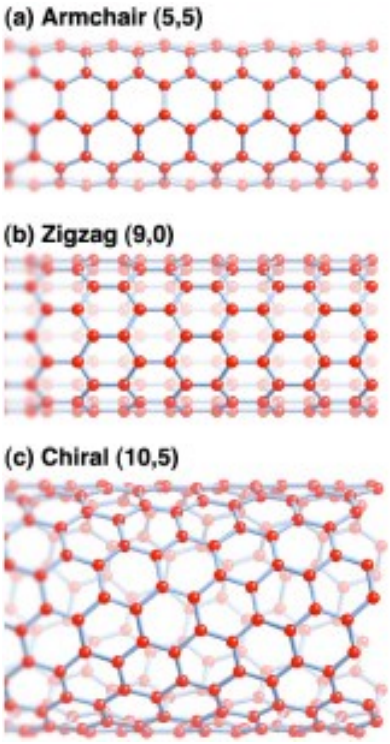

Figure 3-2. Three types of SWCNT: armchair (a), zigzag (b), and chiral (c) nanotubes.

Additionally, in order to determine a unit cell of the one-dimensional lattice, it is necessary to define a translation vector ***T***. The vector ***T*** is parallel to the tube axis and corresponds to the intersection of the vector ***OB***. The translational vector ***T*** is defined to be the normal unit vector to chiral vector $\boldsymbol{C}_h$ as shown in Figure 3-1. The lattice vector ***T*** shown as ***OB*** is given by:

$$\boldsymbol{T} = t_1\boldsymbol{a}_1 + t_2\boldsymbol{a}_2 \equiv (t_1,\ t_2) \tag{3-5}$$

From (3-1) and (3-5), t_1 and t_2 can be expressed by

$$t_1 = \frac{2m+n}{d_R},\quad t_2 = \frac{2n+m}{d_R} \tag{3-6}$$

where d_R is the highest common divisor of (2m+n) and (2n+m). In addition, d_R can be expressed in term of d. Here, d is the highest common of divisor of (n, m).

$$d_R = \begin{cases} d \text{ if } n-m \text{ is not a multiple of } 3d \\ 3d \text{ if } n-m \text{ is a multiple of } 3d \end{cases}$$

The unit lattice length (***T***) along the tube axis direction and the number of the hexagons in a unit cell (***N***) are expressed by:

$$T = \sqrt{3}\,C_h/d_R = \frac{3a_{C-C}\sqrt{n^2+m^2+nm}}{d_R} \quad or \quad T = |T| = \frac{\sqrt{3}L}{d_R} \tag{3-7}$$

$$N = \frac{2(m^2+n^2+nm)}{d_R} \tag{3-8}$$

3.2.2. Production Methods of SWCNTs

Techniques have been developed to produce nantubes in large quantities and commercial available. The main roots for SWCNT synthesis include arc-discharge, laser ablation, and chemical vapor deposition.

Nanotubes were observed in 1991 in the carbon soot of graphite electrodes during an arc discharge [2]. The schematic of laser ablation method is shown in Figure 3-3(a). In arc-discharge, carbon atoms are evaporated by plasma of helium gas ignited by high currents passed through opposing carbon anode and cathode. MWCNTs can be obtained by controlling the growth conditions such as the pressure of inert gas in the discharge chamber and the arcing current. Growth of single-walled tubes needs a metal catalyst in the arc-discharge system [4, 17].

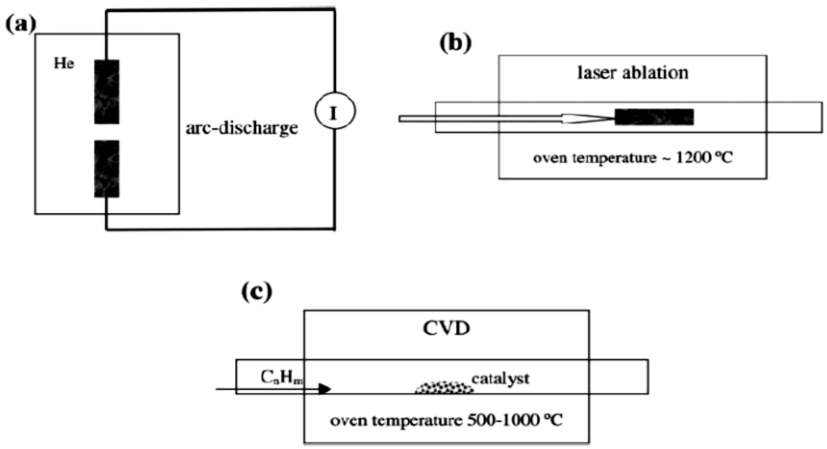

Figure 3-3. Schematic experimental setups for nanotube growth methods: (a) arc-discharge, (b) laser ablation, and (c) CVD [14].

Laser ablation was firstly introduced by Smalley group. The method utilized intense laser pulses to ablate a carbon target placed in a tube-furnace heated to 1200℃. The carbon target contained 0.5 atomic percent of nickel and cobalt. A flow of Ar was passed through the growth chamber to carry the grown nanotubes downstream to be collected on a cold finger during the ablation [18]. The schematic of laser ablation method is shown in Figure 3-3(b).

CVD is currently the best-known technology for the commercial production of carbon nanotubes [19]. During CVD, a substrate is prepared with metal catalyst particles deposited on it. The commonly used metal catalysts are nickel, cobalt, iron or a combination. The growth process involves heating a catalyst material to high temperatures in a tube furnace and flowing by a hydrocarbon gas through the tube reactor for a period of time. Nanotubes grow at the sites of the metal catalysts. After the system cool down to room temperature, the materials grown over the catalyst are collected. The key parameters in nanotube CVD growth are the hydrocarbons, catalysts and growth temperature. The schematic of laser ablation method is shown in Figure 3-3(c).

Carbon nanotubes are the strongest and stiffest materials yet discovered in terms of tensile strength and elastic modulus respectively. SWCNTs are 100 times stronger than the highest grade high carbon steel commercially available. SWCNTs also have a tensile modulus many times higher than steel; they can be stretched over five times their original length with nearly 100% memory and undetectable levels of corresponding structural damage [20-22]. But weak shear interactions between adjacent shells and tubes leads to significant reductions in the effective strength of multi-walled carbon nanotubes and carbon nanotube bundles [23].

Nanotubes are also expected to be very good thermal conductors along the tube, exhibiting a property known as “ballistic conduction”, but good insulators laterally to the tube axis. Measurements show that a SWCNT has a room-temperature thermal

conductivity along its axis of about 3500 W m^{-1} K^{-1} [24]; which is much higher than that of copper (385 W m^{-1} K^{-1})

The electronic structure of SWCNT can be either metallic or semiconducting, depending on its diameter and chirality. For a given (n, m) nanotube, if n = m, the nanotube is metallic; if n-m is a multiple of 3, then the nanotube is semiconducting with a very small band gap, otherwise the nanotube is a moderate semiconductor [25]. Some small diameter carbon nanotubes don't obey this rule due to the electrical properties change caused by curvature effects. In theory, metallic nanotubes can carry an electric current density of 4 × 109 A cm^{-2}, which is more than 1,000 times greater than those of metals such as copper [26].

Due to the above excellent properties, carbon nanotubes are expected to have different potential applications, like electrodes for electrochemical double layer capacitors [27], field-emission materials [28], nano-electronic devices [29], hydrogen storage [30], sensors [31], functional polymers [32], etc.

3.3. Activated Carbon Fiber

Activated carbon fibers (ACF) have excellent adsorptivity due to large specific surface area, pore volume, and uniform microporosity. ACF have been studied extensively both from fundamental and industrial aspects [33-35]. The adsorption property of ACF is determined by their pore width and pore-wall chemistry. The relationship between the pore width and adsorption characteristics has been actively studied [36-38]. As to the pore wall chemistry, the pore-walls of ACF are partially oxidized or modified with other chemical substances in order to get better adsorbents or catalysts [39-42].

The production of highly effective fibrous carbon adsorbents with low diameter, excluding or minimizing external and intra mass transfer resistance, and exhibiting high adsorption rates, is a challenging task for researchers in the science and technology of adsorption. As the name implied, ACF are fibrous morphology, but

activated carbon were generally produced with the form of granular. Activated carbon fiber possesses a relatively uniform porosity (mainly microporosity) in comparison with that of more conventional activated carbon.

Usually speaking, industrial ACF have three kinds of cross-section forms: radial, random, and onion, showed in Figure 3-4 [43].

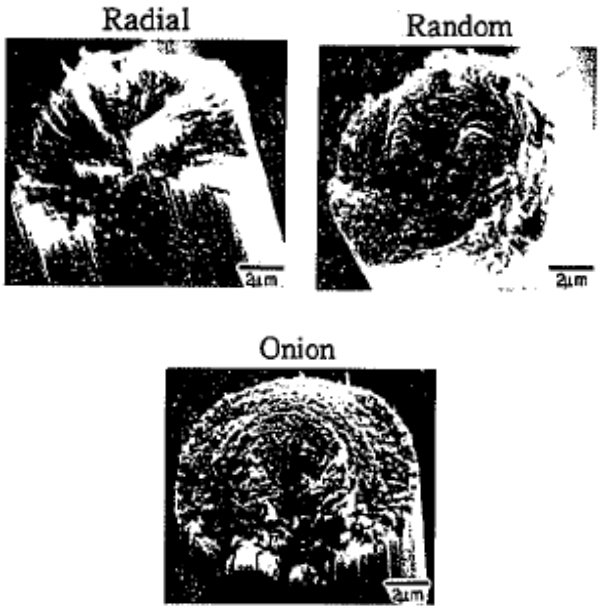

Figure 3-4 the cross-section of pitch-based ACF with different structure [43]

There are several a kind of activated carbon fiber are made from cellulose, polyacrylonitrile (PAN), phenol resin, pitch and other organic materials, in this study, the ACF were prepared from petroleum-derived isotropic pitch precursors using melt-blown spinning.

Microporous materials are classified into crystalline and less-crystalline types. Activated carbon fiber (ACF) is a kind of less-crystalline carbon material which consisting of a three-dimensional network of 2 to 3 nm micrographitic units, the edges of micrographitic units are covered with functional groups and dangling bonds. Each micrographitic unit is formed with a stack of 3 to 4 layers of nanosized graphene sheets. The micrographitic unit network gives a micropore network as its reversal,

where micropores are suggested to be characterized as slit-shaped pores due to the micrographitic unit based microstructure of ACF [44, 45]. Gas adsorption is driven mainly by molecular potentials of micrographitic units, which are enhanced by the presence of two micrographitic unit surfaces surrounding the flat-shaped narrow space of a micropore from both sides [46].

ACF is the representative of microporous carbons consisting of disordered nanographites. Due to the excellent mechanical feature, ACF can be woven into belt or cloth forms, using for strengthening bridges, tunnels and buildings; due to the electrical feature, ACF can be used to manufacture supercapacitor, and due to the high surface area and pore volume, ACF can also be used as adsorbent [47, 48]. The morphology of ACF can eliminate the problems caused by powder or granular activated carbon.

References

[1] H. W. Kroto, J. R. Heath, S. C. O'Brien, R. F. Curl, R. E. Smalley, *Nature* **1985** *318*, 162.

[2] S. Iijima, *Nature* **1991**, *354*, 56.

[3] S. Iijima, T. Ichihashi, *Nature* **1999**, *363*, 603.

[4] D. S. Bethunem, C. H. Kiang, M. S. de Vries, G. Gorman, R. Savoy, R. Beyer, *Nature* **1993**, *363*, 605.

[5] S. Iijima, M. Yudasaka, R. Yamada, S. Bandow, K. Suenaga, F. Kokai, *Chem. Phys. Lett.* **1999**, *309*,165.

[6] E. Bekyarova, K. Murata, M. Yudasaka, D. Kasuya, S. Iijima, and K. Kaneko, *J. Phys. Chem. B* **2003**, *107*, 4681.

[7] K. Murata, K. Hirahara, M. Yudasaka, D. Kasuya, S. Iijima, and K. Kaneko, *J. Phys. Chem. B* **2002**, *106*, 12668.

[8] H. Tanaka, H. Kanoh, M. E. Merraoui, W. A. Steele, M. Yudasaka, S. Iijima, and K. Kaneko, *J. Phys. Chem. B* **2004**, *108*, 17457.

[9] J. Zhu, D. Kase, K. Shiba, D. Kasuya, M. Yudasaka, and S. Iijima, *Nano Lett.* **2003**, *3*, 1033.

[10] R. Yuge, T. Ichihashi, Y. Shimakawa, Y. Kubo, M. Yudasaka, and S. Iijima, *Adv. Mat.* **2004**, *16*, 1420.

[11] K. Ajima, M. Yudasaka, T. Murakami, A. Maigne, K. Shiba, and S. Iijima, *Mol. Pharmaceutics* **2005**, *2*, 475.

[12] K. S. Novoselov, A. K. Geim, S. V. Morozov, D. Jiang, Y. Zhang, S. V. Dubonos, I. V. Grigorieva, A. A. Firsov, *Science* **2004**, *306*, 666.

[13] E. Thostenson, Z. Ren, T. Chou, *Comp. Sci. Technol.* **2001**, *61*, 1899.

[14] M. S. Dresselhaus, G. Dresselhaus, and Ph. Avouris, *Carbon Nanotubes; Synthesis, Structure, Properties, and Applications* (Springer, NewYork, **2001**).

[15] M. S. Dresselhaus, G. F. Dresselhaus, and P. C. Eklund, *Science of Fullerenes and Carbon Nanotubes* (Academic Press, New York, **1996**).

[16] N. Hamada, S. Sawada, and A. Oshiyama, *Phys. Rev. Lett*. **1992**, *68*, 1597.

[17] T. W. Ebbesen, P. M. Ajayan, *Nature* **1992**, 358, 220.

[18] C. Journet, W. K. Maser, P. Bernier, A. Loiseau, M. Lamyde la Chapelle, S. Lefrant, P. Deniard, R. Lee, J. E. Fischer, *Nature* **1997**, 388, 756.

[19] L. Delzeit, C. V. Nguyen, R. M. Stevens, J. Han, and M. Meyyappan, *Nanotechnology* **2002**, 13, 280.

[20] R. S. Ruoff, D. C. Lorents, *Carbon* **1995**, 33, 925.

[21] M. F. Yu, O. Lourie, M. J. Dyer, K. Moloni, T. F. Kelly, R. S. Ruoff, *Science* **2000**, 287, 637.

[22] M. F. Yu, B. S. Files, S. Arepalli, R. S. Ruoff, *Phys. Rev. Lett.* **2000**, 84, 5552.

[23] T. Filleter, R. Bernal, S. Li, H. D. Espinosa, *Adv. Mater.* **2011**, 23, 2855.

[24] E. Pop, D. Mann, Q. Wang, K. Goodson, H. Dai, *Nano Lett.* **2005**, 6, 96.

[25] X. Lu, Z. Chen, *Chem. Rev.* **2005**, 105, 3643.

[26] Hong, Seunghun, S. Myung, *Nature Nanotec.* **2007**, 2, 207.

[27] J. H. Chen, W. Z. Li, D. Z. Wang, S. X. Yang, J. G. Wen, Z. F. Ren, *Carbon* **2002**, 40, 1193.

[28] J. M. Bonard, H. Kind, T. Stockli, L. O. Nilsson, *Solid State Electron* **2001**, 45, 893.

[29] K. Tsukagoshi, N. Yoneya, S. Uryu, *Physica B* **2002**, 323, 107.

[30] A. C. Dillon, K. M. Jones, T. A. Bekkedahl, C. H. Kiang, D. S. Bethune, M. J. Heben, *Nature* **1997**, 386, 377.

[31] A. B. Artyukhin, M. Stadermann, R. W. Friddle, P. Stroeve, O. Bakajin, A. Noy, *Nano Lett.* **2006**, 6, 2080.

[32] S. J. Tans, M. H. Devoret, H. Dai, A. Thess, R. E. Smalley, L. J. Geerligs, *Nature* **1997**, 386, 474.

[33] K. Kaneko, *Studies in Surface Science and Catalysis* **1993**, 99, 573.

[34] K. Kaneko, *J. Membrane Sci.* **1994**, 96, 59.

[35] K. Kaneko, *Studies in Surface Science and Catalysis* **1998**,120, 635.

[36] T. Iiyama, K. Nishikawa, T. Otowa, T. Suzuki, K. Kaneko, B. McEnaney, T. J. May, J. Rouquerol, F. Rodriguez-Reinoso, K. S. W. Sing, K. K. Unger, *Characterisation of Porous Solids IV*, London: Royal Society of Chemistry, **1998**, 41-48.

[37] Z. M. Wang, K. Kaneko, *J. Phys. Chem. B* **1998**, *102*, 2863.

[38] T. Ohkubo, T. Iiyama, K Nishikawa, T. Suzuki, K. Kaneko, *J. Phys. Chem. B* **1999**,*103*, 1859.

[39] C. Marquez-Alvarez, I. Rodriguez-Ramos, A. Guerrero-Ruiz, *Carbon* **1996**, *34*, 1509.

[40] K. Kaneko, A. Kobayashi, T. Suzuki, S. Ozeki, K. Kakei, N. Kosugi, H. Kuroda, *J. Chem. Soc., Faraday Trans. 1* **1988**, *84*, 1795.

[41] K. Kaneko, N. Kosugi, H. Kuroda, *J. Chem. Soc., Faraday Trans. 1* **1989**, *85*, 869.

[42] K. Kaneko, *Colloids and Surface* **1989**, *37*, 115.

[43] Structure and Properties of Pitch-based carbon fibers, *Nippon steel technical report* No.*59*, October **1993**.

[44] J. R. Fryer, *Carbon* **1981**, *19*, 431.

[45] T. Suzuki, K. Kaneko, N. Setoyama, M. Maddox, and K. Gubbins, *Carbon* **1996,** *34*, 909.

[46] K. Kaneko, C. Ishii, M. Ruike, and H. Kuwabara, *Carbon* **1992**, *30*, 1075.

[47] D. Lozano-Castelló, D. Cazorla-Amorós, A. Linares-Solano, and D. F. Quinn, *Carbon* **2002,** *40*, 989.

[48] J. Alcañiz-Monge, De M. A. La Casa-Lillo, D. Cazorla-Amorós, and A. Linares-Solano, *Carbon* **1997,** *35*, 291.

Chapter 4

Electron density control of SWCNT by liquid-phase molecular adsorption of hexaiodobenzene

4.1. Introduction

Since their discovery [1], single wall carbon nanotubes (SWCNT) have attracted considerable attention in widely diverse fields owing to their remarkable mechanical, thermal and electrical properties [2–4]. More recently, studies on the electrical properties of SWCNT have focused on the charge transfer interaction of SWCNT with electron donor or acceptor molecules that allow the manipulation of electrical conductivity of SWCNT [5–7]. Conventional modification of SWCNT has been realized by intercalation with iodine or halogenides of Na, K, Rb, Cs, Ca, Cu, and Ag through gas phase doping or liquid phase adsorption methods [8–13]. These SWCNT modified with metal halogenides always show a p-type behavior, which means that electrons are always withdrawn from the valence band of SWCNT to the adsorbates and the main charge carrier in the SWCNT are holes. However, this empirical rule was disproved by Jung et al. [14], who observed a slight down-shift of a C1s peak in the X-ray photoelectron spectra upon iodine intercalation, indicating that iodine can act as a weak electron donor for SWCNT. They also proved that the iodine has a partial positively charged state of $I^{+0.08-0.1}$ by I LI-edge X-ray absorption near-edge structure (XANES) analysis. Hayakawa et al. [8] reported that the adsorption of iodine also leads to a dramatic enhancement in the conductivity of SWCNT. Hexaiodobenzene (HIB, C_6I_6) molecules exhibit a two-electron oxidation that generates a di-cation $(C_6I_6)^{2+}$ from HIB (C_6I_6) [15]. In addition, $(C_6I_6)^{2+}$ shows σ-aromaticity co-existing with the conventional π-aromaticity that it shares with its

neutral parent [16]. Because of the unique electronic structure of HIB, in this study, SWCNT were modified by HIB adsorption through a liquid-phase adsorption method. Spectroscopic techniques, such as UV-Vis-NIR adsorption, Raman, and X-ray photoelectron spectroscopy, were employed to understand the electron-density changes of SWCNT after the HIB adsorption. Quantitative analysis of the adsorbed amounts was also carried out by a thermogravimetric method.

4.2. Experimental

4.2.1. HIB-Adsorbed SWCNTs Preparation

Super-growth SWCNTs were synthesized by a chemical vapor deposition (CVD) process (Center of Advanced Carbon Materials, AIST). The SWCNTs samples were used without further purification because of their high carbon purity (higher than 99.98 %) [17]. Tube caps of as-prepared SWCNTs were removed by oxidation at 773 K under Ar and O_2 mixed gases for 1 h. For the preparation of HIB-adsorbed SWCNTs, a typical procedure was as follows: 3 mg of SWCNT were dispersed in 50 mL tetrahydrofuran (THF) solution by ultra-sonication using an ultrasonic cleaner (FU-50C, 28 kHz) at 298 K for 2 days. Afterwards, hexaiodobenzene (HIB) (2.31 mg and 6.36 mg) was added to the SWCNT dispersion, and the mixture was further dispersed by sonication for 15 mins. The samples were denoted as HIB@SWCNT-*l* and HIB@SWCNT-*h*, respectively.

Then, the mixture was moved into a water bath, and kept at the temperature of 298 K for 1 week to reach the adsorption equilibrium. After filtration, the remaining solid was washed with THF to remove free HIB molecules and dried under vacuum at 373 K overnight. After the analysis, a HIB@SWCNT-*h* sample was further heat-treated up to 1273 K at a rate of 5 K min^{-1} under N_2 at a flow rate of 100 cm^3 min^{-1}. This sample was denoted as HIB@SWCNT-HTT.

4.2.2. Characterization

Thermogravimetric analysis (TGA) was performed on a thermo-gravimetric analyzer (Shimadzu; DTG-60AH) at a heating rate of 5 K min^{-1} and N_2 flow rate of

100 cm^3 min^{-1}. The changes in the electronic properties of SWCNTs upon HIB adsorption were measured through the following methods. Raman spectra of each sample were measured on a dried solid by Raman spectrometer (JASCO; NRS-3100) with the excitation wavelength of 532 nm (power 0.1 mW). X-ray photoelectron spectra (XPS) were measured with X-ray photoelectron spectrometer (JEOL; JPS-9010MX) using monochromatized MgKα radiation as a photon source. The optical absorption spectra (UV-Vis-NIR spectrophotometer, JASCO, V-670) were measured on an HIB-adsorbed SWCNT solution, which was prepared by dispersing HIB-adsorbed SWCNT in THF (20 mg L^{-1}) by ultra-sonication for 24 h. High-resolution transmission electron microscopy (HRTEM; JEOL, JEM-2100F) was carried out by drop-casting dispersed solution of HIB-adsorbed SWCNT onto carbon-film-supported copper grids. To measure the HIB adsorption effect on the electrical conductivity of SWCNTs, the sheet resistance was measured using a four-point probe method [18] at room temperature. The SWCNTs and HIB-adsorbed SWCNT dispersions were coated on a polyethylene terephthalate (PET) substrate by a spray-coating method.

4.3. Results and Discussions

TGA provides a quantitative way to determine the thermal stability of SWCNT as well as the amount of HIB molecules adsorbed on SWCNTs. The TGA curves of HIB, SWCNT, HIB@SWCNT-*l* (46.2 mg L^{-1}), and HIB@SWCNT-*h* (127.2 mg L^{-1}) are shown in Figure 4-1. The TGA curve of SWCNT shows only 0.8% weight loss until 800 K. This indicates the high purity and high thermal stability of SWCNT. The inset graph shows that the weight loss of HIB starts from 520 K, and it is complete at 850 K, which corresponds to the decomposition of HIB. Therefore, the weight loss ranging from 520 K to 850 K in the TGA curve of HIB-adsorbed SWCNT can be attributed to the decomposition of adsorbed HIB. In this range the weight loss is about 15.0 wt.% of the total mass for HIB@SWCNT-*l* and 18.6 wt.% for HIB@SWCNT-*h*, respectively. The amount of adsorbed HIB per gram can be calculated by the following equation:

$$\text{Adsorbed amount} = \frac{m_{HIB}}{m_{SWCNT}} = \frac{wt.\%\ of\ HIB}{1 - wt.\%\ of\ HIB} \times 1000, \left(\frac{mg}{g}\right)$$

where m_{HIB} is the mass of HIB adsorbed on SWCNTs, m_{SWCNT} is the mass of SWCNTs, and wt% is weight loss. By this equation, the calculated amount of adsorbed HIB is about 176.5 mg g^{-1} for HIB@SWCNT-*l* and 228.5 mg g^{-1} for HIB@SWCNT-*h*.

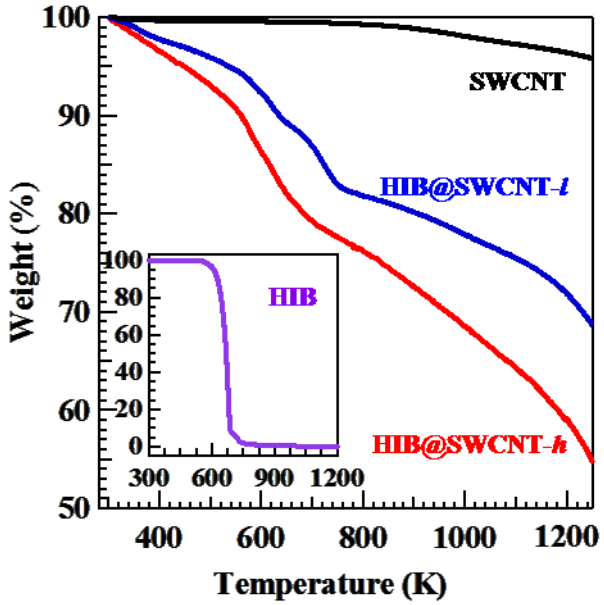

Figure 4-1. TGA curves of HIB (inset), SWCNT, HIB-adsorbed SWCNTs with different HIB concentration of 46.2 mg L^{-1} and 127.2 mg L^{-1} are denoted as HIB@SWCNT-*l* and HIB@SWCNT-*h*, respectively.

Figure 4-2 shows the UV-Vis-NIR absorption spectra of SWCNT, HIB@SWCNT-l, and HIB@SWCNT-h. The UV-Vis-NIR spectrum of SWCNT has the absorption bands in the range of 1200–2100 nm (S_{11}), 700–1100 nm (S_{22}), and 500–700 nm (M_{11}), originating from the interband electronic transitions of van Hove singularities in semiconducting and metallic SWCNT [19].

The change in S_{11} transition after the HIB adsorption indicates the charge transfer between HIB and SWCNT. Furthermore, it should be noted that the intensities of these peaks decrease with increasing the adsorbed amount of HIB and they almost disappear with higher adsorption. This effect can be interpreted either as the withdrawal of electrons from the valence band (i.e., p-type doping) or as the injection

of electrons to the conductance band (i.e., n-type doping) in semiconducting SWCNT [10]. However, the direction of electron transfer cannot be determined only from the absorption spectra since it depends on the band edge alignment between SWCNT and the redox potential of HIB molecules. The slight decrease of peak intensity of M_{11} indicates the weak interaction between metallic SWCNT and adsorbed HIB.

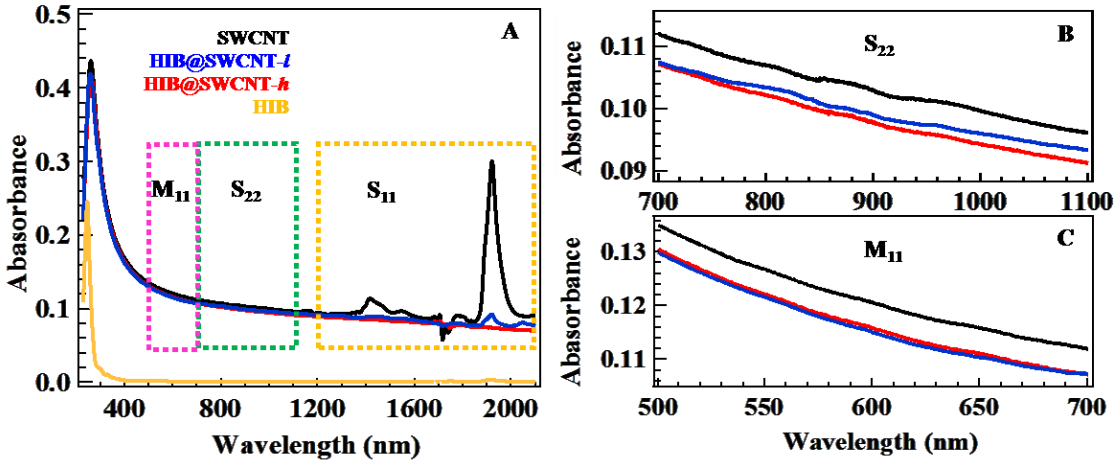

Figure 4-2. NIR absorption spectra of SWCNT, HIB@SWCNT-*l*, and HIB@SWCNT-*h* dispersed in THF at room temperature.

Figure 4-3 shows the Raman spectra of SWCNT, HIB@SWCNT-*l*, HIB@SWCNT-*h,* and HIB@SWCNT-HTT at the radial breathing mode (RBM) region. In liquid-phase adsorption, the influence of the solvent cannot be neglected. In order to examine the contributions of HIB or THF to the Raman spectrum, the spectrum of SWCNT/THF (prepared by dispersing an identical amount of SWCNT in THF) is also shown in Figure 4-3 (green line). The peak at 169.8 cm^{-1} shifted to the lower-frequency side after the adsorption of HIB: the observed shift was 3.4 cm^{-1} for HIB@SWCNT-*l* and 5.8 cm^{-1} for HIB@SWCNT-*h*. Further, a significant decrease in the intensities of all the other peaks (from 250 cm^{-1} to 300 cm^{-1} and from 100 cm^{-1} to 150 cm^{-1}) was observed: in particular, the peaks at 140 cm^{-1} disappeared completely. However, SWCNT/THF shows no significant change in this region. This indicates that the changes in the electronic density of SWCNT can be attributed to the HIB

adsorption but not to THF, and it is further confirmed by HIB@SWCNT-HTT. In the Raman spectrum of HIB@SWCNT-HTT, all peaks are restored to their original state after the removal of HIB molecules from SWCNT by heat-treatment. The disappearance of RBM peak at 140.0 cm^{-1}; suggests a loss of resonance from the nanotubes with a diameter of 1.74 nm (at 140.0 cm^{-1}, calculated by $\omega_{HIB} = 232/d + 6.5$ [20]) upon the adsorption of a charge transfer molecule into SWCNT. This also testifies to a structural deformation of the SWCNT caused by the contraction of the SWCNT upon crystallization of HIB inside the tubes [21]. This result provides evidence for the effective charge transfer between SWCNT and HIB, and also suggests that the effect of HIB adsorption on the electronic structure is dependent on the chirality of SWCNT.

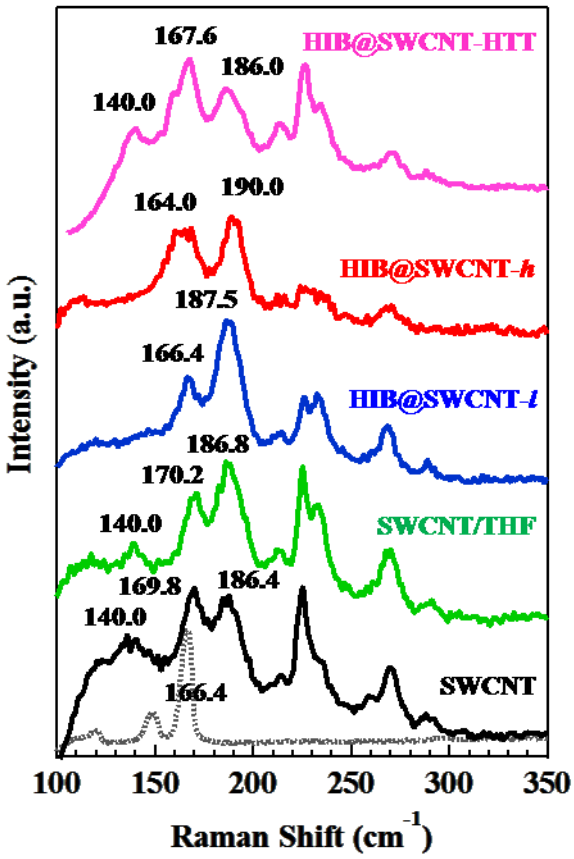

Figure 4-3. Raman spectra at the RBM region of SWCNT, SWCNT/THF without HIB addition, HIB@SWCNT-*l*, HIB@SWCNT-*h*, and HIB@SWCNT-HTT. The spectrum of solid HIB (dash line) is shown as a reference.

It should be noted that the Raman spectra of HIB-adsorbed SWCNT are shifted both towards higher and lower frequencies. In detail, the small blue-shifts of the peak at 169.8 cm^{-1} (by 3.4 cm^{-1} for HIB@SWCNT-l, and 5.8 cm^{-1} for HIB@SWCNT-h) should be caused by a convolution of the peak at 169.8 cm^{-1} of SWCNT and 166.4 cm^{-1} of HIB. On the other hand, the peak at 186.4 cm^{-1} displays a red-shift upon the HIB adsorption, which points to the hardening of radial breathing motion of carbon atoms in SWCNT with a diameter of 1.29 nm [12, 22]. The origin of this shift can be attributed either to an increase in C–C binding energy due to the charge transfer from SWCNT to HIB or, probably, to the mechanical hindrance such as the hardening and stiffening of C–C bonds [12, 23, 24]. From the TEM images of HIB-adsorbed SWCNT shown in Figure 4-4, we found that HIB molecules are distributed inside the tubes, but the binding states and orientation of HIB molecules adsorbed on SWCNT are difficult to resolve, because of the limited resolution.

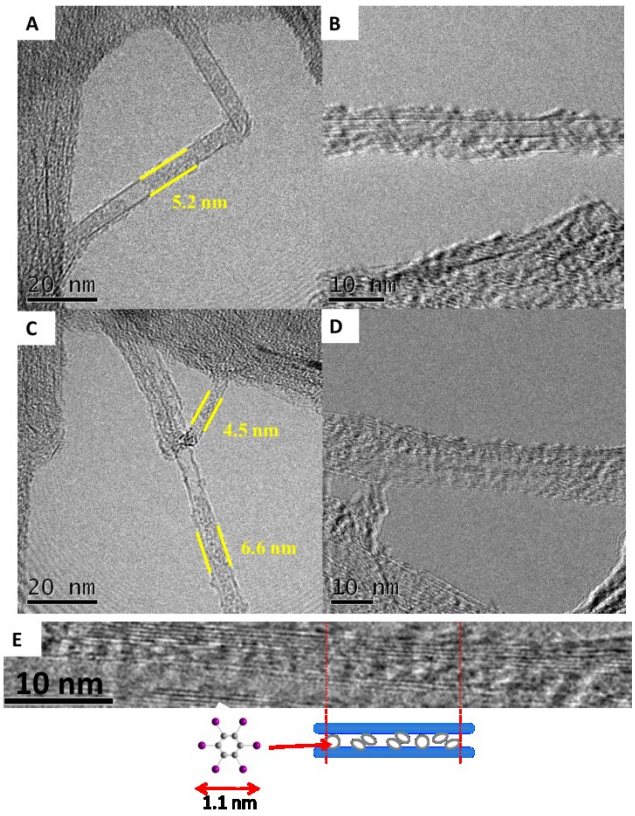

Figure 4-4. TEM images of HIB@SWCNT.

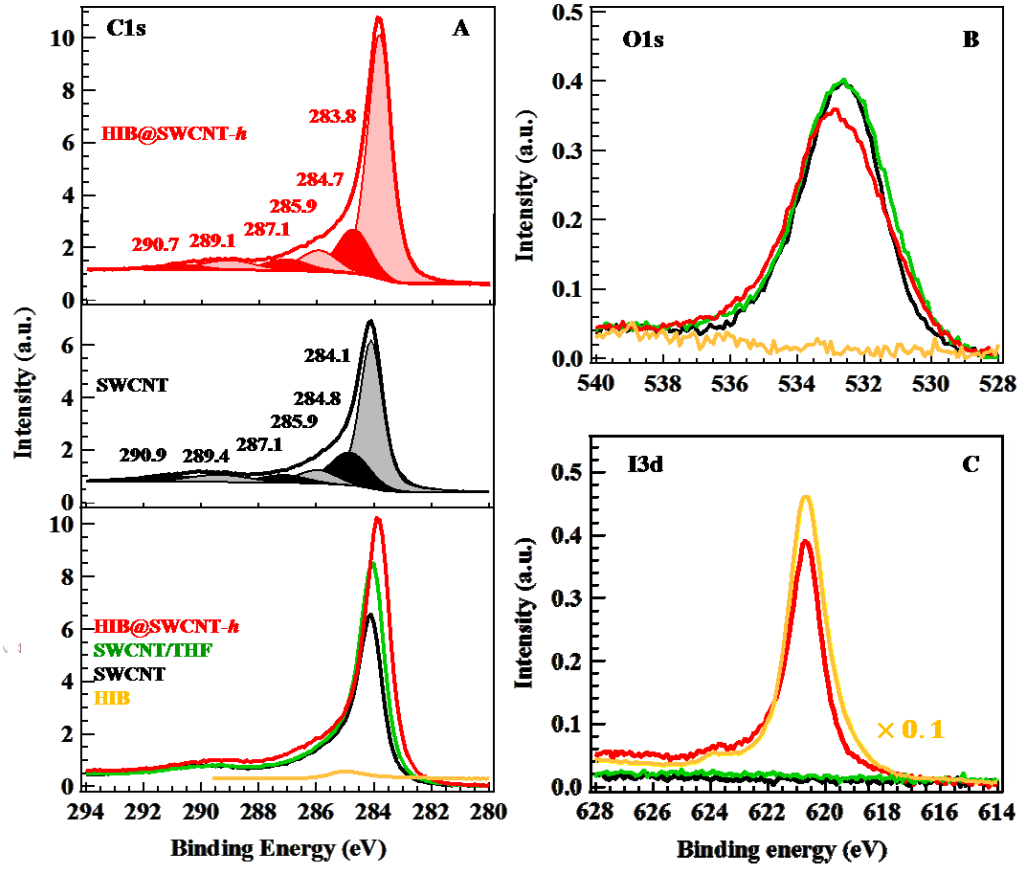

Figure 4-5. XPS spectra of the binding energy of C1s (A), O1s (B), and I3d (C) of SWCNT (black), SWCNT/THF (green), and HIB@SWCNT-*h* (red). The sub-peaks in each spectrum were obtained from peak fitting results by using Lorentzian/Gaussian function.

Systematic XPS analyses were performed to understand the direction of charge transfer between SWCNT and HIB molecules. Figure 4-5 shows the C1s, O1s, and I3d XPS spectra of HIB, SWCNT, SWCNT/THF, and HIB@SWCNT-h. Peak fitting involving a combined Lorentzian and Gaussian function was performed to give better understanding on the origins of binding energies. The most intense C1s peak at around 284.1 eV (Figure 4-5A) is comparable to the C1s binding energy of graphite and is assigned to sp^2-hybridized carbons on the tube walls. A smaller speak at around 284.8 eV is related to sp^3-hybridized carbons and may originate from the presence of defects on the tube walls [25]. The other small peaks around 285.9, 287.0, 289.5 and

290.8 eV are assigned to C–O, C=O, O–C=O and π–π* plasmon, respectively [26–28]. The sp^2 peak shows an obvious shift by 0.3 eV towards the lower binding energy side (from 284.1 to 283.8 eV) upon the HIB adsorption, evidencing the charge transfer between SWCNT and HIB. The downshift of the binding energy, consistent with the shift in Fermi level toward the valence band edge, can be interpreted as evidence of the decrease in the electron density in the SWCNT with adsorbed HIB, indicating a charge transfer from SWCNT to HIB. A similar behavior was reported by Mistry et al. [29] for nitric-acid-treated SWCNT, and Eliseev et al. [12] for AgX doped SWCNT. In the O1s XPS spectra in Figure 4-5B, the slight shift in the peak position and the small change in the peak shape of the SWCNT upon HIB adsorption indicate that the charge transfer interaction takes place not only between the HIB and π-electron system of SWCNT, but also between the iodine of HIB and the oxygen on the SWCNT, which formed in the oxidation process for the removal of tube caps.

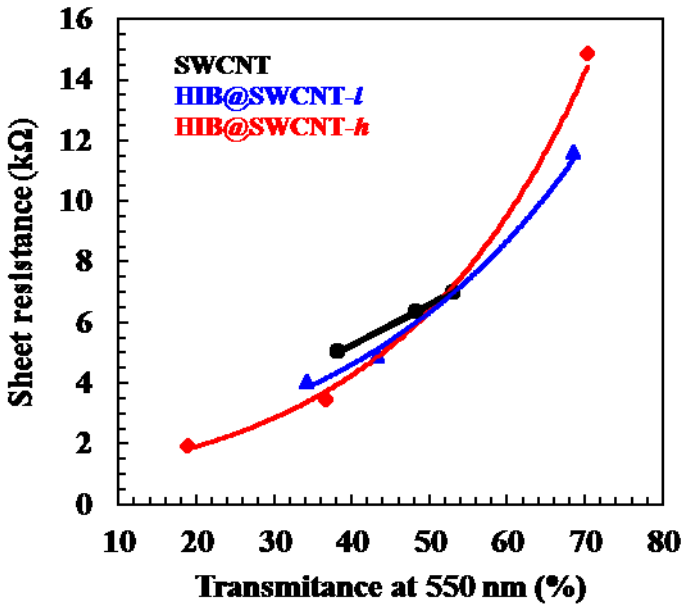

Figure 4-6. The relation between sheet resistance and sheet transmittance as prepared. There among, black curve attributed to SWCNTs, blue curve attributed to HIB@SWCNT-*l* and red curve attributed to HIB@SWCNT-*h*.

Moreover, from our conductivity measurement (Figure 4-6), the electrical conductivity of SWCNTs is effectively enhanced after HIB adsorption. For instance, as shown in Figure 4-6, since the area of all the prepared film are identical (1×2.5 cm^2) , the value of conductance will be controlled by the thickness of film and conductivity of the material. For the estimation of thickness of SWCNTs films, we used an optical absorbance at 550 nm wavelength as incident light source because HIB molecules have no absorption at 550 nm and SWCNTs have no specific absorption band at 550 nm as shown in Figure 4-7(a), and (b). The transmittance of three different thickness films of SWCNTs, HIB@SWCNT-*l* and HIB@SWCNT-*h* were measured by the optical absorbance measurement. When the transmittance of three films made by different material is the same, we can assume that the thickness of the film should be the same. In figure 4-6 (red and blue lines), indicating the conductivity measurement of films having different thickness, the HIB-adsorbed SWCNTs films show much more prominent change dependent on the film thickness than SWCNTs films (black line), especially HIB@SWCNT-*h*.

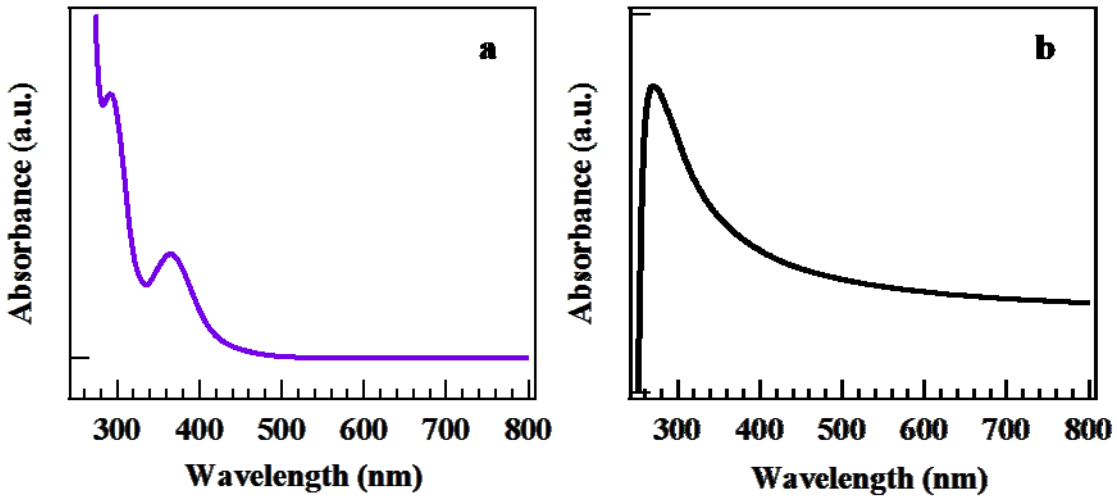

Figure 4-7. UV-Vis absorption spectra of HIB (a) and SWCNT (b) dispersed in THF at room temperature. The absorption of HIB shows starts at 450 nm and the absorption of SWCNTs shows starts at 800nm.

4.4. Conclusions

By using liquid-phase molecular adsorption of HIB to SWCNT, the electronic structure of SWCNT could be modified. The electronic structure changes of SWCNT were investigated by spectroscopic methods. UV-Vis-NIR absorption spectra analysis showed that the interaction of HIB could induce a change in the electron density of state in SWCNT. The disappearance of the RBM-peak at 140 cm^{-1} and an up-shift in the RBM-band at 186.4 cm^{-1} provide evidence for the effective charge transfer from SWCNT to HIB. The slight downshift of C1s XPS peak revealed a slight oxidation of carbon in SWCNT upon HIB adsorption. From these results, we conclude that HIB act as an electron acceptor for SWCNT.

References

[1] S. Iijima. *Nature* **1991**, *354*, 56-58.

[2] T. W. Odom, J. L. Huang, P. Kim, C. M. Lieber. *Nature* **1998**, *391*, 62-64.

[3] R. R. He, H. Z. Jin, J. Zhu, Y. J. Yan, X. H. Chen, *Phys. Lett.* **1998**, *298*, 170-176.

[4] P. Chen, X. Wu, X. Sun, J. Lin, W. Ji, K. L.Tan. *Phys. Rev. Lett.* **1999**, *82*, 2548-2551.

[5] M. Shiraishi, S. Swaraj, T. Takenobu, T. Y. Iwasa, M. Ata, W. E. S. Unger. *Phys. Rev. B* **2005**, *71*, 12549.

[6] R. Voggu, C. S. Rout, A. D. Franklin, T. S. Fisher, C. N. R. Rao. *J. Phys. Chem. C* **2008**, *112*, 13053-13056.

[7] C. N. R. Rao, R. Voggu. *Mater. Today* **2010**, *13*, 34-40.

[8] C. Hayakawa, K. Urita, T. Ohba, H. Kanoh, K. Kaneko. *Langmuir* **2009**, *25*, 1795-1799.

[9] A. M. Rao, P. C. Eklund, S. Bandow, A. Thess, R. E. Smalley. *Nature* **1997**, *388*, 257-259.

[10] N. Minami, S. Kazaoui, R. Jacquemin, H. Yamawaki, K. Aoki, H. Kataura, Y. Achiba. *Synth. Metal*. **2001**, *116*, 405-409.

[11] F. Khoerunnisa, T. Fujimori, T. Itoh, H. Kanoh, T. Ohba, M. Yudasaka, S. Iijima, K. Kaneko. *Chem. Phys. Lett.* **2001**, *501*, 485-490.

[12] A. A. Eliseev, L. V. Yashina, M. M. Brzhezinskaya, M. V. Chernysheva, M. V. Kharlamova, N. I. Verbitsky, A. V. Lukashin, N. A. Kiselev, A. S. Kumskov, R. M.

Zakalyuhin, J. L. Hutchison, B. Freitag, A. S. Vinogradov. *Carbon* **2010**, *48*, 2708-2721.

[13] S. Ghosh, S. R. K. C. Sharma Yamijala, S. K. Pati, C. N. R. Rao. *RSC Advances* **2012**, *2*, 1181-1188.

[14] Y. Jung, S. J. Hwang, S. J. Kim. *J. Phys. Chem. C* **2007**, *111*, 10181-10184.

[15] D. J. Sagl, J. C. Martin. *J. Am. Chem. Soc.* **1988**, *110,* 5827-5833.

[16] R. W. A. Havenith, P. W. Fowler, S. Fias, P. Bultinck. *Tetrahedron Lett*. **2008**, *49*, 1421-1424.

[17] K. Hata, D. N. Futaba, K. Mizuno, T. Namai, M. Yumura, S. Iijima. *Science* **2004**, *306*, 1362-1364.

[18] S. F. Smits. *Bell Sys. Tech. J.* **1958**, 711-718.

[19] H. Kataura, Y. Kumazawa, Y. Maniwa, I. Umezu, S. Suzuki, Y. Ohtsuka, Y. Achiba. *Synthet. Met.* **1999**, *103*, 2555-2558.

[20] L. Alvarez, A. Righi, T. Guillard, S. Rols. *Chem. Phys. Lett*. **2000**, *316*, 186-190.

[21] A. A. Eliseev, M. V. Kharlamova, M. V. Chernysheva, A. V. Lukashin, Y. D. Tretyakov, A. S. Kumskov, N. A. Kiselev. *Russian Chemical Reviews* **2009**, *78*, 833-854.

[22] S. Gotovac, H. Honda, Y. Hattori, K. Takahashi, H. Kanoh, K. Kaneko. *Nano Lett*. **2007**, *7*, 583-587.

[23] B. Botka, Á Pekker, Á Botos, K. Kamarás, R. Hackl. *Phys. Status Solidi B* **2010***, 247,* 2843–2846.

[24] M. A. Loi, J. Gao, F. Cordella, P. Blondeau, E. Menna, B. Bártová, C. Hébert, S. Lazar, G. A. Botton, M. Milko, C. Ambrosch-Draxl. *Adv. Mater.* **2010***, 22,* 1635–1639.

[25] S. Utsumi, H. Honda, Y. Hattori, H. Kanoh, K. Takahashi, H. Sakai, M. Abe, M. Yudasaka, S. Iijima, K. Kaneko. *J. Phys. Chem. C* **2007**, *111*, 5572-5575.

[26] J. Liu, M. R. I. Zubiri, M. Dossot, B. Vigolo, R. H. Hauge, Y. Fort, J. J. Ehrhardt, E. McRae. *Chem. Phys. Lett.* **2006**, *430*, 93-96.

[27] B. I. Rosario-Castro, E. J. Contes, M. E. Perez-Davis, C. R. Cabrera. *Rev. Adv. Mater. Sci.* **2005**, *10*, 381-386.

[28] P. C. Wang, Y. C. Liao, Y. L. Lai, Y. C. Lin, C. Y. Su, C. H. Tsai, Y. J. Hsu. *Mater. Chem. Phys*. **2012**, *134*, 325-332.

[29] K. S. Mistry, B. A. Larsen, J. D. Bergeson, T. M. Barnes, G. Teeter, C. Engtrakul, J. L. Blackburn. *ACS Nano* **2011**, *5*, 3714–3723.

Chapter 5

Electrochemical analysis of iodide ions on the SWCNT thin films

5.1. Introduction

Since their discovery, single-walled carbon nanotubes (SWCNTs) have attracted great interest both of fundamental and application fields because of their novel structural, mechanical and electronic properties. It has been reported that electronic properties of SWCNTs can be modified by intercalation using donor or acceptor molecules involving charge transfer interaction. For example, encapsulation of electron acceptor dopants such as iodine compounds (KI, polyiodine and I_2) into SWCNTs was intensively affected the conjugated π-electron system of SWCNTs [1, 2]. Recently, researchers attempt to employ SWCNTs as the electrode materials of electrochemical sensors and dye-sensitized solar cells (DSCs) [3-6]. The subtle electronic properties confirmed that SWCNTs have the ability to promote charge transfer reactions when used as an electrode in electrochemical reactions.

The aim of this work is to explore the effect of tri-iodide ions (I_3^-) on the Single-Walled Carbon Nanotube (SWCNTs) coated Polyethylene Terephthalate (PET) thin-films using electrochemical method.

5.2. Experimental

5.2.1. SWCNTs Thin Films Preparation

HiPco-SWCNTs (Carbon Nano-technologies, Inc.) with an Fe impurity of 9.9 wt.% were used in this study with further purification, and Super-growth SWCNTs were synthesized by a chemical vapor deposition (CVD) process (Center of Advanced Carbon Materials, AIST) were used without further purification because of their high

carbon purity (higher than 99.98 %) [7]. SWCNTs samples of 1.0 mg were dispersed in 50 ml 1, 2-dichloroethane (DCE) with ultra-sonication for 3 days by ultrasonic cleaner. Then, the SWCNTs dispersions were spray-coated onto the PET films (figure 5-1) with various volumes (10 ml, 15 ml, 20 ml) to form SWCNT-PET thin-films (actual size: 5.0 cm × 0.7 cm). The obtained SWCNT-PET thin-films were dried at 100 ^{o}C under vacuum for 12h to remove the DCE. The electric contact of SWCNT-PET thin-film was made by attaching a thin copper wire on one side of the SWCNT-PET thin-film with silver epoxy. The Hipco-SWCNT coated PET named Hipco-PET, and the super-growth SWCNT coated PET named SG-PET.

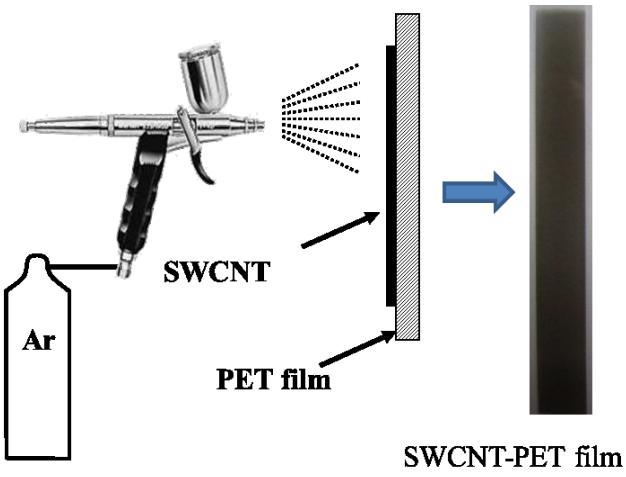

Figure 5-1. The image of spray-coated process and the SWCNT coated PET films denoted as SWCNT-PET films.

5.2.2. Characterization

All of the electrochemical measurements including cyclic voltammetry (CV) and alternating current (AC) impedance are performed in a one-compartment cell containing the SWCNT-PET thin-film as a working electrode, a Pt sheet as a counter electrode and a saturated Ag/AgCl as a reference electrode. Cyclic voltammetry is performed in NaCl-KI working electrolytes (0.1 mol L^{-1} NaCl + 5 mmol L^{-1} KI aqueous solution) with SWCNT-PET thin-film electrode at various scan rates. Charge transfer resistance of this cell was measured by electrochemical impedance

spectroscopy. The light transmittance of all films and the optical absorption spectra of SWCNT-PET thin-films before and after electrochemical measurements were measured using UV-vis-NIR spectroscopy (JASCO V-600). The electronic state change of SWCNTs before and after electrochemical measurements was examined with Raman spectroscopy (JASCO NRS-3100).

5.3. Results and Discussion

5.3.1. Iodide Ions on the Hipco-SWCNT Thin Films

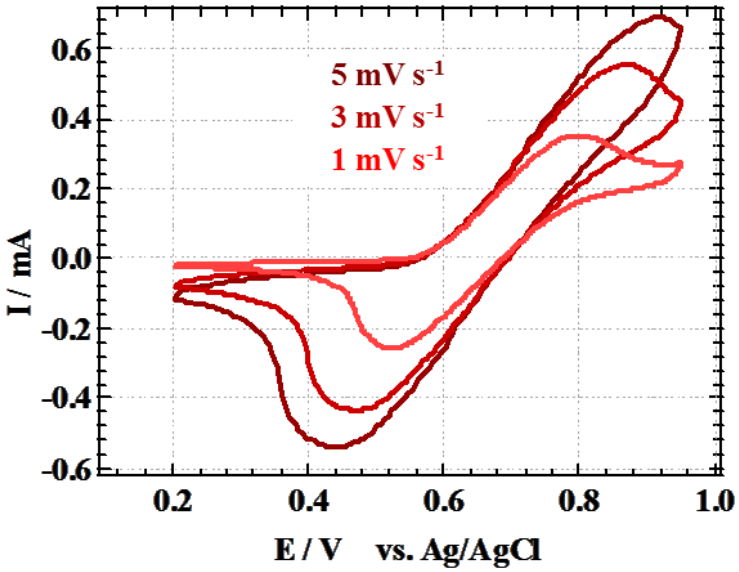

Figure 5-2. Cyclic voltammetry (CV) obtained for Hipco-PET electrode (T=13.56%) in 0.1 mol L^{-1} NaCl electrolyte solution containing 5 mmol L^{-1} KI at various scan rates (5, 3, and 1mV s^{-1}).

The cyclic voltammetry (CV) was studied at a series of scan rates (5 mV s^{-1}, 3 mV s^{-1} and 1mV s^{-1}) for Hipco-PET film with transmittance equal to 13.56% (at 550 nm). CV shows an anodic peak and a cathodic peak for a redox reaction ($3I^- \leftrightharpoons I_3^- + 2e^-$) in figure 5-2. An almost reversible couple is observed centered at 0.66 V with a peak-to-peak separation of 0.28 V at 1 mV s^{-1}. The peak-to-peak separation increases with increasing scan rate, indicating a quasi-reversible process likely as the result of both the slow electron transfer at the SWCNT surface and the slow diffusion through the

narrow pore.

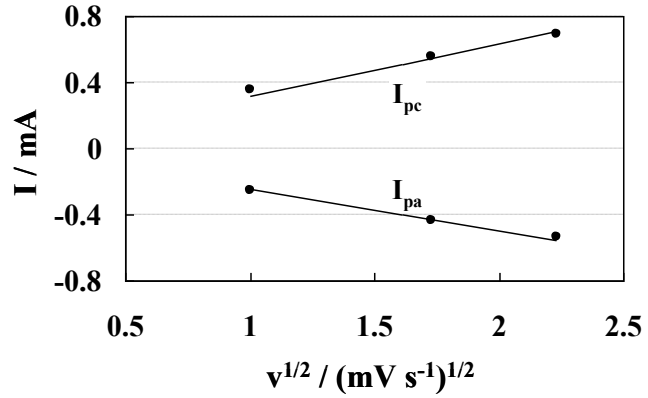

Figure 5-3. Plot for peak currents [cathodic (I_{pc}) and anodic (I_{pa})] vs. square root of scan rates.

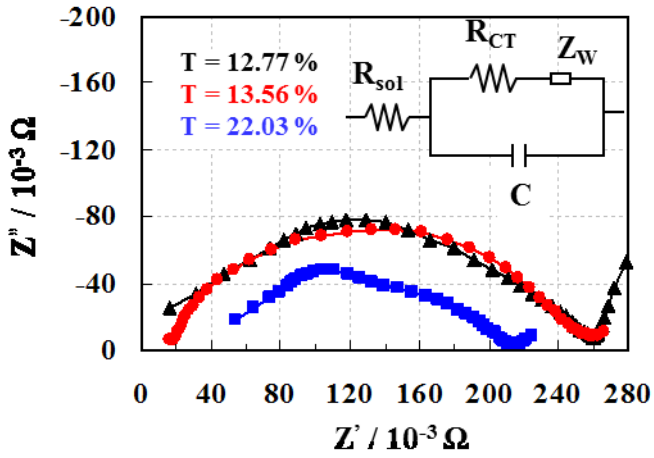

Figure 5-4. Impedance spectra of a cell fabricated with Hipco-PET films working electrodes with various SWCNT loading at a rest potential (+0.70 V). The top inset shows the equivalent circuit.

It is also found that the peak currents increase along with rising of scan rate in figure 5-3. Figure 5-3 shows the relationship of peak currents and scan rates. It may be seen that both the anodic and cathodic peak currents show a linear dependence with the square root of scan rates and passed almost through the origin. Such behavior appears in a quiescent solution in case of diffusion of an ionic species in the vicinity of the electrode surface, which defines the rate of the reaction. Nyquist plots of this

three-electrode cell with various SWCNT loading for Hipco-PET film are show in figure 5-4. The inset shows the equivalent circuit used to model this system, including the solution resistance R_{sol}, charge transfer resistance at the SWCNT/electrolyte interface R_{CT}, double layer capacitance C, and Warburg impedance for tri-iodide ions diffusion. We observed that R_{CT} increases: 0.16, 0.24, and 0.25 Ω cm^2, whereas R_s decreases: 0.040, 0.020, 0.015 Ω cm^2 with increasing SWCNT loading and decreasing light transmittance of 22.03, 13.56, 12.77 %, respectively. This difference is due to the increase in surface area of the Hipco-PET films with higher SWCNT loading.

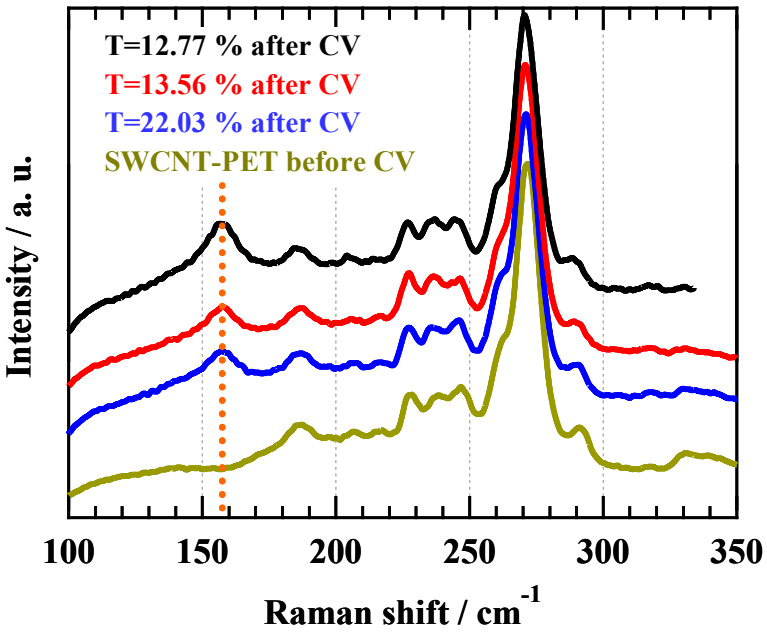

Figure 5-5. Raman spectra of Hipco-PET film at the radial breathing mode (RBM) region measured before and after CV measurement.

Figure 5-5 shows the Raman spectra of SWCNT-PET film at the radial breathing mode (RBM) before and after cyclic voltammetry (CV) measurement. A new peak appears at around 158 cm^{-1} for all Hipco-PET films after CV compare with the film before CV measurement. This indicates that the tri-iodide ions (I_3^-) (which were produced in oxidation reaction $3I^- \rightarrow I_3^- + 2e^-$) were adsorbed onto SWCNTs surface, and the charge transfer interaction occurs between I_3^- and SWCNTs. At a further study, we used another kind of SWCNTs (super-growth SWCNT) with larger

diameter (average diameter: 2.8 nm) and higher purity (> 99.98 %). As a result, the adsorption of I_3^- caused a significantly higher frequency shift from 184 cm^{-1}, and the peak at 138 cm^{-1} disappeared completely. Thus, charge transfer interaction between I_3^- and SWCNTs is evidenced.

5.3.2. Iodide Ions on the SG-SWCNT Thin Films

For iodide ions on the SG-SWCNT thin films, CV was carried out with different thickness of SWCNTs as denoted by transmittance measurement in same condition as previous CV analysis. When increase the thickness of SWCNT film (decrease of the transmittance), the conductivity of the electrode would be expected increase. As the yellow line shown in the figure 5-6, the current increase much quicker when applied potential compared to the thinner film as blue and red plots. In case of different scan rate as shown in the figure 5-6 left and right panels, when we using slow scan rate as $1mVs^{-1}$, the double layer could be formed quick enough to remedy the oxidation of I^-. Therefore, within three scans, the current did not change. When we using quick scan rate as $10mVs^{-1}$, I^- layers are reduced quickly and the double layers would be exhaust without remedy. Therefore, as shown in figure 5-6 right panels, a current decreasing reviewed among different scan.

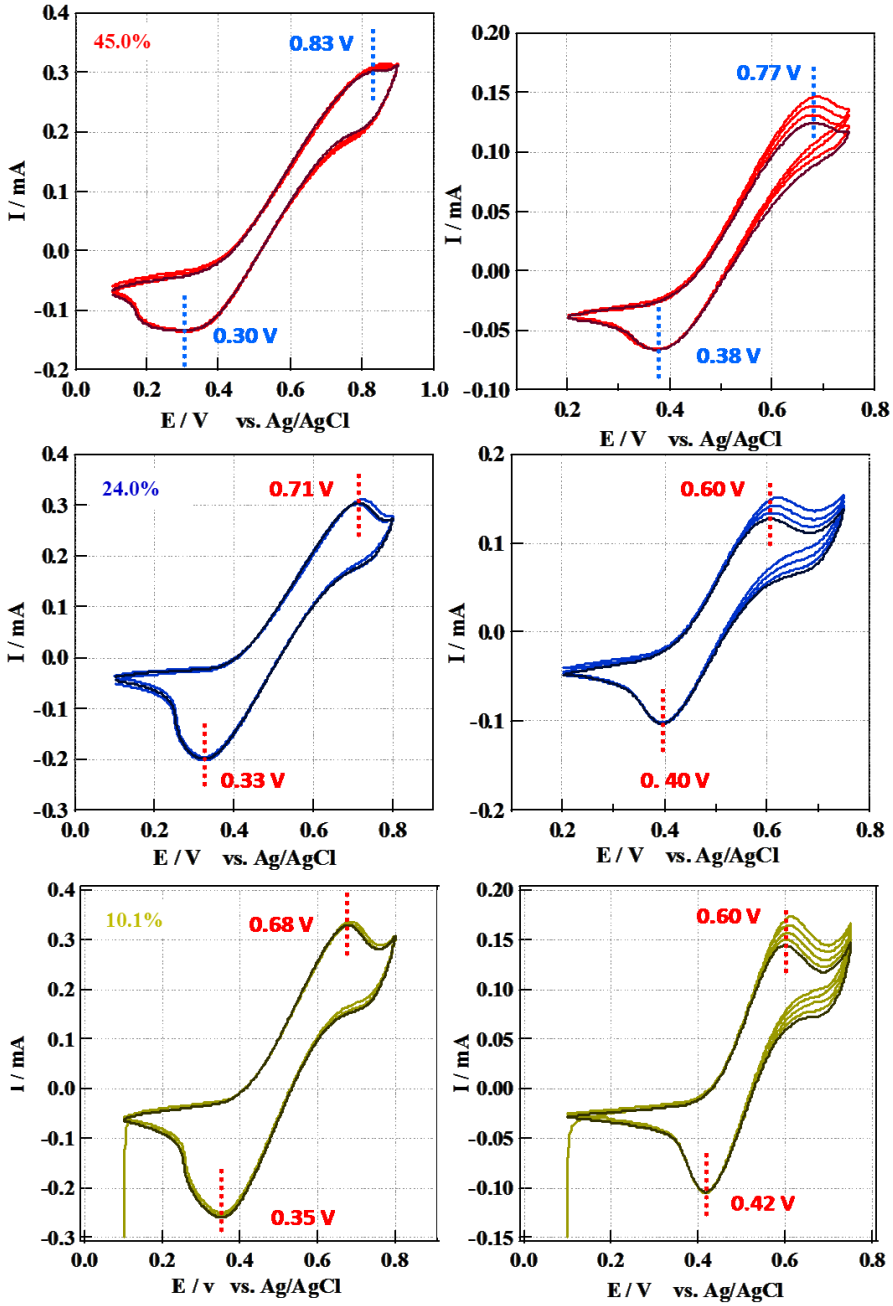

Figure 5-6. Cyclic voltammetry (CV) obtained for SG-PET electrodes with transmittance (at 550 nm) of 10.1% (yellow line), 24.0% (blue line), and 45.0% (red line) in 0.1 mol L^{-1} NaCl electrolyte solution containing 5 mmol L^{-1} KI at different scan rates: 1mV s^{-1} for left spectra, and 10 mV min^{-1} for right spectra.

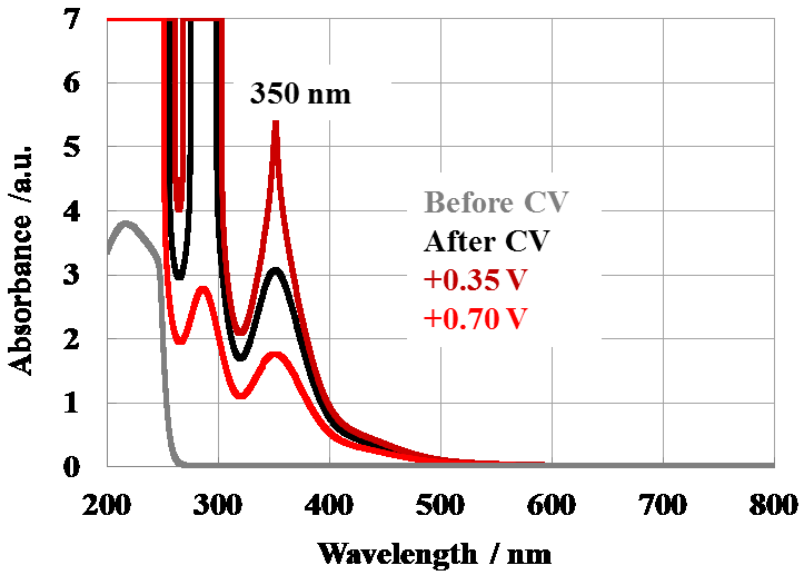

Figure 5-7. UV-Vis spectra for electrolyte (0.1 M NaCl + 5 mM KI aqueous solution) measured before and after cyclic voltammetry (CV) measurement.

UV-Vis spectra of electrolyte solution measured before and after cyclic voltammetry (CV) measurement, and at the rest potential (+0.35 V and +0.70 V) shown as figure 5-7. Compare with the other spectra, no absorption peaks can be observed in the spectrum before CV, indicating the peaks at 285 nm and 350 nm belong to the tri-iodide ions (I_3^-). The spectrum measured at +0.35 V shows highest peak intensity because of the production of I_3^- in oxidation reaction $3I^- \rightarrow I_3^- + 2e^-$. Otherwise, the peak intensity of the one measured at +0.70 V is smaller than the one after one redox reaction, owing to the reduction of the tri-iodide ions (I_3^-).

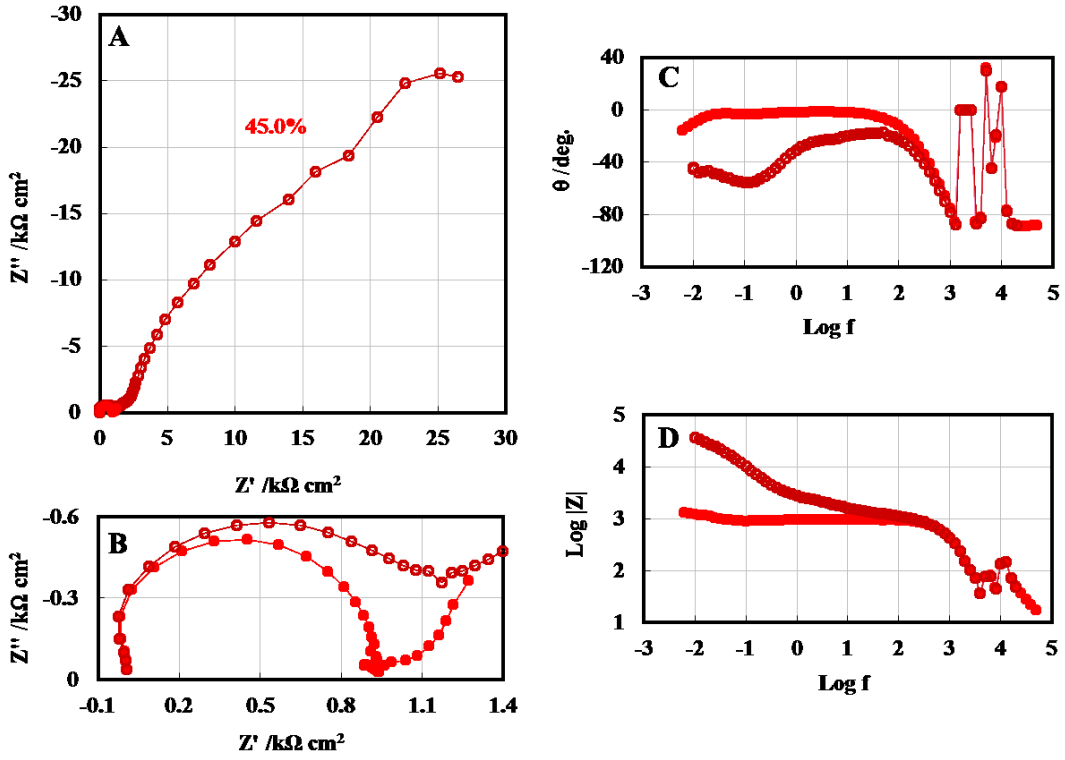

Figure 5-8. Impedance spectra of a cell fabricated with SG-PET film working electrode measured at +0.70 V (red line) and +0.35 V (deep red line) (A), the expanded spectra (B), Bode phase plots (C&D)

The charge transfer resistance (R_{CT}) of an electrochemical reaction can be easily determined from the intercept of the semicircle in a Nyquist plot with the real axis ($-Z^{II} = 0$). As shown in Figure 5-8B, the R_{CT} of red line (0.7V) is smaller than R_{CT} of deep red line. Since when applied 0.7V (vs. Ag/AgCl) potential to the working electrode, the energy level of electron in SWCNTs are decreased which closed to the redox potential of I^-/I_3^-, therefore, the electrons would inject to the working electrode from solution which also means the charge transfer resistance decrease. If we applied 0.35V to the working electrode, the electron energy different between working electrode and solution is not favorable for charge transfer, there would be a big potential barrier for electron transfer. Therefore, as shown in Figure 5-8, the deep red line which attributed to the 0.35V applied bias have bigger R_{CT} than the 0.7V one.

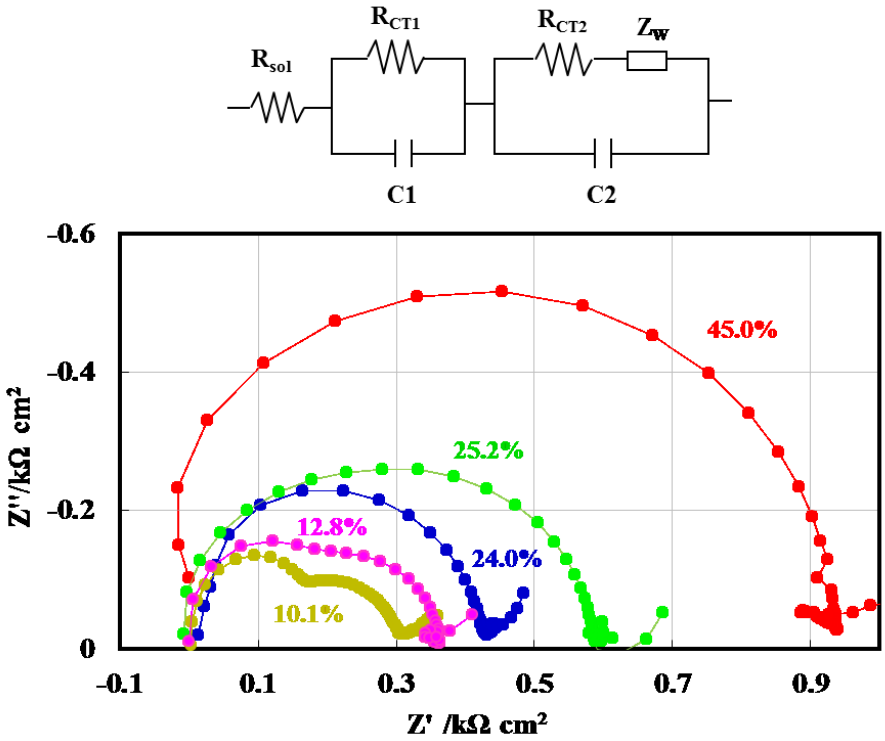

Figure 5-9. Impedance spectra of a cell fabricated with SG-PET films working electrodes with various SWCNT loading at a rest potential (+0.70 V). The equivalent circuit is shown on the top of the spectra.

When we applied same potential (0.7V) to the working electrode as shown in Figure 5-9, the charge transfer would be mainly depend on the conductivity of the electrode. Therefore, as we expected, the more SWCNTs loaded (yellow line), the smaller R_{CT} achieved.

A plausible equivalent circuit was also provided as shown on the top of Figure 5-9. Thereby, the R_{CT1} would be denoted as the conductivity of SWCNTs films and R_{CT2} would be attributed to the charge transfer barrier between electrode and solution interface which we explained as the electron energy levels between working electrode and redox potential of solution.

However, when we applied same potential (0.35V) to the working electrode as shown in Figure 5-9, the charge transfer would be depend on R_{CT1} and R_{CT2} which make the understanding more complicated. Since both resistance would play a role when the electron transfer between electrode and solution.

As shown in Figure 5-10B, the green and red line shows reasonable trend that the R_{CT1} decrease as the increasing of the thickness of SWCNTs films. But the other two lines are not very understandable which may be come from the failure measurement.

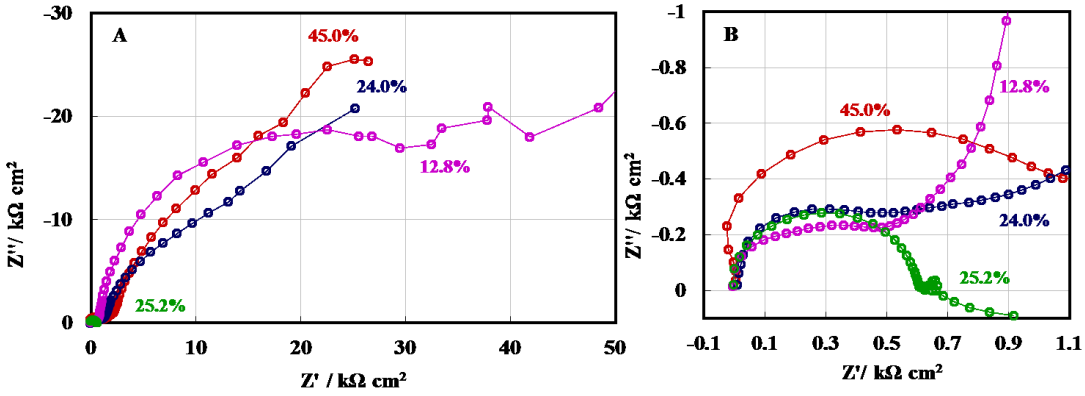

Figure 5-10. Impedance spectra of a cell fabricated with SG-PET films working electrodes with various SWCNT loading at a rest potential (+0.35 V) (A), and the expanded spectra (B).

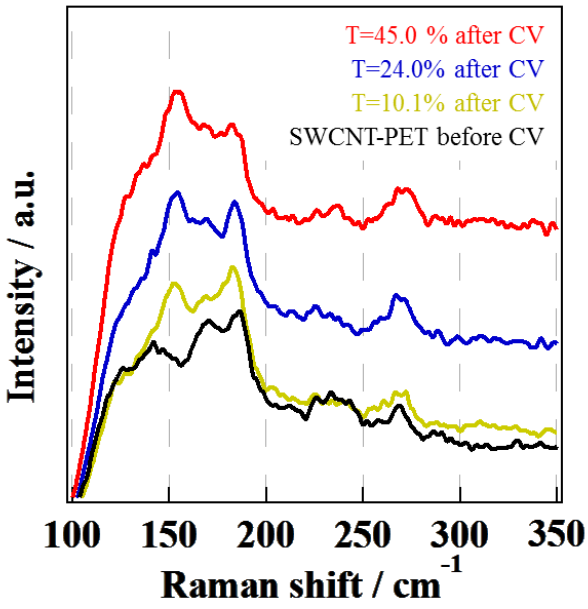

Figure 5-13. Raman spectra of SG-PET film at the radial breathing mode (RBM) region measured before and after CV measurement.

In Raman spectra, a new peak appears at 154 cm^{-1} for all SG-PET electrodes after

CV measurement, indicating the tri-iodide ions (I_3^-) (which were produced by oxidation reaction $3I^- \rightarrow I_3^- + 2e^-$) were adsorbed onto the SWCNT electrode surface, and the peak at 186 cm^{-1} shifts to a lower frequency side by 3 cm^{-1} prove that electronic structure of SWCNT changed because of the charge transfer interaction between I_3^- and SWCNT.

5.4. Conclusions

In conclusion, we have successfully realized the application of spray coated SWCNT on PET substrate as working electrode for tri-iodide ion (I_3^-) reduction. The charge transfer resistance of SWCNT-PET electrode in iodide/tri-iodide (I^-/I_3^-) redox couple electrolyte can be controlled by changing SWCNTs loading. Tri-iodide ions can be adsorbed onto the SWCNTs by electrochemical method. The electronic structure of SWCNT can be modified systematically through charge transfer interaction. By doing systematic electrochemistry measurement, the redox potential of I^-/I_3^- was found to be around 0.7V (vs. Ag/AgCl) and preliminary impedance spectroscopy measurement also carried out in order to understand the charge transfer properities between SWCNts working electrode and KI solution.

References

[1] N. Minami, S. Kazaoui, R. Jacquemin, H. Yamawaki, K. Aoki, H. Kataura, Y. Achiba, *Synthetic Metals* **2001***, 116*, 405.

[2] C. Hayakawa, K. Urita, T. Ohba, H. Kanoh, K. Kaneko, *Langmuir **2009**,* 25, 1795.

[3] T. N. Murakami, M. Gratzel, *Inorganica Chimica Acta* **2008***, 361*, 572.

[4] S. Kim, J. Yim, X. Wang, D. C. Bradley, *Adv. Funct. Mater.* **2010***, 20*, 2310.

[5] C. Y. Su, A. Y. Lu, Y. L. Chen, C. Y. Wei, P. C. Wang, C. H. Tsai, *J. Mater. Chem.* **2010***, 20*, 7034.

[6] M. M. Rahman, I. C. Jeon, *J. Braz. Chem. Soc.* **2007***, 18*, 1150.

[7] K. Hata, D. N. Futaba, K. Mizuno, T. Namai, M. Yumura, S. Iijima, *Science* **2004***, 306*, 1362.

Chapter 6

Nanodynamic Analysis of Ionic Liquids Confined in Carbon Nanospace using an NMR Method

In this chapter, we report pulsed-field gradient-nuclear magnetic resonance (PFG-NMR) results of the structural and dynamical properties of the bulk ionic liquids (ILs) ([EMIm][BF_4], [BMIm][BF_4], [BMIm][PF_6], [HMIm][BF_4], [HMIm][PF_6]) and ILs [EMIm][BF_4] confined inside activated carbon fiber (ACF) with inner diameters of 1.1 nm for A20 and 1.0 nm for A15. The main objective of this study was to understand effects of the pore size and the pore filling on the structural and dynamical properties of the confined ILs. The rest of this chapter is structured as follows. Section 6.1 is the introduction. Section 6.2 contains a description of the properties of materials have been employed in this study and our experimental methods. In order to well understand the diffusion behavior of the ILs confined inside nanopores, we need to study the dynamic properties of bulk ILs as a reference. So, this section concludes two components: bulk ILs and confined ILs. In Section 6.3 we present results and discussions of the structural and dynamic properties of the bulk ILs and confined ILs separately as well as section 6.2, and in Section 6.4 we summarize our main findings.

6.1. Introduction

As an attractive technology for electric energy storage, supercapacitors have attracted great interest recently [1-8]. Also called electrical double-layer capacitors (EDLC) or ultracapacitors, supercapacitors store energy by forming electric double layers of the electrolyte within two symmetric porous carbon electrodes of high

surface area and opposite charges. The recent discovery of the normalized capacitance increase in carbide-derived carbon (CDC) microporous structures at the pore size is smaller than 1 nm [9, 10], has given rise to a great deal of technological activity to refine potential devices [11] and fundamental research to uncover the underlying molecular phenomena [12-15].

Nanopores have a great potential for use in drug delivery, nano-fluidic transistors, DNA translocation, catalysis, sensors for chemical agents, nanobatteries, supercapacitors, templates for nanoparticle self-assembly as well as in fundamental research [16-20]. These applications require in-depth understanding of the motion of molecules or charge carriers inside the pores. On the other hand, molecular diffusion in a unidimensional channel is very different from that of isotropic diffusion in the bulk system. For example, the melting points and the thermal decomposition temperature of several ILs have been reported to increase by more than 200 °C when confined inside multi-walled carbon nanotubes (MWCNTs) [21, 22]. In contrast, when confined inside nanoporous silica [23], ILs can exhibit similar mobility as the bulk phases, and their melting points decrease significantly [24, 25]. Therefore, diffusion in nanopores very interesting and it is very important to study in-depth.

6.2. Experimental:

6.2.1. Preparation of Bulk ILs Samples

ILs containing three different types of methylimidazolium-based cations (1-ethyl-, 1-butyl- and 1-hexyl-3-methylimidazolium; [EMIm], [BMIm] and [HMIm]) and two types of anions (tetrafluoroborate [BF_4] and hexafluorophosphate [PF_6]) were used without further treatment. All of these ILs were purchased from Fluka except [HMIm][BF_4] (Aldrich). The details about the physical properties of these ILs are shown in table 6-1.

Samples were prepared by adding ILs and deuterated water (D_2O) into the standard 5 mm NMR tubes with a series concentration of ILs (percentage by volume) between 100% and 10%. The total volume of each mixture was 0.8 ml. After loading the

samples, the NMR tubes were sealed by caps to avoid changes in the water content. All diffusion measurements were performed at 298 K after sample equilibration.

Table 6-1. Physical properties of methylimidazolium-based ILs:

	M /g mol^{-1}	T_m /K	T_b /K	T_d /K	ρ /g ml^{-1}	Purity
[EMIm][BF_4]	197.97	288	> 623	664[26]	1.294[a]	≥ 97.0%
[BMIm][BF_4]	226.02	202	561	698[27]	1.21[b]	≥ 97.0%
[BMIm][PF_6]	284.18	283[27]		706[27]	1.38[b]	≥ 98.5%
[HMIm][BF_4]	254.08				1.149[b]	≥ 98.5%
[HMIm][PF_6]	312.04				1.419[b]	≥ 99.0%

[a] The density at 25 ^{o}C. [b] The density at 20 ^{o}C.

Proton pulse-field gradient nuclear magnetic resonance (PFG-NMR) diffusion studies were carried out at 298 K on a Bruker DSX-400 MHz spectroscopy with a Diff 30 field gradient probe. Diffusion data were obtained from dependencies of the intensity of the PFG NMR signal (A) on the amplitude of the magnetic field gradients (g). The signal intensity was determined by integrating the area under selected line(s) of the frequency-domain NMR spectra recorded by the PFG NMR stimulated echo pulse sequence. Different lines in such spectra can correspond to different species. Hence, diffusion data for a chosen type of species in a sample can be obtained by selecting an appropriate line in the spectrum for data processing. For the NMR lines exhibiting no significant overlap with the lines of other types of ions or molecules in a sample the diffusivity (D) was determined from the measured attenuation of the PFG NMR signal ($\Psi \equiv A_{(g)}/A_{(g=0)}$) corresponding to this line using [28, 29] :

$$\Psi = exp\left((-\gamma\delta g)^2 D\left(\Delta - {}^{\delta}/_{3}\right)\right) \tag{6-1}$$

where γ is the gyromagnetic ratio of the nuclei, which is 2.675 × 10^8 rad T^{-1} s^{-1} for a proton; δ denotes the effective duration for rectangular gradient pulses; g is the amplitude of the magnetic gradients; and Δ is the separation between the gradient pulses.

lnΨ versus $[(-\gamma\delta g)^2(\Delta-\delta/3)]$ can be plotted to give a straight line with a gradient of D. If the plot shows two distinct slopes, then the data is analyzed with two different diffusion coefficients.

The hydrodynamic radii (R_h) can then be obtained from the Stokes-Einstein equation (eq. 6-2), assuming that the aggregates are spherical and non-interacting.

$$R_h = {}^{k_B T}/_{6\pi\eta D} \tag{6-2}$$

where k_B is the Boltzmann constant, T is the absolute temperature, and η is the viscosity of the solvent mixture.

Viscosity of the ILs was measured with a viscometer (m-VPOC) at 298 K.

6.2.2. Preparation of Confined ILs Samples

Pitch-based activated carbon fibers (ACF-A20, -A15, AD'ALL Co. Ltd.) were used in an agate mortar. Pore structures were characterized based on the N_2 adsorption isotherm at 77 K. Details of those analyses are shown in table 6-2. The SEM images of ACF-A20 are shown in figure 6-1.

Table 6-2. Physical properties of ACF:

	A20	A15
S_{BET} ($P/P_0 = 0.05 \sim 0.30$) /$m^2\ g^{-1}$	1740	1430
$S(\alpha_s)$ /$m^2\ g^{-1}$	1750	1400
Slit pore with (α_s) /nm	1.1	1.0
Micropore volume (DR) /ml g^{-1}	0.63	
Total pore volume (α_s) / ml g^{-1}	0.97	0.67

250 mg of grinded ACF samples were evacuated at 393 K for 2 h using a vacuum line, and then mixed with 150 μl and 100μl ILs [EMIm][BF_4] for A20, 90μl for A15, respectively. The mixtures were sealed into glass tubes under vacuum, then were heated up to 600 K and keep it for 12 h in an electric-furnace as shown in scheme 6-1.

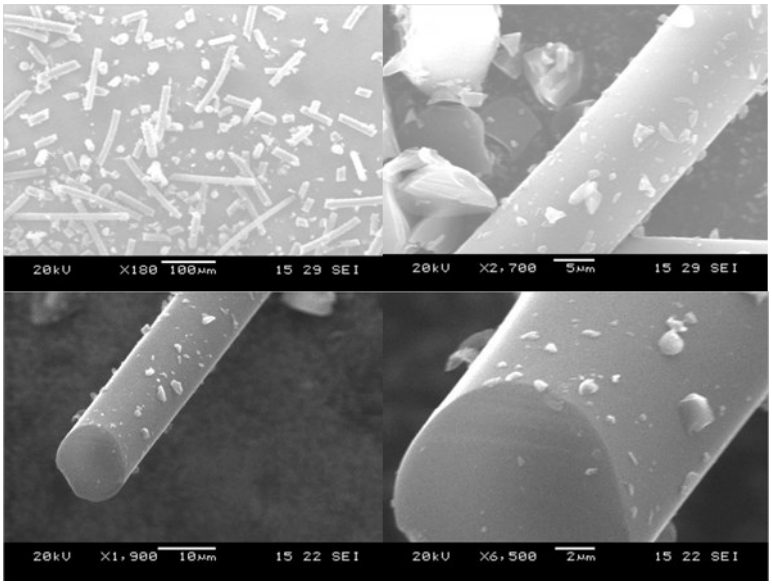

Figure 6-1. SEM images of ACF-A20.

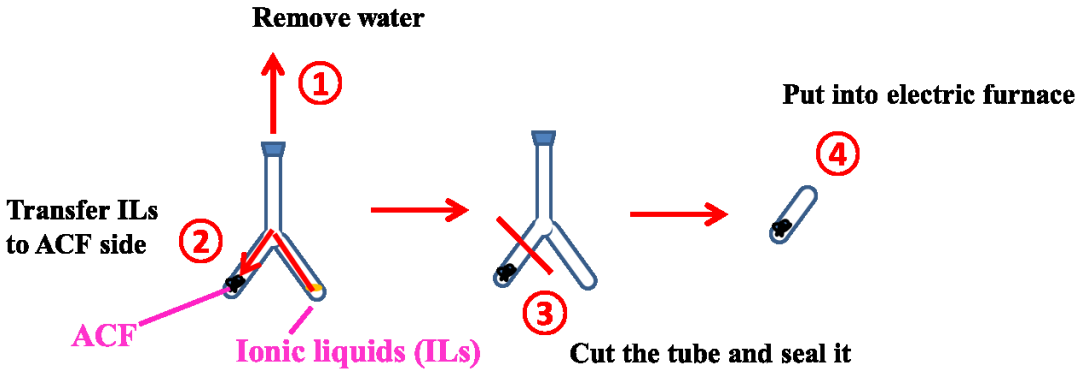

Schem 6-1. The method of samples preparation

Activated carbon fiber (ACF) 250 mg

1) Drying ACF under vacuum (<1×10^{-4} mbar) at 393 K for 2 h (remove the water in the ACF nanopores).
2) Transfer the ILs to the ACF side.
3) Cut and seal the tube.
4) Put the tube into an electric-furnace, heating the samples up to 600 K for 12 h.
5) Transfer the sample into an NMR tube in ambient.

ILs- ACF

Thermo-gravimetric analysis (TGA) was performed on a thermo-gravimetric analyzer (Shimadzu; DTG-60AH) at a heating rate of 5 K min^{-1} and N_2 flow rate of 100 cm^3 min^{-1} to determine the adsorbed amounts of ILs inside the ACF. Proton PFG-NMR diffusion studies were carried out at 298 K on a Bruker DSX-400 MHz spectroscopy.

6.3. Results and Discussions

6.3.1. Bulk Ionic Liquids

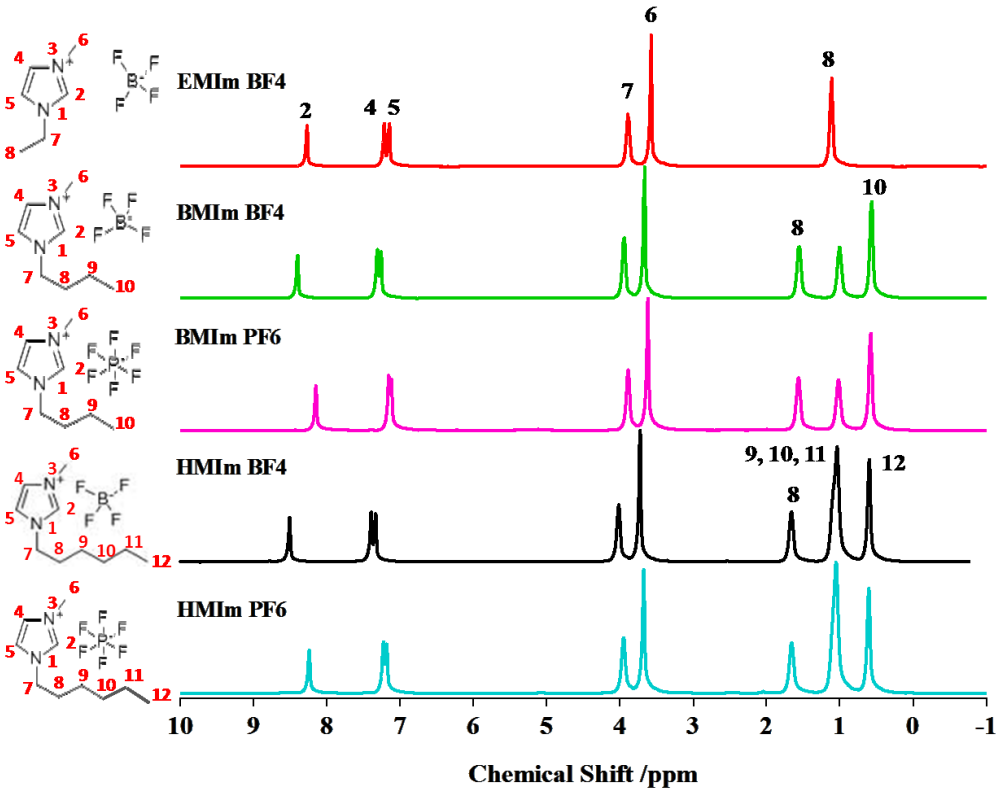

Figure 6-2. ^{1}H NMR spectra of imidazolium based ionic liquids at 298 K.

Figure 6-2 shows the ^{1}H 1D-NMR spectra of bulk pure [EMIm][BF_4], [BMIm][BF_4], [BMIm][PF_6], [HMIm][BF_4], and [HMIm][PF_6]. The numbers (1 ~ 8) in figure 6-2 correspond to the skeleton atoms for the cation in the inset of figure 6-2. In these spectra, all peaks are assigned to the cations because there is no proton existence in the anions. The peaks at the low frequency region around 0 ~ 3.8 ppm are

originate from the protons of the ethyl chain for $[EMIm]^+$, butyl chain for $[BMIm]^+$, and hexyl chain for $[HMIm]^+$, while the peak around 4.0 ppm belongs to the protons of the methyl group attached to the imidazolium ring. The peaks at downfield 7 ~ 9 ppm can be assigned to the protons of the imidazolium ring. There is no water signal appears in these spectra. This is because the ionic liquids we used in this study is high purity with the water percentage is low than 0.05 %. It is seen in figure 6-2 that the chemical shift of the protons on the imidazolium ring (H2, H4, H5) show a significantly downfield shift with increasing length of the alkyl chain for the same anion, and upfield shift with increasing the size of the anion (as shown in table 6-3). However, there are no significantly shifts were observed for the peaks attributed to the alkyl chain, indicates the protons on the imidazolium ring interacts more closely with the anions. We also observed that the shift of H2 is obviously larger than H4 and H5, indicates H2 interacts more strongly than H4 and H5.

Table 6-3. Chemical shifts of respective protons in cations.

ppm	2	4	5	7	6	8	9～11	12
$EMImBF_4$	8.28	7.21	7.15	3.90	3.58	1.12		
$BMImBF_4$	8.39	7.31	7.25	3.94	3.66	1.55	1.00	0.55
$BMImPF_6$	8.16	7.15	7.11	3.88	3.62	1.55	1.01	0.56
$HMImBF_4$	8.51	7.40	7.33	4.00	3.73	1.66	1.02	0.58
$HMImPF_6$	8.24	7.23	7.18	3.95	3.68	1.64	1.06	0.61

It has been confirmed that various properties of ILs such as intensity, polarity, solubility, viscosity and conductivity depend on the water content [30-32]. Therefore, a detailed understanding of the dynamic behavior of ILs-water mixtures is important. In this study we use deuterated water (D_2O) replaced H_2O to avoid the intensity effect on the proton NMR spectrum, and we expect the D_2O effect might be different. The ^1H NMR spectra of $[EMIm][BF_4]$ and $[BMIm][BF_4]$ in D_2O are shown in figure 6-3. Compare with the pure ILs (figure 6-3a), when a small amount of D_2O is added into

ILs (figure 6-3b), the chemical shift of cation peaks were observed to shift downfield. All singles are located at the downfield compared to the pure ILs even increase the water concentration up to 90%. As we all known, the formation of hydrogen bond makes the proton signal shift downfield. This result suggests that an addition of D_2O into ILs increases the number of hydrogen bond owing to the formation of new hydrogen bond between water and cation or inion, results in perceptible deshielding effect on all protons in the cations. This factor should be lead to a downfield shift for those protons.

On the other hand, the chemical shifts of all proton signals due to the cations shift upfield with increasing water concentration (figure 6-3 b-g). When a small amount of water was added to ILs, the hydrogen bond interaction cation-water and anion-water are formed results in downfield shift for all protons in cations. However, with the further addition of water, the cation separated from the anion and was surrounded by water molecules. At the same time, water prefers to form hydrogen bond with water rather than cation. Therefore, such changes in the chemical shift can be attributed to a decrease in the extent of hydrogen bond between water and cations with increasing water concentration (or decreasing ILs concentration) [33].

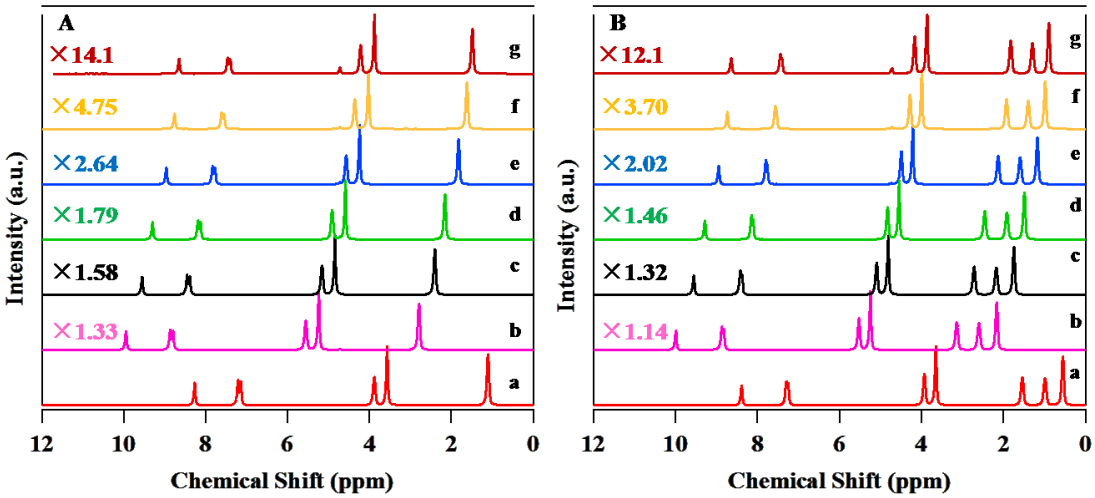

Figure 6-3. ^{1}H NMR spectra of [EMIm][BF_4] (A) and [BMIm][BF_4] (B) in D_2O with varies ILs concentration (percentage by volume) at 298 K: (a) 100%, (b) 90%, (c) 80%, (d)70%, (e) 50%, (f) 30%, and (g) 10%.

The PFG-NMR method is noninvasive and makes it possible to independently measure the self-diffusion coefficient of each ionic species in the system under the study, provided that the components contain NMR sensitive nuclei [34]. Figure 6-4 shows the ^{1}H PFG-NMR attenuation curves of 3-methylimidazolium based ionic liquids (ILs) with Δ was fixed at 500 ms and δ was 2 ms. The lines marked as circle are raw data, while the solid lines are the fitting data. Each set of the result shows good linear relationship, and the self-diffusion coefficient can be obtained from the slope of each set of plots and equation 6-1.

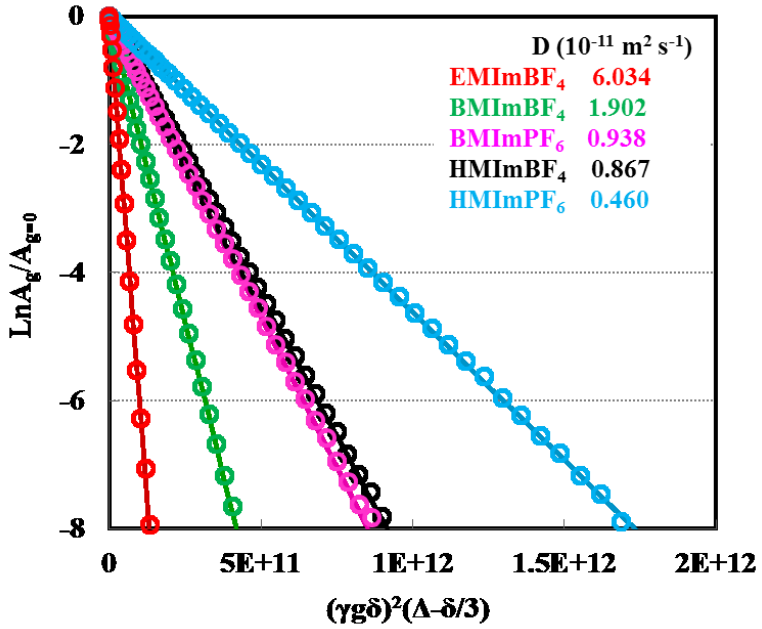

Figure 6-4. ^{1}H PFG-NMR attenuation curves of pure imidazolium based ionic liquids at 298 K.

The relationship between diffusion coefficient (D) and molecular mass is shown in figure 6-5. It is seen that the diffusion coefficient of bulk ILs decreases with increasing the molecular mass for the same anion ($D_{[EMIm]+} > D_{[BMIm]+} > D_{[HMIm]+}$). That is because the $[EMIm]^+$ cation is smaller and is expected to diffuse more quickly through the liquid than the larger $[HMIm]^+$ cation with its long alkyl chain which should restrict its mobility and reduce free space among the ions.

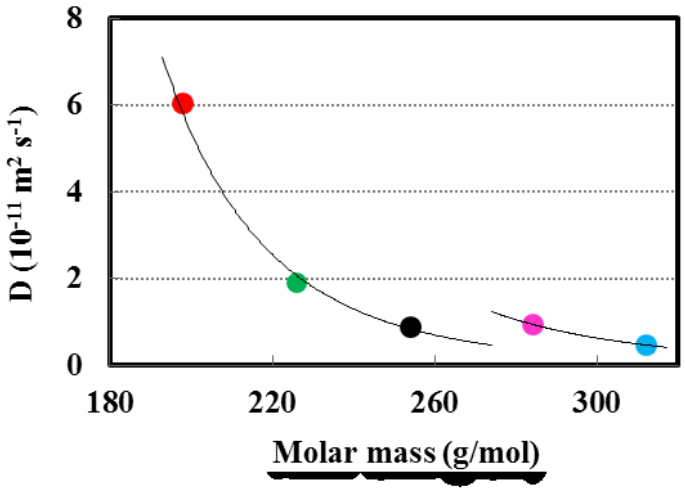

Figure 6-5. The diffusion coefficients of imidazolium based ionic liquids for [EMIm][BF_4] (red), [BMIm][BF_4] (green), [HMIm][BF_4] (black), [BMIm][PF_6] (pink), and [HMIm][PF_6] (blue). The relationship can be clearly shown from the fitting data (solid lines).

Figure 6-6 shows examples of the PFG-NMR attenuation curves measured for ILs [EMIm][BF_4], [BMIm][BF_4], and [HMIm][BF_4] in D_2O. All of the samples have a same anion $[BF_4]^-$, and all attenuation curves were fitted to a single diffusion coefficient. The linearly attenuation curves meaning that the ILs is either all solubilized or is in fast exchange between the aqueous solution. Figure 6-6 also shows that the diffusion coefficient decreases with increasing ILs concentration.

The plots of diffusion coefficient and ILs molar concentration are shown in figure 6-7. It shows a general trend that the dynamics slows down as the concentration increases for all species. This may be ascribed to the increasing of the viscosity with increasing concentration. A similarly result was reported by Nakakoshi et al. for the dynamic study of [BMIm][Br] [35]. In this paper, they assume that [BMIm] cation contains both hydrophobic and hydrophilic moieties. They also suggest that, at higher molar fractions χ_{ILs}>0.015 (about 0.75 M for [BMIm][Br]), the cations and anions are completely dissociated and move independently may be caused by the repulsion from cations and attraction from anions. Therefore, we suggest that the addition of water weaken the hydrogen bonding interaction between cation and anion, results in the

increasing of cation diffusion coefficient in this concentration we studied.

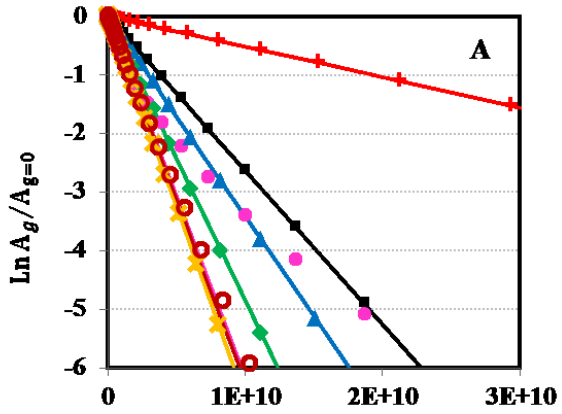

$EMImBF_4$ concentration	D (10^{-10} $m^2 s^{-1}$)
100%	0.5206
90%	2.547
80%	2.634
70%	3.420
50%	4.837
30%	6.558
10%	6.297

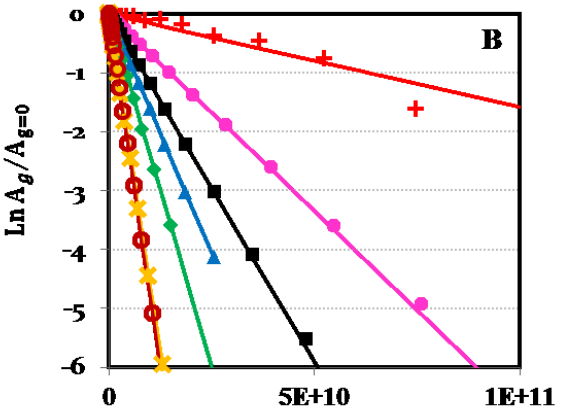

$BMImBF_4$ concentration	D (10^{-10} $m^2 s^{-1}$)
100%	0.1592
90%	0.6763
80%	1.190
70%	1.636
50%	2.395
30%	3.465
10%	4.833

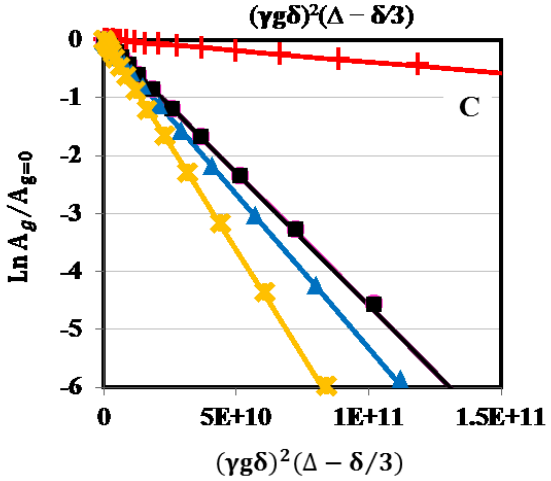

$HMImBF_4$ concentration	D (10^{-10} $m^2 s^{-1}$)
100%	0.03584
97.5%	0.4641
92.3%	0.4646
90%	0.5388
87.5%	0.7366

Figure 6-6. ^{1}H PFG-NMR attenuation curves of the solutions of ILs in D_2O with a range of concentrations (by volume) from 10% to 100% for [EMIm][BF_4] (A) and [BMIm][BF_4] (B), 87% to 100% for [HMIm][BF_4] (C).

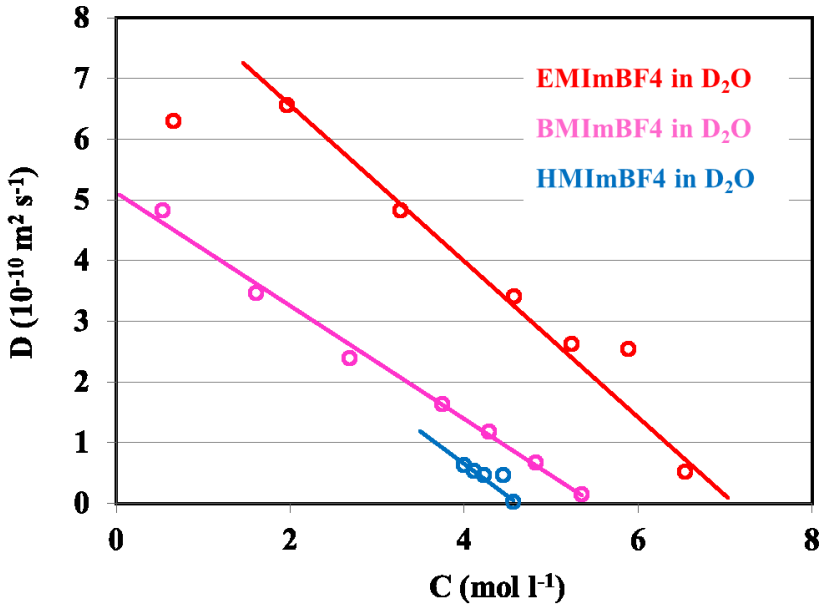

Figure 6-7. Diffusion coefficients of [EMIm][BF_4] (red), [BMIm][BF_4] (pink) and [HMIm][BF_4] (blue) in D_2O as a function of the concentration at 298 K.

Table 6-4. Aggregation data determined using PFG-NMR for pure ILs and the solutions of [EMIm][BF_4] in D_2O at 298 K

solutions	D($\times 10^{-11}$) m^2 s^{-1}	R_h (Å)	η (cP)
Pure [EMIm][BF_4]	5.206	1.1	34.04
70%	34.20	1.7	3.80
50%	48.37	1.8	2.50
30%	65.58	1.8	1.87
10%	62.97	2.8	1.23
Pure [BMIm][BF_4]	1.902	1.1	107.7
Pure [BMIm][PF_6]	0.938	0.9	250.5
Pure [HMIm][BF_4]	0.867	1.3	196.0
Pure [HMIm][PF_6]	0.460	1.0	469.9

Table 6-4 shows the ^1H self-diffusion coefficient values, D, for the cations in ILs, [EMIm][BF_4], [EMIm][BF_4], [EMIm][BF_4], [EMIm][BF_4], and [EMIm][BF_4] as well as the diffusion data arising from dilution of [EMIm][BF_4] in D_2O. The diffusion constant increases with decreasing of viscosity as well as decreasing of ILs concentration for [EMIm][BF_4]/D_2O solutions. So we suggest that D values arise from

the relatively large measured viscosities of these ILs.

6.3.2. Confined Ionic Liquids

In this section, effects of the diffusion time of [EMIm][BF_4], amount of adsorbed [EMIm][BF_4], and pore size of ACF were studied to understand the structural and dynamic properties of ILs confined inside slit-like graphitic pores.

6.3.2.1. Effect of the Diffusion Time of [EMIm][BF_4]

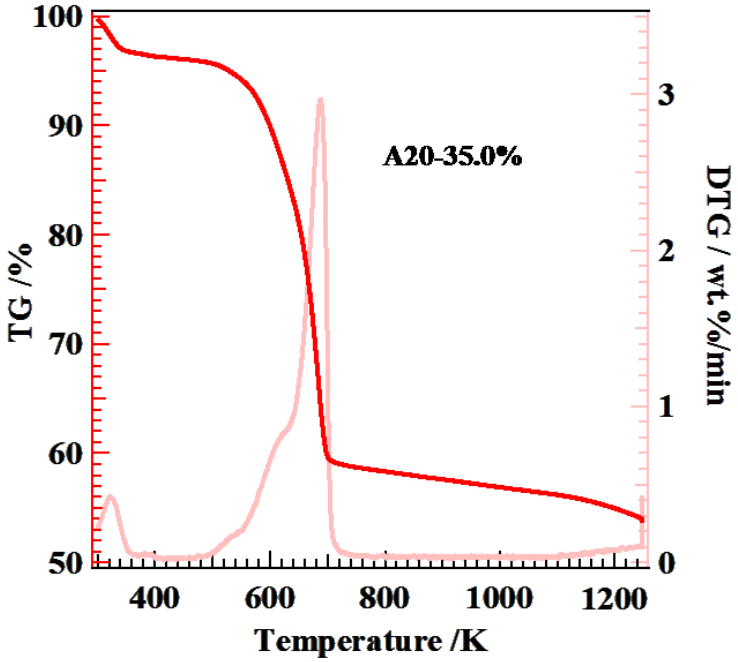

Figure 6-8. TGA thermograms of A20-35.0%

The amount of confined [EMIm][BF_4] was calculated by a thermogravimetric analysis (TGA) measurement. Figure 6-8 shows the TGA results of confined [EMIm][BF_4] inside ACF-A20. It can be seen that there is an initial loss of weight at a temperature below 350 K. This is attributed to the removal of physically adsorbed water. The TGA thermograms shows a main weight loss of [EMIm][BF_4] at around 650 K which very close to the decomposition temperature 664 K [26], indicating the weight loss of this region are from the decomposition of the strongly bonded

[EMIm][BF_4] confined inside ACF, and the shoulder in the range of 450-600 K should be attributed to the removal of weakly bonded or free [EMIm][BF_4] confined inside ACF. The weight loss in the range of 450-800 K is about 35.0%, so we named this sample as A20-35.0%.

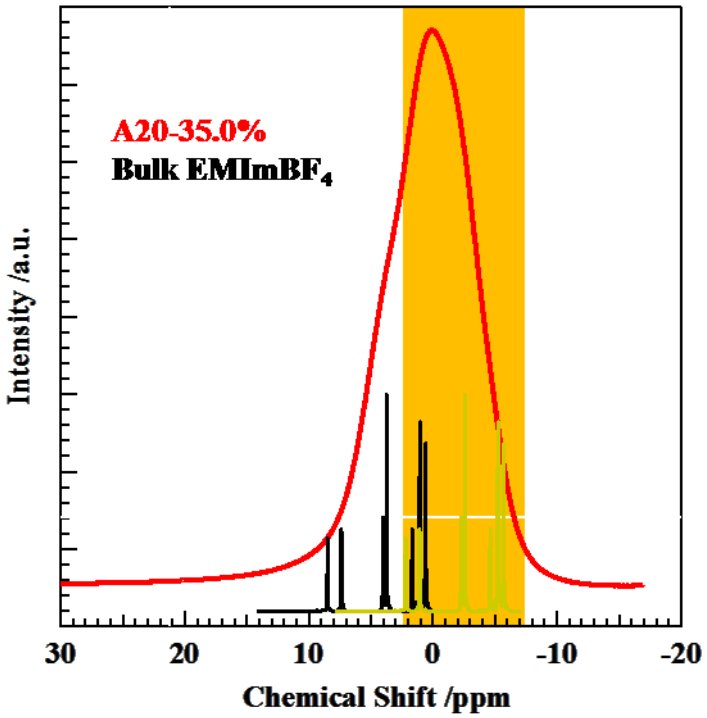

Figure 6-9. ^{1}H NMR spectra of confined [EMIm][BF_4] inside A20 (red line), bulk [EMIm][BF_4] (black line) and shift upfield by 6 ppm (yellow line) at 298 K.

Figure 6-9 shows the ^{1}H NMR spectra of confined [EMIm][BF_4] (A20-35.0%). Compare with the bulk [EMIm][BF_4] (black line), there is only one single peak centered at around 0 ppm caused by the overlapping of all proton signals. The peak of confined [EMIm][BF_4] may be separated to two parts in the range of 10 - 0 ppm and -10 - 0 ppm, respectively. Here we suggest that the left part might be come from the confined water or the free [EMIm][BF_4] molecules, and the right part is attributed to the confined [EMIm][BF_4].

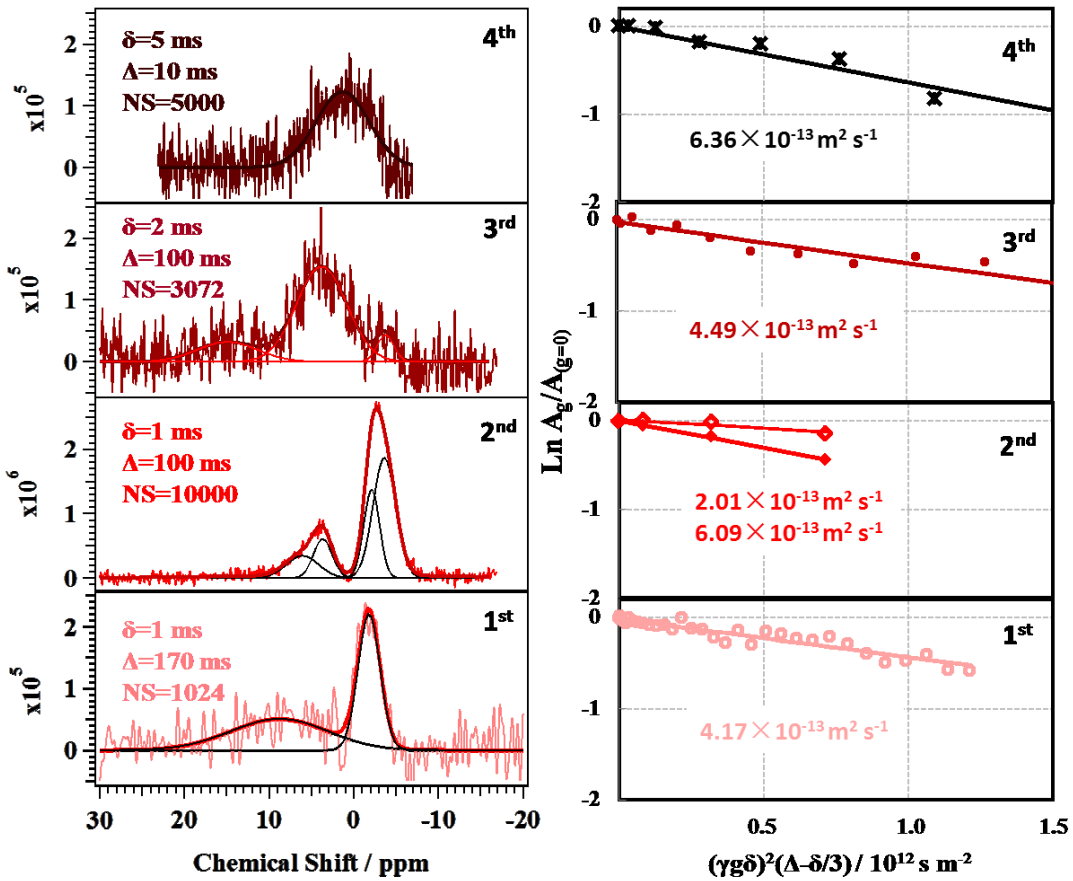

Figure 6-10. ^{1}H NMR spectra of sample A20-35.0% (left side) from the diffusion measurement and the attenuation curves (right side) with varies gradient pulse duration (δ) and diffusion time (Δ).

In this section, we studied the effects of the parameters which can effect on the diffusion coefficients D, such as different gradient pulse duration (δ), diffusion time (Δ). Figure 6-10 (left) shows the ^{1}H NMR spectra of sample A20-35.0% from the 2D diffusion measurement with different parameter settings. The sample was measured four times defined as 1st, 2nd, 3rd, and 4th as show in figure 6-10. The detailed measurement set-ups are given in Table 6-5. The smooth peaks were obtained from multi-peak fitting. From the results as shown, different gradient pulse duration (δ), diffusion time (Δ) and the number of scans (ns) were found have distinguished effect on ^{1}H chemical shift and the signal-to-noise ratio. In the case of δ or Δ, the effects were mainly seen as the changing of position and shape of peaks. We assume δ or Δ effects could be attributed to the different dynamic state of adsorbed ILs molecules in

the nanospace such as adsorbed orientation, adsorbed condition (completed, close or sequestered attached), or pore size; in case of scan times (ns), the main effects are the increase of signal-to-noise. Figure 6-10 right side shows the attenuation curves of A20-35.0% with four times measurements. All results show a single component reflect on the attenuation curve is a linearly decay, indicates all pieces have a similar diffusion velocity measured under a specific diffusion time.

As we discussed in the DTG analysis (figure 6-8), the weight loss in the range of 450-600 K reflects to the free or weakly bonded [EMIm][BF_4], and the weight loss in the range of 600-800 K reflects to the strongly bonded [EMIm][BF_4]. Therefore, we suggest that the left proton signals of the second time measurement is attributed to the weakly bonded [EMIm][BF_4] with a smaller diffusion coefficient. In contrast, the right proton signals is attributed to the strongly bonded [EMIm][BF_4] diffuses faster than the left one.

Table 6-5. Parameters of the diffusion measurement

Sample name=	1st	2nd	3rd	4th
GRADIENT PULSE DURATION (delta) (ms)=	1	1	2	5
DIFFUSION TIME (DELTA) (ms))=	170	100	100	10
DELAY BETWEEN THE 2 FIRST PULSES (tau)=	2.516	2.516	3.535	6.545
REPETITION TIME (D1) (ms)=	5000	1000	1000	1000
MAXXIMUN GRADIENT VALUE [G/cm]=	827.5	1000	1000	1000
GRADIENT START VALUE [G/cm]=	6.19	6.19	6.19	6.19
NUMBER OF GRADIENT STEPS=	32	4	16	8
NUMBER OF SCANS=	1024	10000	3072	5000
Td=	512	512	512	512
rg=	1024	1024	1024	1024
sw=	100	50	50	30

6.3.2.2. Effect of the Amount of Confined [EMIm][BF_4]

The amount of confined [EMIm][BF_4] was calculated by a thermogravimetric analysis (TGA) measurement. Figure 6-11A shows the TGA results of raw ACF-A20,

confined ILs [EMIm][BF_4] inside A20 with a range of adsorbed amounts from 1.7% to 26.2% (by weight loss). All of these samples were made by the method was described in experimental section. To make definite identification, we carried out differential thermogravimetric analysis (DTGA) as given in figure 6-11B. It can be seen that there is an initial loss of weight at a temperature below 350 K. This is attributed to the removal of physically adsorbed water. The DTGA thermograms of A20-26.2% and A20-23.2% show a main weight loss of [EMIm][BF_4] around 650 K which very close to the decomposition temperature 664 K, indicating the weight loss of this region are from the decomposition of the strongly bounded [EMIm][BF_4] confined inside ACF, and the shoulder in the range of 450-600 K should be attributed to the removal of weakly bounded or free [EMIm][BF_4] confined inside ACF. Similarly, the weight loss of lower adsorbed samples A20-3.1% and A20-1.7% in the range of 450-600 K indicates the removal of weakly bounded or free [EMIm][BF_4].

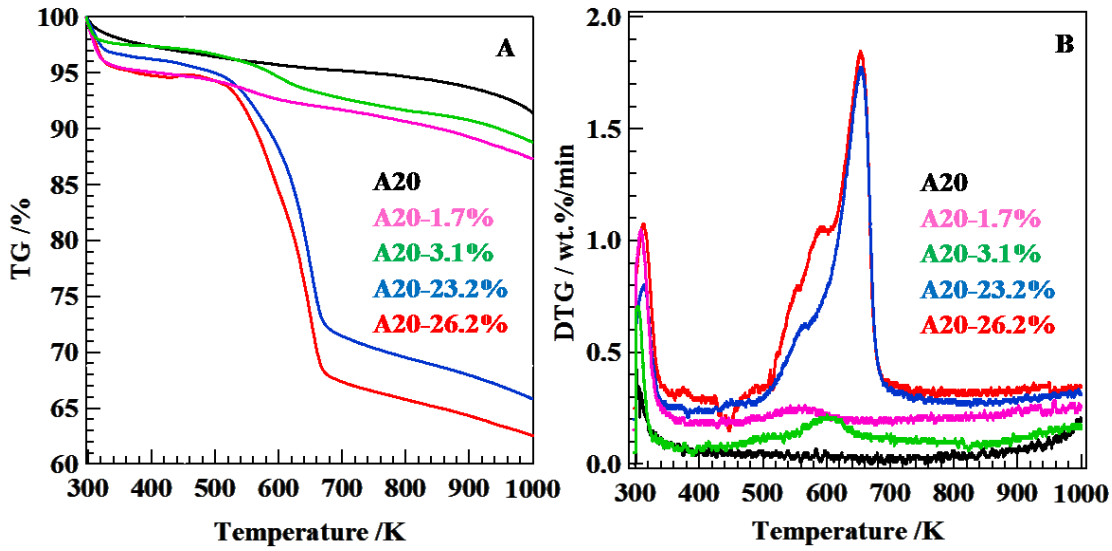

Figure 6-11. TGA thermograms of (A) A20, and A20-[EMIm][BF_4] with a range of adsorbed amounts from 1.7% to 26.2%, and DTG thermograms of those samples (B).

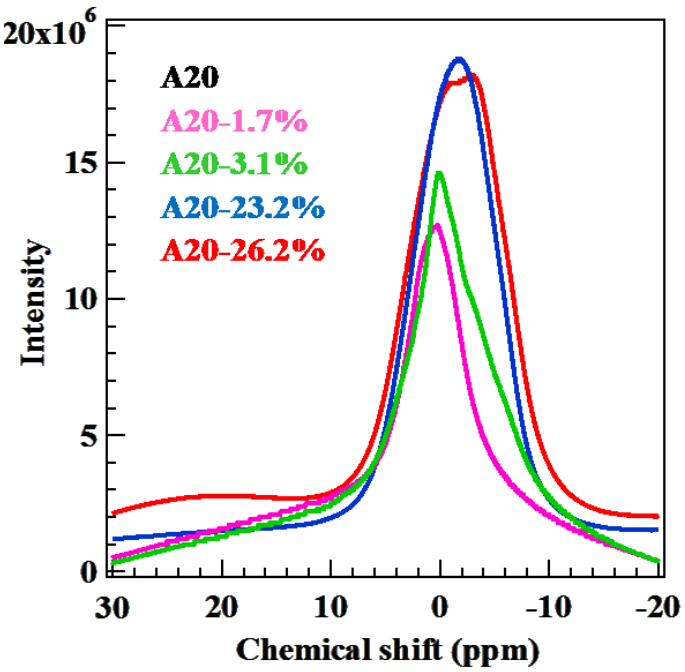

Figure 6-12. ^{1}H NMR spectra of confined [EMIm][BF_4] inside ACF-A20 with a range of adsorbed amount measured at 298 K.

Figure 6-12 shows the ^{1}H NMR spectra of confined [EMIm][BF_4] inside ACF-A20 with a range of adsorbed amount 1.7% - 26.2% (by the weight loss of TGA measurement). Compares the ^{1}H NMR spectrum of [EMIm][BF_4] (see fig. 6-2), there is only one single peak centered at around 1ppm for the lowest adsorbed sample A20-1.7% indicates there are quite a few of water exist in the pores or on outside surface of ACF. When more [EMIm][BF_4] was adsorbed, there are some small peaks appear in a range of -10 - 0 ppm as a shoulder of the main peak. The intensity of these small peaks increases with increasing the amount of adsorbed [EMIm][BF_4], indicates the signals of this region (-10 - 0 ppm) are attributed to the confined [EMIm][BF_4]. This result is corresponding to the DTG analysis.

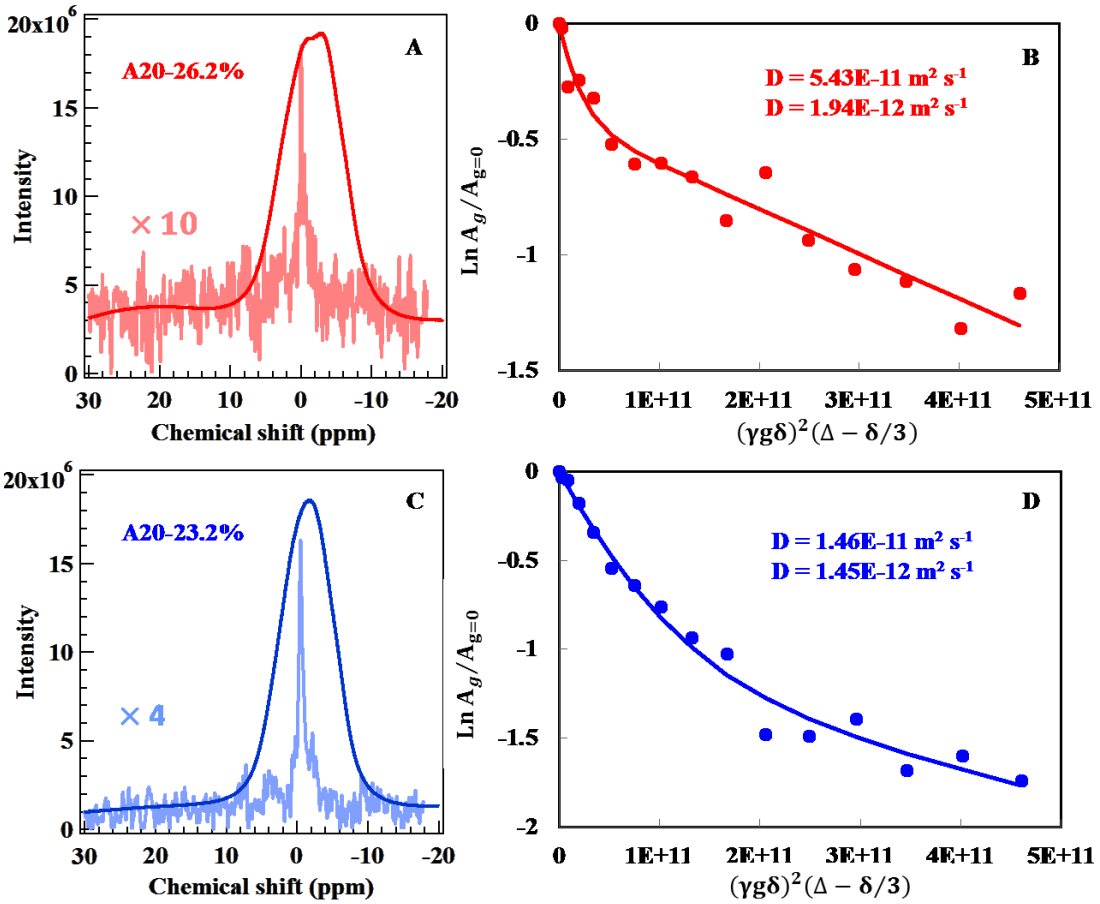

Figure 6-13. ^{1}H NMR spectra (the smooth one) and the one from diffusion measurement (noisy one) (A), the attenuation curves (B) for A20-26.2%, and ^{1}H NMR spectra (C), the attenuation curves (D) for A20-23.2%.

Two samples of confined [EMIm][BF_4] were measured to understand the effect of the adsorbed amount on the dynamic property. In figure 6-13, left side shows the ^{1}H NMR spectra (smooth line) and the singles from the diffusion measurements of (A) A20-26.2%, and (C) A20-23.3%; the right side shows the attenuation curves of (B) A20-26.2%, and (D) A20-23.3%. The detailed measurement set-ups are given in Table 6-6. Both of the samples show a similar attenuation curve contents two components. The faster one is observed at a scale of 10^{-11} m^2 s^{-1}, and the slower one is observed at 10^{-12} m^2 s^{-1}. Compare with the bulk [EMIm][BF_4], we can consider the faster one is attributed to the confined water or free [EMIm][BF_4] because it is very close to the value of the bulk [EMIm][BF_4], and the slower one is attributed to the

confined [EMIm][BF_4] inside ACF-A20. It's also can be seen that, the diffusion coefficient increases with increasing the amount of adsorbed [EMIm][BF_4] indicates the confined ILs moves faster with a higher adsorption or higher pore filling.

Table 6-6. Parameters of the diffusion measurement

Sample name=	A20-26.2%	A20-23.2%
GRADIENT PULSE DURATION (delta) (ms)=	1	1
DIFFUSION TIME (DELTA) (ms))=	60	60
DELAY BETWEEN THE 2 FIRST PULSES (tau)=	2.545	2.545
REPETITION TIME (D1) (ms)=	1000	1000
MAXXIMUN GRADIENT VALUE [G/cm]=	1038.32	1038.32
GRADIENT START VALUE [G/cm]=	6.43	6.43
NUMBER OF GRADIENT STEPS=	16	16
NUMBER OF SCANS=	4000	4000
Td=	512	512
rg=	4096	8192
sw=	50	50

6.3.2.3. Effect of Slit Pore Size of ACF

In this section, slit pore size effect was studied perform on two adsorbents with different slit pore size (1.1 nm for A20, 1.0 nm for A15). The amounts of confined [EMIm][BF_4] were determined by TGA measurement, 23.2% for confined [EMIm][BF_4] in A20 and 22.5% in A15 (by weight loss). The samples are named as A20-23.2%, A15-22.5% and A10-22.5%, respectively, and the amount of the confined [EMIm][BF_4] almost the same (as shown in figure 6-14A). From the DTG curve we observed that sample A15-22.5% and A10-22.5% only show the strongly bonded [EMIm][BF_4]. That is because only micropores existed in A15 and A10 makes those samples have a very high pore loading at the weight loss of 22.5%.

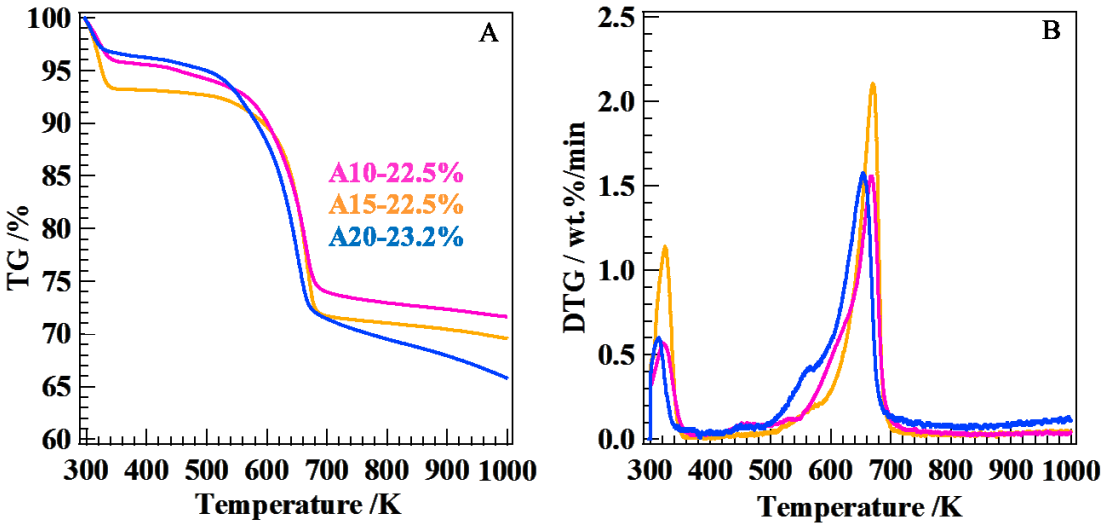

Figure 6-14. TGA thermograms of the confined [EMIm][BF_4] and DTG thermograms of those samples (B).

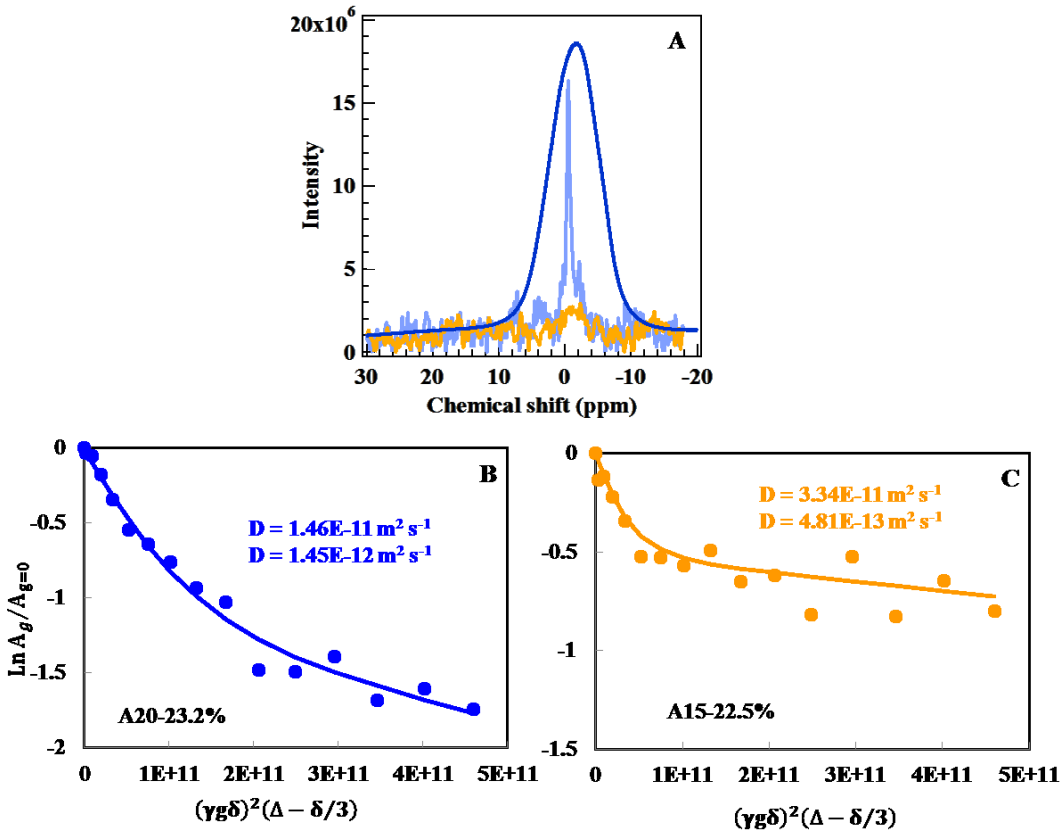

Figure 6-15. 1H NMR spectra of confined [EMIm][BF_4] (A), and attenuation curves of A20-23.2% (B), and A15-22.5% (C).

In this section, we aim to study the pore size effect on the confined [EMIm][BF_4]. Figure 6-15 shows the diffusion results of [EMIm][BF_4] confined in two sizes of slit-pores (1.1 nm for A20 and 1.0 nm fore A15). Both the two samples show a similar attenuation curve contents two components. The faster one is observed at a scale of 10^{-11} m^2 s^{-1}, and the slower one is observed at 10^{-12} m^2 s^{-1} for sample A20-23.2% and 10^{-13} m^2 s^{-1} for sample A15-22.5%. As we described in the last section, the faster one is attributed to the confined water or free [EMIm][BF_4], and the slower one is attributed to the confined [EMIm][BF_4] inside nanopores. The diffusion coefficient due from A20-23.5% was observed three times faster than A15-22.5%. This may be caused by the different structure of confined [EMIm][BF_4] in 1.1 nm nanopores compares with the 1.0 nm nanopores. The structure of confined [EMIm][BF_4] in 1.0 nm pores can be consider as a single file distribution (as shown in figure 6-16), while in 1.1 nm pores, this changes to zigzag distribution of cations and similarly for anions.

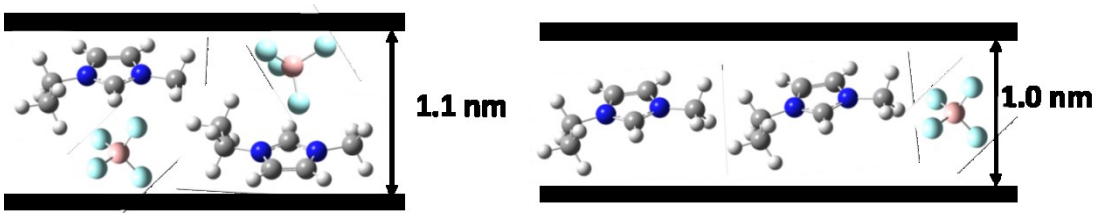

Figure 6-16. Images of the confined [EMIm][BF_4] structure in A20 (left) and A15 (right) with different slit-pore size.

6.4. Conclusions

We studied the effects of the amount of confined [EMIm][BF4], slit pore size of ACF, and the diffusion time of [EMIm][BF4] on structural and dynamical properties of the confined IL [EMIm][BF4]. Our results can be summarized as followers, the increase of the diffusion coefficients D by increasing the amount of confined [EMIm][BF4] caused by the higher adsorption which make the structure of confined [EMIm][BF4] certainly close to the liquid-like structure as well as confined in larger pores. D also increase with decreasing diffusion time Δ, that is caused by the different dynamic state of confined ILs molecules in nanospace such as adsorbed orientation, and adsorbed condition (completed, close or sequestered attached). All of the results indicate that variables such as pore size, pore loading, and pore morphology have a profound influence on the structural and dynamical properties of the confined [EMIm][BF4].

References

[1] J. R. Miller, P. Simon, *Science* **2008**, *321*, 651.

[2] P. Simon, Y. Gogotsi, *Nat. Mater.* **2008**, *7*, 845.

[3] D. N. Futaba, K. Hata, T. Yamada, T. Hiraoka, Y. Hayamizu, Y. Kakudate, O. Tanaike, H. Hatori, M. Yumura, S. Iijima, *Nat. Mater*. **2006**, *5*, 987.

[4] J. Chmiola, C. Largeot, P. L. Taberna, P. Simon, Y. Gogotsi, *Science* **2010**, *328*, 480.

[5] J. R. Miller, R. A. Outlaw, B. C. Holloway, *Science* **2010**, *329*, 1637.

[6] Y. W. Zhu, S. Murali, M. D. Stoller, K. J. Ganesh, W. W. Cai, P. J. Ferreira, A. Pirkle, R. M. Wallace, K. A. Cychosz, M. Thommes, *Science* **2011**, *332*, 1537.

[7] A. Izadi-Najafabadi, T. Yamada, D. N. Futaba, M. Yudasaka, H. Takagi, H. Hatori, S. Iijima, K. Hata, *ACS Nano* **2011**, *5*, 811.

[8] M. F. El-Kady, V. Strong, S. Dubin, R. B. Kaner, *Science* **2012**, *335*, 1326 − 1330.

[9] J. Chmiola et al. *Science* **2006**, *313*, 1760.

[10] J. Chmiola et al. *Chem. Int. Ed.* **2008**, *47*, 3392.

[11] P. Simon, *Nature Mater.* **2008**, *7*, 845.

[12] J. Huang, B. G. Sumpter, V. Meunier, A*ngew. Chem. Int. Ed.***2008**, *47*, 520.

[13] L. Yang, B. H. Fishbine, A. Migliori, L. R. Pratt, *J. Am. Chem. Soc.* **2009**, *131*, 12373.

[14] Y. Shim, H. J. Kim, *ACS Nano* **2010**, *4*, 2345.

[15] G. A. Feng et al. *Phys. Chem. Chem. Phys.* **2011**, *13*, 1152.

[16] B. J. Melde, B. J. Johnson, P. T. Charles, *Sensors* **2008,** *8*, 5202.

[17] A. M. Rossi, L. Wang, V. Reipa, T. E. Murphy, *Biosens. Bioelectron.* **2007**, *23*, 741.

[18] V. Cauda, B. Onida, B. Platschek, L. Muhlstein, T. Bein, *J. Mater. Chem.* **2008**, *18*, 5888.

[19] G. T. Regarajan, D. Enke, M. Steinhart, M. Beiner, *J. Mater. Chem.* **2008**, *18*, 2537.

[20] R. Karnik, K. Castelino, C. Duan, A. Majumdar, *Nano Lett*. **2006**, *6*, 1735.

[21] S. Chen, K. Kobayashi, Y. Miyata, N. Imazu, T. Saito, R. Kitaura, H. Shinohara, *JACS* **2009**, *131*, 14850.

[22] S. Chen, G. Wu, M. Sha, S. Huang, *JACS* **2007**, *129*, 2416.

[23] R. Göbel, P. Hesemann, J. Weber, E. Möller, A. Friedrich, S. Beuermann, A. Taubert, *Phys. Chem. Chem. Phys*. **2009**, *11*, 3653.

[24] J. Le Bideau, P. Gaveau, S. Bellayer, M.-A. Néouze, A. Vioux, Phys. *Chem. Chem. Phys.* **2007**, *9*, 5419.

[25] M. Kanakubo, Y. Hiejima, K. Minami, T. Aizawa, H. Nanjo, *Chem. Commun*. **2006**, *17*, 1828.

[26] A Noda, K Hayamizu, M Watanabe, *J. Phys. Chem. B* **2001**, *105*, 4603.

[27] H Tokuda, K Hayamizu, K Ishii, Md. Abu Bin Hasan Susan, M Watanabe, *J. Phys. Chem. B* **2004**, *108*, 16593.

[28] P. T. Callaghan, *Principles of NMR Microscopy*; Clarendon Press: Oxford, **1991**.

[29] J. Karger, D. M. Ruthven, *Diffusion in Zeolites and Other Microporous Solids*; Wiley & Sons: New York, **1992**.

[30] T. Welton, *Chem. Rev.* **1999**, *99*, 2071.

[31] C. Chiappe, *Monatsh. Chem*. **2007**, *138*, 1035.

[32] K. R. Seddon, A. Stark, M. J. Torres, *Pure Appl. Chem.* **2000**, *72*, 2275.

[33] T. Singh, A. Kumar, *J. Phys. Chem. B* **2007**, *111*, 7843.

[34] K. Hayamizu, Y. Aihara, S. Arai, W. S. Price, *Solid State Ionics* **1998**, *107*, 1.

[35] M. Nakakoshi, S. Ishihara, H. Utsumi, H. Seki, Y. Koga, K Nishikawa, *Chem. Phys. Lett.* **2006**, *427*, 87.

General Conclusions

In this work, the electronic property of single-walled carbon nanotubes (SWCNTs) was studied by encapsulation the guess molecules or ions. The electronic structure of modified SWCNTs was examined by means of absorption spectroscopy, Raman spectroscopy, high resolution electron microscopy (HR-TEM) with high sensitivity, porosity analysis methods.

The diffusion behavior of ionic liquids in nanospace of activated carbon fibers was also investigated. The examination was carried out by an pulsed-field gradient-nuclear magnetic resonance (PFG-NMR) method.

In chapter 4, a study of electronically modified SWCNT with hexaiodobenzen (HIB) was carried out to understand the charge transfer interaction between the wall of the SWCNTs and adsorbed molecules. The TEM image shows the adsorbed molecules almost exist in the internal of SWCNTs. The disappearance of the absorption signals and the chemical shift Raman and XPS peaks indicate the existence of week charge transfer between SWCNT and adsorbed HIB molecules.

In chapter 5, the electrochemical property of SWCNTs-coated PET film is studied by cyclic voltammetry and alternating current (AC) impendence methods. As the results of cyclic voltammetry, a pair of well-defined redox waves of I_3^-/I^- is obtained. The peak-to-peak separation increases with increasing scan rate, indicating a quasi-reversible process likely as the result of both the slow electron transfer at the SWCNT surface and the slow diffusion through the narrow pore. It is also found that both the anodic and cathodic peak currents show a linear dependence with the square root of scan rates. Such behavior appears in a quiescent solution in case of diffusion of an ionic species in the vicinity of the electrode surface, which defines the rate of the reaction. In the case of AC impendence, we have successfully realized the application of spray coated SWCNTs on PET substrate as an electrodes for tri-iodide reduction in DSSCs. The charge transfer resistance of SWCNT-PET electrode in I_3^-/I^- redox couple electrolyte can be controlled by changing SWCNTs loading.

In chapter 6 reports the results of PFG-NMR diffusion study of imidazolium-based ionic liquids and the structure and dynamic properties of the IL [EMIm][BF_4] confined inside a nanoporous carbon materials, ACF. Our results indicate that variables such as pore size, pore loading, and pore morphology have a profound influence on the structural and dynamical properties of confined ILs.

Acknowledgements

First and foremost I would like to express my deepest gratitude to my advisor Professor Hirofumi Kanoh, for his invaluable guidance, consistent encouragement, and support. I have been fortunate to gain the benefit of his expertise in the field of molecular chemical, especially electrical chemical. He has always been a patient listener to my research ideas and constantly gave me positive feedback in order to implement them. I wish to express my deep and sincere gratitude to Professor Katsumi Kaneko of Research Center for Exotic Nanocarbon, Shinshu University, for his valuable suggestions, detailed and constructive comments and important support throughout my work. Also I am deeply grateful to Assistant Professor Tomonori Ohba for suggestions, valuable discussions, and encouragements.

I wish to express my deep and sincere gratitude to Professor Terence Cosgrove and Dr. Stuart Prescott of University of Bristol, and Professor Peter Griffiths of University of Greenwich in UK for great suggestions and discussion. I have been fortunate to gain the benefit of their expertise in the field of diffusion NMR measurement. I am also very thank to Dr. Youssef Espidel for his patiently guidance of the operation of the NMR instrument.

I would like to thank to Professor Sumia Iijima, Dr. Motoo Yumura, and Dr. Kenji Hata of Nanocarbon Research Center, National Institute of Advanced Industrial Science and Technology (AIST) for kindly proving the Super-Growth SWCNT samples. Also I am deeply grateful to Hiroto Komatsu and Akira Sakuma of Godo Shigen sangyo Co. for kindly proving the hexaiodobenzene (HIB) samples.

Many thank to Dr. Bo Hou of University of Bristol for many experiments like SEM, TEM, and NMR measurement.

I should mention many great friends and all members in molecular groups of Chiba University as being important in my study and life. During this work, their supports and encourages have been very helpful for my life as researcher. Above all, very thanks to Mr. Chi Song, Mr. Chenghao Sun, Dr. Yan Cheng, Dr. Yongjun Liu, Dr. Shuwen Wang, Ms. Natsuko Kojima, and Dr. Fitri Khoerunnisa who were wonderful

colleagues in friendly rivalry to me all the time.

I would like to thank to Faculty of Science, Chiba University as well as to the Global Center of Excellent (G-COE) Chiba University for offering the research assistant during the postgraduate period and a research grant. Those are being the great supports for study, research and living allowances. Also I warmly thank the Japan Society of the Promotion of Science (JSPS) for the support by a Grant-in-Aid for Fundamental Scientific Research (B) (No. 23350072).

Finally, I would like to give my special thanks to my parents, my sister and brother and my husband for their ever-present love, great understanding, encouragement and support in my life and study.

July, 2013

Lu Mingxia

Accomplishments

Publications:

Mingxia Lu, Tomonori Ohba, Katsumi Kaneko, Kenji Hata, Motoo Yumura, Sumio Iijima, Hiroto Komatsu, Akira Sakuma and Hirofumi Kanoh, Electron density control of SWCNT by liquid-phase molecular adsorption of hexaiodobenzene, *Materials* **2013**, *6*, 535-543.

Conferences (International)

Mingxia Lu, Tomonori Ohba, Katsumi Kaneko, Kenji Hata, Motoo Yumura, Sumio Iijima, Hiroto Komatsu, Akira Sakuma and Hirofumi Kanoh, Electron density control of SWCNT by liquid-phase molecular adsorption of hexaiodobenzene, the 10th International Conference on Fundamentals of Adsorption (FOA10), Hyogo-Awaji Yumebutai, Japan, May 24 to 28th, 2010 (Poster).

Mingxia Lu, Tomonori Ohba, Katsumi Kaneko and Hirofumi Kanoh, Electrochemical analysis of iodide ions on SWCNT thin films, Carbon 2011, Shanghai, China July 24 to 29th, 2011 (Poster).

Conference (Domestic)

M. Lu, T. Ohba, H. Kanoh, K. Hata, M. Yumura, S. Iijima, H. Kamatru, A. Sakuma, and K. Kaneko, Adsorption property control of SWCNT walls with electron-donor and acceptor interaction, The 13th Symposium on iodine Science, Chiba University, Japan October 8th, 2010 (Poster)